Pontifícia Universidade Católica
do Rio de Janeiro

Artur Serpa de Carvalho Rego

Kinetic study on thermal decomposition of sulfates: TGA experiments and modelling

Tese de Doutorado

Thesis presented to the Programa de Pós–graduação em Engenharia de Materiais e de Processos Químicos e Metalúrgicos, do Departamento de Engenharia Química e de Materiais da PUC-Rio in partial fulfillment of the requirements for the degree of Doutor em Engenharia de Materiais e de Processos Químicos e Metalúrgicos.

Advisor : Prof. Rogério Navarro Correia Siqueira
Co-advisor: Prof. Rodrigo Fernandes Magalhães de Souza

Rio de Janeiro
October 2022

Pontifícia Universidade Católica
do Rio de Janeiro

Artur Serpa de Carvalho Rego

Kinetic study on thermal decomposition of sulfates: TGA experiments and modelling

Thesis presented to the Programa de Pós–graduação em Engenharia de Materiais e de Processos Químicos e Metalúrgicos da PUC-Rio in partial fulfillment of the requirements for the degree of Doutor em Engenharia de Materiais e de Processos Químicos e Metalúrgicos. Approved by the Examination Committee:

Prof. Rogério Navarro Correia Siqueira
Advisor
Departamento de Engenharia Química e de Materiais – PUC-Rio

Prof. Rodrigo Fernandes Magalhães de Souza
Co-advisor
Departamento de Engenharia Química e de Materiais – PUC-Rio

Prof. Francisco José Moura
PUC-Rio

Drª. Andréa Pereira Parente
PUC-Rio

Prof. Víctor de Andrade Alvarenga Oliveira
UFOP

Prof. Fernando Luiz Pellegrini Pessoa
Centro Universitário SENAI CIMATEC

Rio de Janeiro, October 7th, 2022

Artur Serpa de Carvalho Rego

Graduated in chemical engineering at PUC-Rio in 2015. Master's degree in Materials Engineering and Chemical and Metallurgical Processes at PUC-Rio in 2017.

Bibliographic data

Serpa de Carvalho Rego, Artur

Kinetic study on thermal decomposition of sulfates: TGA experiments and modelling / Artur Serpa de Carvalho Rego; advisor: Rogério Navarro Correia Siqueira; co-advisor: Rodrigo Fernandes Magalhães de Souza. – 2022.

116 f: il. color. ; 30 cm

Tese (doutorado) - Pontifícia Universidade Católica do Rio de Janeiro, Departamento de Engenharia Química e de Materiais, 2022.

Inclui bibliografia

1. Engenharia Química – Teses. 2. Engenharia de Materiais – Teses. 3. Sulfatos metálicos. 4. Modelagem. 5. Otimização por enxame de partículas. 6. Cinética. 7. Decomposição térmica. I. Navarro Correia Siqueira, Rogério. II. Fernandes Magalhães de Souza, Rodrigo. III. Pontifícia Universidade Católica do Rio de Janeiro. Departamento de Engenharia Química e de Materiais. IV. Título.

CDD: 620.11

Acknowledgments

First and foremost, I would like to thank my parents, Flavia and José Eduardo, and my sister Isabel for the never-ending support in every step taken in all these years.

I would like to thank my advisor, Professor Rogério Navarro, and co-advisor, Professor Rodrigo Souza, for helping me understand the thesis's technical aspects and supporting the conversations throughout the years.

A special thanks to Professors Amanda Lemette and Brunno Santos from LaMAC for helping me to understand more about modeling and optimization algorithms.

I would like to thank Henrique Meira for the help in the thermal runs and laboratory analyses.

I would like to express my gratitude to all the friends I made as postgraduate in PUC, Annita Fidalgo, João Gonçalves, Ana Dourado, Julia Cardoso, Aimée Valente, Nathalli Mello, Layne Lucas, Camila Souza and Jéssica Rocha.

I would like to offer a special thanks to my friends that I can always count on, Zeca Carvalho, Kaio Caiazzo, Beatriz Vergaça, Cadu Ribeiro, Renata Nofal, Elisa Salgado, Alberto Nogueira, Lucas Tamaki, André Nogueira, José Henrique Blanco, Felipe Bizzo, Pablo Esteban Salinas, Felipe Hadba, and Felipe Argento.

This study was financed in part by the Coordenação de Aperfeiçoamento de Pessoal de Nível Superior - Brasil (CAPES) - Finance Code 001.

Abstract

Serpa de Carvalho Rego, Artur; Navarro Correia Siqueira, Rogério (Advisor); Fernandes Magalhães de Souza, Rodrigo (Co-Advisor). **Kinetic study on thermal decomposition of sulfates: TGA experiments and modelling**. Rio de Janeiro, 2022. 116p. Tese de Doutorado – Departamento de Engenharia Química e de Materiais, Pontifícia Universidade Católica do Rio de Janeiro.

The interest over of the decomposition of sulfates has increased due to its capacity of generating clean H_2 through the thermochemical cycles. Understanding the decomposition mechanism is relevant to future industrial design and applications. Moreover, the modeling of these processes gives the information needed to know how much energy is required for the occurrence of the reactions. Among the different reaction systems, it is observed a range of complexity, with the presence of intermediate phases, and multiple consecutive or simultaneous reactions. Therefore, the present work proposed to develop a modeling methodology for the thermal decomposition of sulfates systems with different complexity levels: aluminum sulfate, potassium alum, mixture of aluminum sulfate and potassium sulfate, zinc sulfate, and iron (II) sulfate. The experiments were performed using thermogravimetric analysis (TGA) to understand the decomposition stages and use the data in the modeling step. The developed model consisted of a system of differential equations to describe every reaction taking place in the decomposition. The kinetic parameters estimation was made by using particle swarm optimization. The results indicate that potassium sulfate catalyzes the decomposition of aluminum sulfate. In the case of zinc, the desulfation of anhydrous zinc sulfate occurs in two stages, with the presence zinc oxysulfate as an intermediate phase. Iron (II) sulfate also shows a complex decomposition system, as it first decomposes into iron (III) sulfate before it is completely converted into hematite. All the modeling results displayed an excellent agreement with the experimental data, with R^2 values above 0.98 for all cases.

Keywords

Metal sulfates; Modeling; Particle swarm optimization; Kinetics; Thermal decomposition.

Resumo

Serpa de Carvalho Rego, Artur; Navarro Correia Siqueira, Rogério; Fernandes Magalhães de Souza, Rodrigo. **Estudo cinético da decomposição térmica de sulfatos: experimentos de TG e modelagem**. Rio de Janeiro, 2022. 116p. Tese de Doutorado – Departamento de Engenharia Química e de Materiais, Pontifícia Universidade Católica do Rio de Janeiro.

A decomposição de sulfatos vem ganhando notoriedade pela sua capacidade de geração limpa de H_2 através dos ciclos termoquímicos. O entendimento do mecanismo de decomposição é relevante para futuros planejamentos em aplicações industriais. Além disso, a modelagem desses processos permite obter informações acerca da energia requerida para que os mesmos ocorram. Dentre os diferentes sistemas de reações de decomposição, observa-se que alguns deles são mais complexos do que outros, envolvendo a presença de fases intermediárias e múltiplas reações consecutivas ou simultâneas. Portanto, o presente trabalho se propõe a desenvolver uma metodologia para a modelagem da decomposição térmica de sistemas reacionais com diferentes níveis de complexidade: sulfato de alumínio, alúmen de potássio, mistura de sulfatos de alumínio e potássio, sulfato de zinco e sulfato de ferro (II). Os experimentos foram realizados utilizando análise termogravimétrica (TG) para ter o entendimento dos diferentes estágios de decomposição, utilizando os dados obtidos na etapa de modelagem. O modelo envolveu o uso de um conjunto de equações diferenciais para representar cada uma das reações que ocorrem na decomposição. A estimação dos parâmetros cinéticos feita pelo método de otimização por enxame de partículas. Os resultados indicaram que sistemas envolvendo a decomposição do sulfato de alumínio são catalisados na presença de sulfato de potássio. No caso do zinco, a dessulfatação do sulfato anidro ocorre em duas etapas, com a presença de um oxissulfato como uma fase intermediária. O sulfato de ferro (II) também apresenta uma decomposição complexa ao passar pela fase de sulfato de ferro (III) antes de ser completamento convertido em hematita. Todas as modelagens mostraram excelente ajuste aos dados experimentais, com R^2 acima de 0.98 em todos os casos.

Palavras-chave

Sulfatos metálicos; Modelagem; Otimização por enxame de partículas; Cinética; Decomposição térmica.

Table of contents

List of figures

List of tables

Calma
A pressa é um vício descontente
É justo navegar contra a corrente
Mas calma
Pois tudo sempre encontra o seu lugar

Maglore, *Calma (Todas as Bandeiras).*

1
Introduction

Fossil fuels are the main source of energy production, constituted in the burn of coal, natural gas, and oil. The fact that these materials are not renewable represent a problem in a long-term period, as the sources are naturally finite, and the demand tends to grow over the rise of the world's population.[1] Furthermore, the concern over the consequences of using fossil fuels has increased since the end of 20th century. The main product of burning fossil fuels is the greenhouse effects gases, and its continuous use is now causing climate changes, such as Earth temperature and ocean-level rise, and uncommon climate events occurring more frequently.[2–4]

Therefore, the development of new technologies that allow the use of a different energy-matrix is required. Hydrogen (H_2) seems like a viable route, as there are different ways of producing it and its consumption to produce energy represents a clean process, as shown in Equation 1-1. There are different ways of obtaining H_2, such as water electrolysis,[5,6] steam reforming,[7–9] photocatalysis,[10] and thermochemical cycles.[11–13] Among the presented processes for hydrogen production, the thermochemical water-splitting cycles has gained some recognition as it represents a sustainable and environmentally friendly route.[14]

$$H_{2(g)} + \frac{1}{2}\,O_{2(g)} \longrightarrow H_2O_{(g)} \tag{1-1}$$

In the case of most metal sulfates, the cycle contemplates the decomposition of those compounds into their respective oxides and further regeneration back to the sulfate form. The generic mechanism involved in this process is displayed in Equations 1-2 and 1-3. The water-splitting cycle is represented in Equation 1-4, and is noted as the global reaction. The whole process is subjected to the temperature in which the metal sulfate decomposes into the oxide. Therefore, if the sulfate is stable in wide temperature range, such as the $CaSO_4$,[15,16] the process becomes inefficient as it requires more energy to generate the desired H_2.

$$MSO_4 \longrightarrow MO + SO_{2(g)} + \frac{1}{2}\,O_{2(g)} \tag{1-2}$$

$$MO + SO_{2(g)} + H_2O_{(g)} \longrightarrow MSO_4 + H_{2(g)} \tag{1-3}$$

$$H_2O_{(g)} \longrightarrow H_{2(g)} + \frac{1}{2}\,O_{2(g)} \tag{1-4}$$

Bhosale and contributors[17–20] have performed a series of studies over the

viability of using different sulfates to generate hydrogen using the thermochemical water-splitting cycles. Moreover, more contributions can be made to enhance the process, such as reducing the decomposition temperature of the sulfates using different atmosphere compositions[21,22] or testing different materials that can be used as catalysts.[14,23]

Besides knowing the thermochemical viability, it is important to have an understanding over the thermal decomposition mechanisms and its kinetics. The thermal decomposition of sulfates have been addressed in an immense amount of works, studying different variables, such as sample size,[24,25] atmosphere composition,[21,22,25] and using additives.[14,24,26,27] These studies are essential to understand all that involves the decomposition reaction, and also to try to achieve better conditions in which the process can take place. Moreover, the modeling of those processes is also important, as they can numerically describe the kinetic parameters of interest, mainly the activation energy (E_a).

Different modeling techniques can be approached to verify the parameters. For isothermal studies, the Arrhenius plot can be used to determine the activation energy and the pre-exponential factor (k_0) values.[28–30] In dynamic heating situations, other methods can be used, such as the model-free equations. In this case, different models are assumed depending on the controlling step of the studied process. Thus, a series of different equations are used and the one that displays the best fitting is the chosen one. This type of modeling has been widely used in the literature.[31–35]

The graphical technique is also applicable in dynamic heating rate as showed by Vachuška and Vobořil.[36] In this case, the ordinary differential equation (ODE) is manipulated to yield an equation that can determine the kinetic parameters using its angular and linear coefficients. However, their applicability is limited to cases in which the mechanism is simple, usually involving one decomposition step, or when the multiple steps are well-segmented. Therefore, some modifications are required to use such models. By using the ODE (or system of ODEs), it is possible to better describe the model itself, requiring only a method can estimate the kinetic parameters present in the equations.

Similar to the modeling technique, there are different ways to estimate the kinetic parameters, usually being divided into two groups, the deterministic ones, such as Newton Method and the stochastic ones, such as particle swarm optimization (PSO). The first is normally based on the derivatives of the functions involved in the problem. On the other hand, the stochastic ones take a more statistical approach in the estimation process. Both types of techniques have one common goal, which is to minimize the objective function of the

problem.

In the present work, the thermal decomposition of different metal sulfates (potassium alum, zinc sulfate, and iron (II) sulfate) were performed using a thermogravimetric balance using different heating rates in inert atmosphere (N_2). Thermodynamic simulation were performed to understand the possible scenarios involving the reaction mechanisms. A different model was developed for each sulfate studied as each one presented its unique mechanism. As for the estimation of all the kinetic parameters, the PSO technique was used to minimize the objective function.

2
Objectives

2.1
Main goal

Evaluate the thermal decomposition of potassium alum dodecahydrate ($KAl(SO_4)_2 \cdot 12\,H_2O$), zinc sulfate heptahydrate ($ZnSO_4 \cdot 7\,H_2O$), and iron (II) sulfate heptahydrate ($FeSO_4 \cdot 7\,H_2O$) using a thermogravimetric balance. Moreover, develop a model capable of describing the listed scenarios, and estimate the kinetic parameters of the decomposition reactions using particle swarm optimization.

2.2
Specific goals

- Perform the thermal decomposition of the different sulfates in a thermogravimetric balance using different heating rates in inert atmosphere;
- Run thermodynamic simulations of the equilibrium composition of the different reaction systems;
- Develop a kinetic model to describe the thermal decomposition systems;
- Estimate the kinetic parameters of the models using particle swarm optimization;

3
Literature review

3.1
Potassium alum

Potassium alum is a double salt (K_2SO_4 and $Al_2(SO_4)_3$) commonly found in its dodecahydrate form ($KAl(SO_4)_2 \cdot 12\,H_2O$), a white colored compound.[37] As the hydrated potassium is heated, the structure 'loses' nine water molecules, yielding the potassium alum trihydrate ($KAl(SO_4)_2 \cdot 3\,H_2O$). The further heating leads to the anhydrous compound, which decomposes into potassium sulfate (K_2SO_4) and aluminum oxide (Al_2O_3). The reaction steps of the dehydration process can be seen in Equations 3-1 and 3-2.

$$KAl(SO_4)_2 \cdot 12\,H_2O \xrightarrow[70\ ^\circ C]{\Delta} KAl(SO_4)_2 \cdot 3\,H_2O + 9\,H_2O_{(g)} \tag{3-1}$$

$$KAl(SO_4)_2 \cdot 3\,H_2O \xrightarrow[230\ ^\circ C]{\Delta} KAl(SO_4)_2 + 3\,H_2O_{(g)} \tag{3-2}$$

Kishimura, Imasu and Matsumoto[38] studied the dehydration of potassium alum using Raman spectroscopy and XRD analysis, concluded that it is a complex process that takes place in several stages. The number of steps in which the dehydration process occurs diverges among the authors that studied the thermal decomposition of $KAl(SO_4)_2 \cdot 12\,H_2O$ using TGA/DTA.[21,26,35,39–44] Souza et al.,[21] and Meshram, Gautam and Singh[44] reported that there the dehydration process occurs in four different steps instead of two. Wojciechowska, Wojciechowski and Kamiński[35] reported that the dehydration takes place in three different stages.

The reaction steps of the decomposition of potassium alum is not completely investigated. Based on the TGA/DTA curves from the literature studies, there is only one drop in the curve, indicating that the process occurs with only one decomposition stage, resulting in aluminum oxide and potassium sulfate,[26,35,40,41] as seen in Equation 3-3.

$$2\,KAl(SO_4)_2 \xrightarrow{\Delta} Al_2O_3 + K_2SO_4 + 3\,SO_{2(g)} + \frac{3}{2}\,O_{2(g)} \tag{3-3}$$

However, as potassium alum is a complex salt, the decomposition reaction steps could be more elaborated than the one described above. Souza et al.[21] performed the decomposition in both inert and reductive atmospheres and identified an intermediate compound in their XRD analysis, $K_3H(SO_4)_2$. The presence of this compound could be an indication that the real decomposition

reaction steps involves reactions without weight loss, which not be identified using TGA/DTA.

The presence of $K_3H(SO_4)_2$ was observed in other works, usually associated with potassium sulfate (K_2SO_4) and potassium bissulfate ($KHSO_4$).[45–47] Vries and Gellings[48] performed a careful study concerning the thermal decomposition of different potassium-bearing compounds ($KHSO_4$, $K_2S_2O_7$, $K_2S_2O_8$). By using TGA and XRD, the authors concluded that the decomposition of $KHSO_4$ into K_2SO_4 occur in finite steps, with the presence of another intermediate compound (K_2SO_5), according to Equations 3-4, 3-5 and 3-6.

$$2\,KHSO_4 \xrightarrow{\Delta} K_2S_2O_7 + H_2O_{(g)} \tag{3-4}$$

$$K_2S_2O_7 \xrightarrow{\Delta} K_2SO_5 + SO_{2(g)} \tag{3-5}$$

$$K_2SO_5 \xrightarrow{\Delta} K_2SO_4 + \frac{1}{2}\,O_{2(g)} \tag{3-6}$$

Aside from potassium, the complex salt also has the presence of aluminum. The reaction steps of the decomposition of $Al_2(SO_4)_3$ was already studied in a number of works.[26,28,31,40,49,50] The reaction takes place in only one step, corresponding to the formation of aluminum oxide (Al_2O_3), as seen in Equation 3-7. A noticeable interaction between aluminum sulfate and potassium sulfate was reported by Apte, Kiran and Chernosky.[26] The authors observed that the decomposition temperature of aluminum sulfate was reduced in the presence of potassium sulfate, possibly with the latter having a catalytic effect in the decomposition of $Al_2(SO_4)_3$. This behavior can be seen in the TGA curves, as the anhydrous potassium alum begins to decompose around 650 °C, whereas anhydrous aluminum sulfate begins to decompose almost 100 °C higher, indicating that K_2SO_4 indeed has an impact in decomposition of $Al_2(SO_4)_3$.

$$Al_2(SO_4)_3 \xrightarrow{\Delta} Al_2O_3 + 3\,SO_{3(g)} \tag{3-7}$$

3.1.1 Kinetic studies

There is a variety of kinetic studies regarding the decomposition of potassium alum. Most of the authors used TGA under isothermal or dynamic conditions to determine the decomposition temperatures and perform the kinetic modeling. Moreover, the atmosphere conditions also present some variation, with authors using oxidative (air), inert and vacuum conditions. In the case of potassium alum, some authors also performed thermal studies with other aluminum and potassium bearing species to make comparisons.

Pysiak and Glinka[41,42] reported a study in two parts concerning the thermal decomposition of basic aluminum potassium sulfate ($K[Al_3(OH)_6][SO_4]_2$). The first part of the work proposed to identify the different decomposition stages, concluding that the decomposition takes place in three different stages. The first (200 - 400 °C) and second (400 - 600 °C) ones represent the complete dehydration of basic aluminum potassium sulfate, yielding potassium alum. The third and final stage (600 - 950 °C) represents the desulfation of $KAl(SO_4)_2$ into potassium sulfate and aluminum oxide.

The second part of their work concerned the kinetics of the reaction. Each stage was studied in isothermal and isobaric (10^{-3} hPa) conditions. The modeling was divided into the dehydration and the desulfation processes. The first one was better described using the Kolmogorov-Erofeev-Avrami, with activation energies of 139.5 kJ.mol^{-1} for the first stage of dehydration and 200.5 kJ.mol^{-1} in the second dehydration step. The desulfation process was better described by the Bronstein-Ginstling model, with an activation energy of 215.9 kJ.mol^{-1}.

Wojciechowska, Wojciechowski and Kamiński[35] studied the thermal decomposition of ammonium and potassium alums using TGA under air and inert (argon) atmospheres at a heating rate of 3.5 °C.min^{-1}. At temperatures above 750 °C, it was observed the formation of K_2SO_4, Al_2O_3 and SO_3 as the products of the decomposition of potassium alum, observing a small difference in the starting decomposition temperature depending on the composition of the atmosphere. The authors used model-free equations for the kinetic modeling of the process resulting in activation energies values of 180 kJ.mol^{-1} in air atmosphere and 172 kJ.mol^{-1} in inert atmosphere.

Küçük and contributors[32,51] studied the thermal decomposition of alunite ore ($KAl_3(SO_4)_2(OH)_6$). In their first study, it was determined that the first step in the decomposition of the ore (around 500 °C) resulted in anhydrous potassium alum and amorphous Al_2O_3. Around 700 °C, the XRD peaks correspondent to $KAl(SO_4)_2$ disappeared and the formation of potassium aluminum sulfate ($K_3Al(SO_4)_3$) and aluminum sulfate were observed, which are further decomposed into K_2SO_4 and $Al_2(SO_4)_3$. These second and third decomposition steps, shown in Equations 3-8 and 3-9, are not simply detected in TGA, as they do not have any weight loss involved in whole process.

$$2\,KAl(SO_4)_2 \xrightarrow{\Delta} \frac{2}{3}\,K_3Al(SO_4)_3 + \frac{2}{3}\,Al_2(SO_4)_3 \tag{3-8}$$

$$\frac{2}{3}\,K_3Al(SO_4)_3 \xrightarrow{\Delta} K_2SO_4 + \frac{1}{3}\,Al_2(SO_4)_3 \tag{3-9}$$

In a later study,[32] the kinetic data regarding the decomposition of

alunite ore was addressed. The TG experiments were performed under air atmosphere at different heating rates (5 – 20 °C.min^{-1}). The reaction steps of the decomposition is the same one as seen in their previous study[51] (Equations 3-8 and 3-9). The kinetic modeling method chosen were Ozawa and KAS, reaching similar results in both ones. For a conversion degree of 0.1, the activation energies observed were 226.3 kJ.mol^{-1} (Ozawa) and 220.7 kJ.mol^{-1} (KAS), and for a conversion degree of 0.8, the values were 320.3 kJ.mol^{-1} (Ozawa) and 328.6 kJ.mol^{-1} (KAS).

Apte and contributors[26,31] studied the decomposition of aluminum sulfate, potassium alum, alunite, and ammonium alum using TGA in inert atmosphere (60 L.min^{-1}) at a heating rate of 20 °C.min^{-1}. The authors reported that up to 300 °C, potassium alum completely dehydrates, and further decomposes into Al_2O_3, K_2SO_4, and SO_3. Aluminum sulfate dehydrates completely at 400 °C and later decomposes into Al_2O_3 and SO_3 at 750 °C. The TGA and DTA curves indicate that the presence of K_2SO_4 contributes to the reaction by lowering the temperature of the decomposition of $Al_2(SO_4)_3$, noticed by the decomposition temperature mentioned earlier.

The kinetic modeling was performed only for aluminum sulfate using different model-free equations. As expected, the activation energy values showed great variation depending on the reaction steps. Apte et al.[31] reported that the thermal decomposition of $Al_2(SO_4)_3$ was better described in the contracting disc with an activation energy of 235 kJ.mol^{-1}.

Papazian, Pizzolato and Orrell[49] studied the thermal decomposition of aluminum sulfate using dynamic TGA (15 °C.min^{-1}) under air atmosphere and vacuum (2×10^{-6} torr). In both conditions, the dehydration is complete at 400 °C and the decomposition is complete in temperatures higher than 920 °C. The authors did not observe the presence of SO_3 under vacuum condition. The modeling is not specified clearly, only indicating the equation used in the work. The kinetic results indicate that the atmosphere condition has a significant impact in the decomposition process. The reaction was found as first-order under air atmosphere and second-order in vacuum. Regarding the activation energy, the authors reported that the values coincide at 398 kJ.mol^{-1} in the temperature range of 770 - 880 °C. For higher temperatures, the activation energy of the decomposition of $Al_2(SO_4)_3$ was 120 kJ.mol^{-1} in air atmosphere and 95.8 kJ.mol^{-1} in vacuum.

Chou and Soong[28] performed studies on the thermal decomposition of aluminum sulfate using TGA (air atmosphere) in dynamic and static conditions. The authors used model-free equations and Arrhenius plot to calculate the activation energy of the reaction. The isothermal runs indicated

an activation energy of 482 kJ.mol^{-1}, a value higher than presented by previous authors.[49,52,53] However, the difference could be related to experimental design and conditions used in each work. In the dynamic studies, different sample sizes and heating rates were tested. The results indicate a decrease of the activation energy as the heating is increased and, by extrapolating to a zero heating rate, the authors reached a result that matched the same values as the isothermal runs. The change in the sample sizes also impacted the activation energy, as the weight increases, the activation energy decreases, as the geometries change in the crucible and the mass and heat transfer effects are affected by the quantity of reactant.

3.2 Zinc sulfate

Zinc sulfate is a salt very soluble in water that has different hydrate forms (mono-, di, tetra-, hexa-, and heptahydrate).[54] The dehydration process of zinc sulfate heptahydrate ($ZnSO_4 \cdot 7\,H_2O$) takes place in different steps. At first, around 40 °C, the structure 'loses' one water molecule, yielding the hexahydrate form ($ZnSO_4 \cdot 6\,H_2O$). Around 100 °C, $ZnSO_4 \cdot H_2O$ becomes the stable phase. The anhydrous salt is obtained in temperatures close to 250 °C. The reactions of the different dehydration steps can be seen in Equations 3-10, 3-11, and 3-12.

$$ZnSO_4 \cdot 7\,H_2O \xrightarrow[40\ ^\circ C]{\Delta} ZnSO_4 \cdot 6\,H_2O + H_2O_{(g)} \tag{3-10}$$

$$ZnSO_4 \cdot 6\,H_2O \xrightarrow[100\ ^\circ C]{\Delta} ZnSO_4 \cdot H_2O + 5\,H_2O_{(g)} \tag{3-11}$$

$$ZnSO_4 \cdot H_2O \xrightarrow[250\ ^\circ C]{\Delta} ZnSO_4 + H_2O_{(g)} \tag{3-12}$$

Some authors[24,34,55] studied the thermal decomposition of zinc sulfate heptahydrate, showing that the dehydration mechanism occurs in three different steps. However, the starting material in the work of Mu and Perlmutter[24] consisted in a mixture of zinc hepta- and tetra- hydrates, leading to a slightly different results when comparing with the other authors.[34,55]

Upon further heating, the anhydrous zinc sulfate decomposes into zinc oxide. This step was thoroughly by many works, as the desulfation process does not occur in one direct step, but rather with the presence of an intermediate phase ($ZnO \cdot 2\,ZnSO_4$).[25,56–60] The reaction steps in which the decomposition of anhydrous zinc sulfate takes place is well-established in the literature, as seen in Equations 3-13 and 3-14.

$$ZnSO_4 \xrightarrow{\Delta} \frac{1}{3}\,ZnO \cdot 2\,ZnSO_4 + \frac{1}{3}\,SO_{3(g)} \tag{3-13}$$

$$\frac{1}{3}\,\mathrm{ZnO}\cdot 2\,\mathrm{ZnSO_4} \xrightarrow{\Delta} \mathrm{ZnO} + \frac{2}{3}\,\mathrm{SO_{3(g)}} \tag{3-14}$$

The conditions in which the experiments take place have a direct impact in the decomposition temperature. This was extensively addressed in the work of Narayan, Tabatabaie-Raissi and Antal,[25] which performed their experiments using different variables: atmosphere composition (helium and air), hydration degree (heptahydrate and anhydrous), sample mass, and boat material (platinum, quartz, and ceramic). The results indicate that the use of platinum boats as sample holder led to a catalytic effect in the decomposition, reducing the temperature in which the sample degrades, but still using the same reaction steps already displayed. Soto-Díaz et al.[23] observed a similar behavior when using Pd catalysts.

Moreover, the atmosphere also had an impact, as the SO_3 dissociates into SO_2 and O_2, the flow of air delays the dissociation of SO_3, and shifts the decomposition of zinc sulfate to higher temperatures. This result was also observed in the work of Tagawa[58] using different metal sulfates. On the other hand, Mu and Perlmutter[24] pointed out in their studies that the atmosphere composition had no impact in the decomposition temperature, but did not report the temperatures of their studies in air atmosphere.

3.2.1 Kinetic studies

Similar to potassium alum, there are many kinetic studies regarding the thermal decomposition of zinc sulfate. On the other hand, the presence of the intermediate phase ($\mathrm{ZnO}\cdot 2\,\mathrm{ZnSO_4}$) between the decomposition of $ZnSO_4$ and formation of ZnO makes it challenging to properly model the decomposition process. The experimental conditions used also present variations, such as different atmospheres, isothermal or dynamic heating runs in TGA. Moreover, some authors chose to study the decomposition of $ZnSO_4$ and $\mathrm{ZnO}\cdot 2\,\mathrm{ZnSO_4}$ separately, synthesizing the latter.

Aside from the difference in the experimental conditions, the modeling techniques used also showed some differences. The graphical methods are influenced as the desulfation reactions occurs in two separate steps (Equations 3-13 and 3-14), therefore perform the segmentation can be somewhat troublesome when using higher heating rates. In the case of the isothermal studies, the challenge is to identify the change in the slope caused by the formation of $\mathrm{ZnO}\cdot 2\,\mathrm{ZnSO_4}$ and its further decomposition.

In the work of Ingraham and Marier,[29] the were used cylindrical pellets of ZnSO4 and ZnO.ZnSO4 to study the processes separately, using dynamic

heating in the temperature of 500 °C to 900 °C, with nitrogen as the carrier gas. They identified two different phases of ZnSO4 ($\alpha - ZnSO_4$ and $\beta - ZnSO_4$), transitioning around 755 °C. The activation energies were determined using linear Arrhenius plot, yielding 209 kJ.mol^{-1} and 242.4 kJ.mol^{-1} for the decomposition of $\beta - ZnSO_4$ and $ZnO \cdot 2\,ZnSO_4$, respectively.

Tagawa and Saijo[59] also used cylindrical pellets of different sulfates to evaluate their kinetics, but using isothermal runs in inert atmosphere. The authors identified the $ZnO \cdot 2\,ZnSO_4$ using XRD analysis. The reported activation energies for the decomposition of zinc sulfate and zinc sulfate were 238.1 kJ.mol^{-1} and 274.8 kJ.mol^{-1}, respectively.

Ibanez et al.[56] performed their tests using an isothermal balance in temperatures between 900 °C and 980 °C. The authors used samples of pure zinc sulfate and pure zinc oxysulfate to evaluate the activation energy. In their studies using pure $ZnSO_4$, the change in the slope is noticeable in conversion versus time plots around 33 % of conversion. However, as the temperature of the experiment increased, the change in the slope becomes imperceptible. As expected, the runs with pure $ZnO \cdot 2\,ZnSO_4$ did not present any change in slope throughout the extension of the experiment. The authors determined 305.9 kJ.mol^{-1} and 318.9 kJ.mol^{-1} as the activation energies for the decomposition of zinc sulfate and zinc oxysulfate, respectively. The Law of Nuclei Formation was used to describe the process.

Narayan, Tabatabaie-Raissi and Antal[25] performed a meticulous study evaluating four different variables that could impact the kinetics of zinc sulfate thermal decomposition: sample size, water of hydration, boat material, and carrier gas. The decrease in the sample size (24 mg to 16 mg) shifted the temperature to lower regions by about 20 °C. This result is disagrees with the one reported by Mu and Perlmutter,[24] whose stated that no difference in the decomposition temperature was noted when changing the sample size. However, Mu and Perlmutter[24] did not present any numerical or graphical representation to support this result. The increase in the amount of reactant used in the experiments lead to changes in the heat and mass transfer, which may compromise the results.[25,56,57]

The kinetic results were obtained using the Friedman equation combined with a nonlinear least-squared algorithm to determine the kinetic parameters in the different conditions evaluated. The activation energy for the thermal decomposition of $ZnSO_4$ ranged from 227 kJ.mol^{-1} to 298 kJ.mol^{-1}, with the lowest value corresponding to the use of a platinum boat, which is accounted to a catalytic effect. The activation energies of the thermal decomposition of $ZnO \cdot 2\,ZnSO_4$ varied from 252 kJ.mol^{-1} to 315 kJ.mol^{-1}. In the matter of the

reaction order, the authors reported that the thermal decomposition of zinc sulfate had an overall apparent order equal to unity, whereas the apparent reaction order of the thermal decomposition of zinc oxysulfate is equal to zero.[25]

The work of Mu and Perlmutter[24] evaluated the thermal decomposition of various metal sulfates, testing the effect of different additives, such as carbon, different oxides and salts. The decomposition temperature decreased in all cases in which any additive was involved. The authors also reported an activation energy of 351.4 kJ.mol^{-1} and a reaction order of $\frac{2}{3}$ for the decomposition of anhydrous zinc sulfate.

The difficulty of modeling a more complex system is shown in the work of Straszko, Olszak-Humienik and Mozejko.[34] The authors used different model-free equations to obtain the activation energies of each step in the thermal decomposition (dehydration and desulfation) showed in Equations 3-10 to 3-14. A requirement to determine the kinetic parameters is to segment all the reactions in the TGA curve, which can be difficult as it is uncertain to define exactly when one reaction stopped and another one has started. The results indicate that the decomposition of $ZnSO_4$ is controlled by random nucleation model with an activation energy 261 kJ.mol^{-1}. The decomposition of zinc oxysulfate is controlled either by three-dimensional diffusion model or contracting volume model, with activation energies of 1100 kJ.mol^{-1} and 530 kJ.mol^{-1}, respectively.

More recently, Kurban et al.[61] used a graphical method to model the decomposition of zinc sulfate with and without a Pd catalyst. The authors concluded that the reaction takes place in a single-step reaction, a behavior also observed in the work of Narayan, Tabatabaie-Raissi and Antal[25] when using platinum boats. The work findings show the complexity in segmenting the different reactions, as it is needed to use a graphical approach. The activation energies determined in the absence of the Pd catalyst were 238 and 368 kJ.mol^{-1} for the decomposition of $ZnSO_4$ and $ZnO \cdot 2\,ZnSO_4$, respectively. In the presence of the catalyst, the activation energy was 204 kJ.mol^{-1}. The reaction order in both cases were around 1.7.

3.3 Iron sulfate

Iron (II) sulfate is a green compound in its heptahydrate form, having other hydration degrees, with the tetra- and the monohydrate being the most common ones.[54] The dehydration of iron (II) sulfate heptahydrate ($FeSO_4 \cdot 7\,H_2O$) takes place in multiple steps.[62] First, the 3 mol of water

molecules are removed around 70 °C, forming the tetrahydrate compound ($FeSO_4 \cdot 4\,H_2O$). Next, around 100 °C, another 3 mol of water molecules leave the structure, yielding the monohydrate salt ($FeSO_4 \cdot H_2O$). At last, the anhydrous salt is formed around 300 °C.[63] Other hydrate forms of iron (II) sulfates have been observed by Mitchell,[64] with the hexa- and pentahydrate compounds. The general dehydration reactions previously described is shown in Equations 3-15, 3-16, and 3-17.

$$FeSO_4 \cdot 7\,H_2O \xrightarrow[70\ ^\circ C]{\Delta} FeSO_4 \cdot 4\,H_2O + 3\,H_2O_{(g)} \tag{3-15}$$

$$FeSO_4 \cdot 4\,H_2O \xrightarrow[100\ ^\circ C]{\Delta} FeSO_4 \cdot H_2O + 3\,H_2O_{(g)} \tag{3-16}$$

$$FeSO_4 \cdot H_2O \xrightarrow[300\ ^\circ C]{\Delta} FeSO_4 + H_2O_{(g)} \tag{3-17}$$

The desulfation reactions of iron (II) sulfate is not well-defined, being highly dependent on the atmosphere composition.[65] Kanari et al.[66] studied the thermal decomposition under inert (N_2) and oxidative (O_2 and $O_2 + Cl_2$) atmospheres using TGA. In the case of the inert atmosphere, the $FeSO_4$ phase decomposes directly to Fe_2O_3. On the other hand, the decomposition under oxidative atmosphere displayed a different phase, $FeOHSO_4$,[67] which can be accounted by the oxidation between O_2 and the monohydrate iron (II) sulfate.[68]

Under oxidative atmosphere, the same $FeOHSO_4$ was observed by different authors.[65,68–73] These studies also suggests that the anhydrous $FeSO_4$ formed oxidizes forming an oxysulfate phase, $Fe_2O(SO_4)_2$. This last phase further decomposes into iron (III) sulfate ($Fe_2(SO_4)_3$) and hematite (Fe_2O_3). The general reaction steps of decomposition under oxidative atmosphere is shown in Equations 3-18, 3-19, and 3-20.

$$FeSO_4 \cdot H_2O + \frac{1}{4}\,O_2 \xrightarrow{\Delta} FeOHSO_4 + \frac{1}{2}\,H_2O_{(g)} \tag{3-18}$$

$$FeOHSO_4 \xrightarrow{\Delta} \frac{1}{2}\,Fe_2O(SO_4)_2 + \frac{1}{2}\,H_2O_{(g)} \tag{3-19}$$

$$\frac{1}{2}\,Fe_2O(SO_4)_2 \xrightarrow{\Delta} Fe_2O_3 + SO_{3(g)} \tag{3-20}$$

Lacalamita et al.[74] performed the thermal decomposition of iron (II) sulfate heptahydrate under N_2 atmosphere using TGA. The authors performed *in-situ* XRD analysis at different temperature steps, identifying the present phases using the Rietveld method. The dehydration takes place as shown in Equations 3-15, 3-16, and 3-17. They did not report the presence of iron oxysulfate, concluding that the $FeOHSO_4$ phase decomposes directly into $Fe_2(SO_4)_3$ and Fe_2O_3. However, even though the $Fe_2O(SO_4)_2$ phase is not present, it can be seen as a mixture of anhydrous iron (II) sulfate and

hematite in a certain proportion. The last step of the decomposition represents the formation of hematite from $Fe_2(SO_4)_3$. The reaction steps is shown in Equations 3-21, 3-22, and 3-23.

$$FeSO_4 \cdot H_2O + \frac{1}{4}\,O_2 \xrightarrow{\Delta} FeOHSO_4 + \frac{1}{2}\,H_2O_{(g)} \tag{3-21}$$

$$FeOHSO_4 \xrightarrow{\Delta} \frac{1}{3}\,Fe_2(SO_4)_3 + \frac{1}{6}\,Fe_2O_3 + \frac{1}{2}\,H_2O_{(g)} \tag{3-22}$$

$$\frac{1}{3}\,Fe_2(SO_4)_3 \xrightarrow{\Delta} \frac{1}{3}\,Fe_2O_3 + SO_{2(g)} + \frac{1}{2}\,O_{2(g)} \tag{3-23}$$

Despite the XRD analysis, the proposed reaction steps by Lacalamita et al.[74] does not agree with information obtained from the TGA signal. By their XRD results, there is no presence of anhydrous iron (II) sulfate in the reactions, but they also report that around 260 to 300 °C, there is a weight loss of around 4 %, which would correspond to the last water molecule in the hydrated salt. Other authors[66,71,75,76] reported that the $FeSO_4 \cdot 7\,H_2O$ dehydrates in three different steps (3-15, 3-16, and 3-17) to anhydrous $FeSO_4$, and then the decomposition takes place in two steps, to ferric sulfate and ferric oxide (Equations 3-24, 3-25).

$$FeSO_4 \xrightarrow{\Delta} \frac{1}{6}\,Fe_2(SO_4)_3 + \frac{1}{3}\,Fe_2O_3 + \frac{1}{2}\,SO_{2(g)} \tag{3-24}$$

$$\frac{1}{6}\,Fe_2(SO_4)_3 \xrightarrow{\Delta} \frac{1}{6}\,Fe_2O_3 + \frac{1}{2}\,SO_{2(g)} + \frac{1}{4}\,O_{2(g)} \tag{3-25}$$

3.3.1 Kinetic studies

The kinetic studies concerning the thermal decomposition $FeSO_4$ are similar to what is observed in the cases of potassium alum and $ZnSO_4$, many studies with different experimental conditions and modeling techniques. However, the decomposition of iron (II) sulfate has the presence of more intermediate compounds ($FeOHSO_4$ and $Fe_2O(SO_4)_2$), and the iron (III) sulfate. Moreover, unlike what was seen in the previous sulfates, the atmosphere composition has direct impact in the decomposition reaction steps as previously reported.

Johnson and Gallagher[77] performed thermogravimetric runs with $FeSO_4$ using both O_2 and N_2 atmospheres, evidencing the different reaction steps that take place when changing the atmosphere composition. The authors fitted the experimental data in contracting geometry model, resulting in activation energies ranging from 188.1 to 255 $kJ.mol^{-1}$, with the values being lower in O_2 atmosphere than with N_2.

More recently, Huang et al.[78] studied the thermal decomposition of anhydrous ferrous sulfate with pyrite under nitrogen atmosphere. The authors

concluded that the addition of pyrite (mainly the presence of FeS_2) increased the desulfation rate of $FeSO_4$. Moreover, the presence of the different iron oxides (Fe_2O_3, Fe_3O_4, and FeO) catalyzed the thermal decomposition reactions. The kinetic analysis was made using different model-free equations. The extended Prout-Tompkins had the best result, with an activation energy of 244.34 kJ.mol^{-1} and a reaction order of 2.16. Kubo, Taniguchi and Shirasaki[79] observed a similar model, but with a lower activation energy (135.4 kJ.mol^{-1}).

In the work of Kanari et al.,[66] two different $FeSO_4$ samples (industrial and laboratory) under nitrogen atmosphere using thermogravimetric balance. The samples presented differences in their compositions, with the industrial sample being composed of iron (II), whereas the laboratory sample had a composition of both iron (II) and iron (III). The kinetic study was made using Arrhenius plots (isothermal decomposition studies), resulting in activation energies of 262 kJ.mol^{-1} and 238 kJ.mol^{-1} for the industrial and laboratory samples, respectively.

In a different context, Swamy, Prasad and contributors[63,68,69,80–82] published various of studies regarding the thermal decomposition of $FeSO_4$, $Fe_2(SO_4)_3$, and other intermediate compounds ($FeOHSO_4$, and $Fe_2O(SO_4)_2$) in air atmosphere. Prasad[82] reported activation energies in the range 247 to 297 kJ.mol^{-1} for the thermal decomposition of iron (III) sulfate, with the difference accounted by method in which the different samples were prepared.

In the later works of Prasad,[80–83] the author performed various runs with different starting materials using model-free equations to determine the activation energies. The results indicate that the decomposition of $FeOHSO_4$ and $Fe_2O(SO_4)_2$ are controlled by two-dimensional diffusion (246 kJ.mol^{-1}) and one-dimensional diffusion (619 kJ.mol^{-1}), respectively.

The thermal decomposition of iron (II) sulfate in air was studied using Zsako's statistical method.[63] The authors defined the decomposition in three different steps, with the first two concerning the dehydration of $FeSO_4 \cdot 7\,H_2O$, and the third as the decomposition of $Fe_2O(SO_4)_2$. The results indicate that the decomposition of iron oxysulfate has an activation energy of 552 kJ.mol^{-1}.

Kolta and Askar,[84] and Tagawa and Saijo[59] performed their kinetic studies using iron (III) sulfate. However, the experimental conditions were different. The first used TGA under air atmosphere, whereas the latter used cylindrical pellets under inert atmosphere. Despite both using the Arrhenius plot to determine the activation energy, the values are discrepant, 106 kJ.mol^{-1} in the work of Kolta and Askar[84] and 211.8 kJ.mol^{-1} in the work of Tagawa and Saijo.[59] Wu et al.[85] used a similar approach and found 114.6 kJ.mol^{-1} in thermal decomposition of $Fe_2(SO_4)_3$.

4
Theoretical basis

4.1
Thermal decomposition modeling

4.1.1
Graphical method

Among the different models that can used for modeling reaction kinetics, Vachuška and Vobořil,[36] which was further revisited by Speyer,[86] proposed a correlation for the decomposition of solids. The decomposition rate defined by this model can be seen in Equation 4-1.

$$\frac{df}{dt} = m_0^{n-1}(1-f)^n k_0 \exp\left(-\frac{E_a}{RT}\right) \tag{4-1}$$

where f is the conversion of the reaction, t is the time, m_0 is the initial mass of the sample as the decomposition reaction starts, n is the reaction order, k_0 is the pre-exponential factor, E_a is the activation energy, R is the universal gas constant, and T is the temperature.

For convenience, Equation 4-1 can be linearized by taking the logarithm as in Equation 4-2.

$$\ln\frac{df}{dt} = \ln\left[k_0 m_0^{n-1}\right] + n\ln(1-f) - \frac{E_a}{RT} \tag{4-2}$$

Then taking a time derivative, yields Equation 4-3.

$$\frac{d}{dt}\left(\ln\frac{df}{dt}\right) = \frac{d^2f/dt^2}{df/dt} = \frac{-n(df/dt)}{1-f} + \frac{E_a}{RT^2}\frac{dT}{dt} \tag{4-3}$$

At last, the relationship between temperature and time (Equation 4-4) is added, resulting in the linear Equation 4-5.

$$T = (\phi t + T_r) \tag{4-4}$$

$$(\phi t + T_r)^2\frac{d^2f/dt^2}{df/dt} = -n\left[\frac{(\phi t + T_r)^2(df/dt)}{1-f}\right] + \frac{E_a\phi}{R} \tag{4-5}$$

where ϕ is the heating rate and T_r is the reference room temperature.

The main advantage of using the linear form is that the activation energy (intercept) and the reaction order (slope) can be easily determined by plotting $\frac{(\phi t+T_r)^2(df/dt)}{1-f}$ versus $(\phi t + T_r)^2\frac{d^2f/dt^2}{df/dt}$. The linear plot of the decomposition of $NiSO_4$ under inert atmosphere is displayed in Figure 4.1. By the coefficients, the reaction order is 1.61 and the activation energy is 279.1 kJ.mol^{-1}.

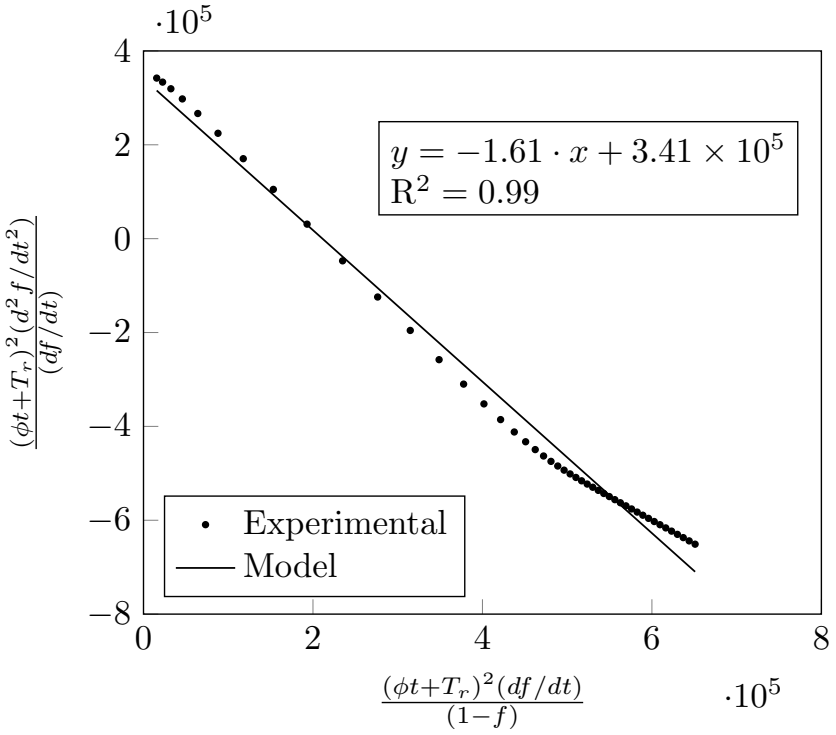

Figure 4.1: Linear plot of the decomposition of $NiSO_4$ under inert atmosphere. Experimental data obtained from Bejaoui et al..[87]

However, the use of Equation 4-5 has some concerns. First, it requires the numerical values of the first ($\frac{df}{dt}$) and second derivatives ($\frac{d^2f}{dt^2}$). Considering that the TGA signal has some noise, the propagation of the error will automatically be implicit in the derivatives. Moreover, the linear form can only be used in simple systems. For more complex systems, with reactions happening close to each other or occurring simultaneously, Equation 4-5 fails to fully describe the system.

In some cases, such as the decomposition of zinc sulfate, segment the different reactions is not a simple task, as it is troublesome to define the end of one reaction and the beginning of the next one. Therefore, to be able to avoid the mathematical approximations of the derivatives and apply the method in more complex systems, another approach is ought to be made.

The use of Equation 4-5 was proposed by Vachuška and Vobořil[36] not only because of the simplicity in obtaining the kinetic parameters (angular and linear coefficients), but also due to less computational effort. However, solving ordinary differential equations (ODE), such as Equation 4-1, is a much simpler task with modern computers. Moreover, using a system of ODEs allow the model to be used in more complex reactions, formulating one equation for each reaction step. It is necessary to have knowledge over the basic reaction steps of the decomposition reaction, and a method to estimate the kinetic

parameters of all the ODEs involved in the model.

4.1.2 Ordinary differential equations (ODE) method

To model more complex reaction steps (involving sequential or even simultaneous reactions occurring), a system of ODE can be proposed. Each differential equation concerns one reaction of the mechanism. Considering Equation 4-1, it concerns the conversion of a decomposition reaction that takes place in a single step, as in the case of nickel sulfate.

In some cases, multiple steps occur (such as $ZnSO_4$[24] and $FeSO_4$[66,74]) requiring new sets to evaluate the conversion of all the reactions involved. Thus, a different approach is made in these cases as seen in Equation 4-6. Each $\frac{df_i}{dt}$ equation in the set concerns a different reaction.[88–91]

$$\begin{cases} \dfrac{df_1}{dt} = \cdots \\ \dfrac{df_2}{dt} = \cdots \\ \vdots \\ \dfrac{df_n}{dt} = \cdots \end{cases} \tag{4-6}$$

Taking the case of copper sulfate as an example, the proposed mechanism of the decomposition reaction is shown in Equations 4-7 and 4-8.[24,60,92] The decomposition occurs in two steps, with the presence of an intermediate phase ($CuO \cdot CuSO_4$), unlike to what happens in simpler systems such as the nickel sulfate.

$$CuSO_4 \xrightarrow{\Delta} \frac{1}{2}\, CuO \cdot CuSO_4 + \frac{1}{2}\, SO_{3(g)} \tag{4-7}$$

$$\frac{1}{2}\, CuO \cdot CuSO_4 \xrightarrow{\Delta} CuO + \frac{1}{2}\, SO_{3(g)} \tag{4-8}$$

The graphical method displayed in Section 4.1.1 is not able to model describe the two reaction simultaneously. To determine the kinetic parameters, it would be necessary to segment the conversion curve into two.[61] The first one concerns the decomposition of $CuSO_4$, and the latter the decomposition of $CuO \cdot CuSO_4$. Despite the possibility to use the graphical method, the segmentation of the curves is not always precise and the results could be misleading.

Considering the Equations 4-7 and 4-8, the ODE system can be developed as shown in Equation 4-9. The first equation in the system is the same as displayed in Equation 4-1, but the second equation is modified to be dependent of the first one. This due to the nature of the thermal decomposition in multiple

steps. The $CuO \cdot CuSO_4$ phase can only be decomposed if it is previously formed, thus the second reaction's (Equation 4-8) conversion depends on the conversion of the first reaction (Equation 4-7).

$$\begin{cases} \dfrac{df_1}{dt} = m_{0,1}^{n_1}(1-f_1)^{n_1} k_{0,1} \exp\left(-\dfrac{E_{a,1}}{RT}\right) \\ \dfrac{df_2}{dt} = m_{0,2}^{n_2}(1-f_2)^{n_2} k_{0,2} \exp\left(-\dfrac{E_{a,2}}{RT}\right) - \\ \qquad \left[m_{0,1}^{n_1}(1-f_1)^{n_1} k_{0,1} \exp\left(-\dfrac{E_{a,1}}{RT}\right)\right] \end{cases} \tag{4-9}$$

By solving the ODE system, there are two conversion curves as outputs, f_1 and f_2. To describe the global conversion (f_{global}), it is necessary to attribute weights to each individual conversion (Equation 4-10). The weight values, w_1 and w_2, are determined according to the theoretical mass balance of the modeled reaction stages. In the case of copper, both values are equal to 0.5, as seen in the mechanism shown previously (Equations 4-7 and 4-8).

$$f_{\text{global}} = \sum_{i=1}^{n_r} w_i \times f_i \tag{4-10}$$

where n_r is the number of reactions evaluated in the mechanism, w_i is the weight of the ith reaction, f_i is the conversion of the ith reaction, and f_{global} is the global conversion of the reaction system.

The result of ODE system modeling is depicted in Figure 4.2, resulting in activation energies of 333 and 389 kJ.mol^{-1} for the decomposition of $CuSO_4$ and $CuO \cdot CuSO_4$, respectively.

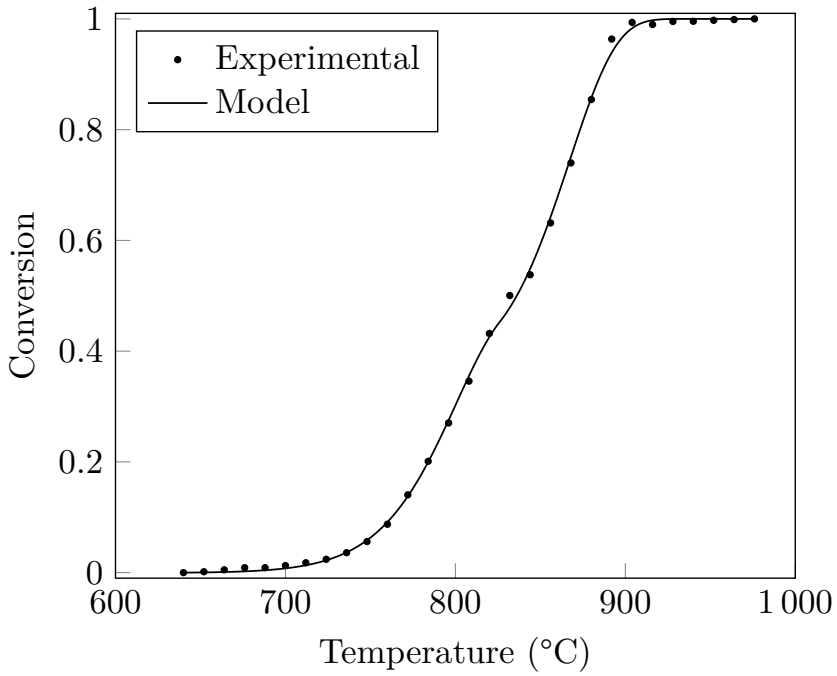

Figure 4.2: Modeling of the thermal decomposition of $CuSO_4$ under air atmosphere using the system of ODE. Experimental data obtained from Gadalla.[93]

By describing each reaction individually, the results of differential equation method can be seen with more details. Figure 4.3 displays the individual conversions (f_1 and f_2) as well as the global conversion (f_{global}).

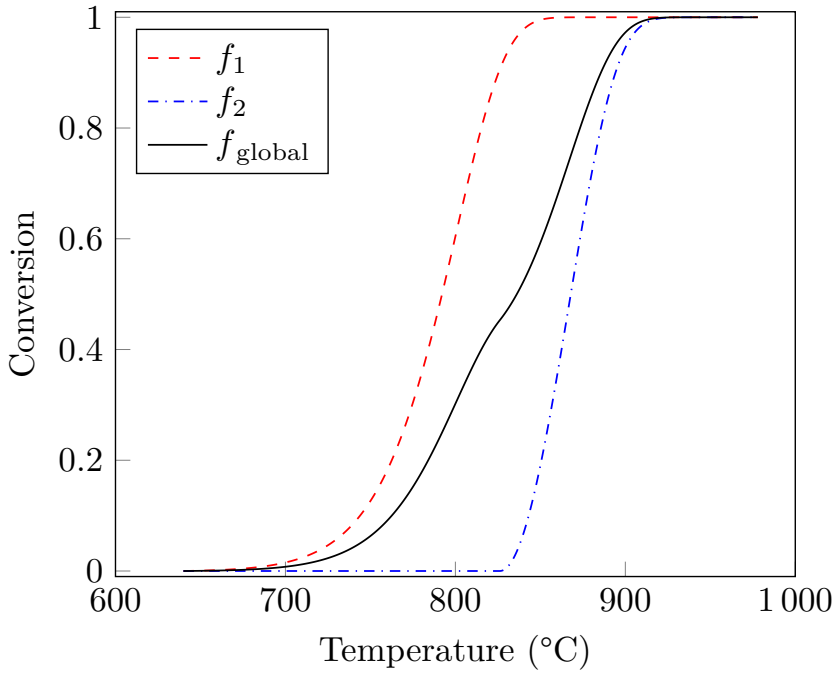

Figure 4.3: Individual and global conversions of the thermal decomposition of $CuSO_4$ under air atmosphere using the ODE system. Experimental data obtained from Gadalla.[93]

Unlike the graphical method, that determined the kinetic parameters by using slope and intercept values, the differential equations method require a way to estimate the kinetic parameters. A good estimation is needed to get a good agreement between model and experimental values. Moreover, by using Equation 4-1 coupled with parameter estimation instead of a graphical method, it is possible to determine the pre-exponential factor (k_0) value alongside the activation energy and reaction order.

Figures 4.4, 4.5, and 4.6 depict the effect of the three different kinetic parameters on the conversion curves obtained by solving Equation 4-1. The increase of the k_0 value causes the conversion to start at lower temperatures. In contrast, the increase in the E_a value makes the conversion to start at higher temperatures. Finally, the variation in n value does not change the temperature in which the reaction start, but rather the smoothness of the conversion curve. Therefore, for a proper fitting, the k_0 and E_a values act like a counterbalance to one another over the decomposition temperature, and the n value dictates if the transition is steep or gradual.

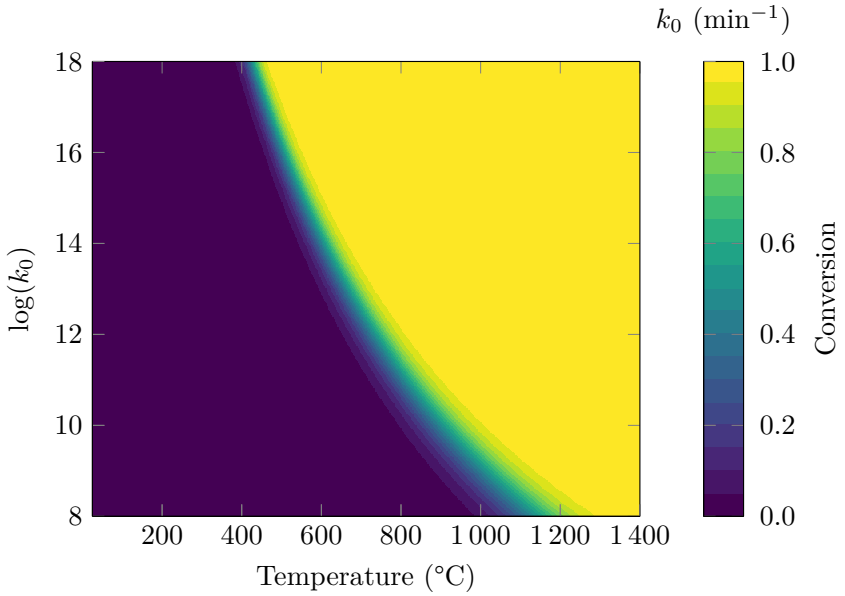

Figure 4.4: The effect of the k_0 value in conversion curves. $m_0 = 10$ mg, $E_a = 250$ kJ.mol^{-1}, and $n = 1.5$.

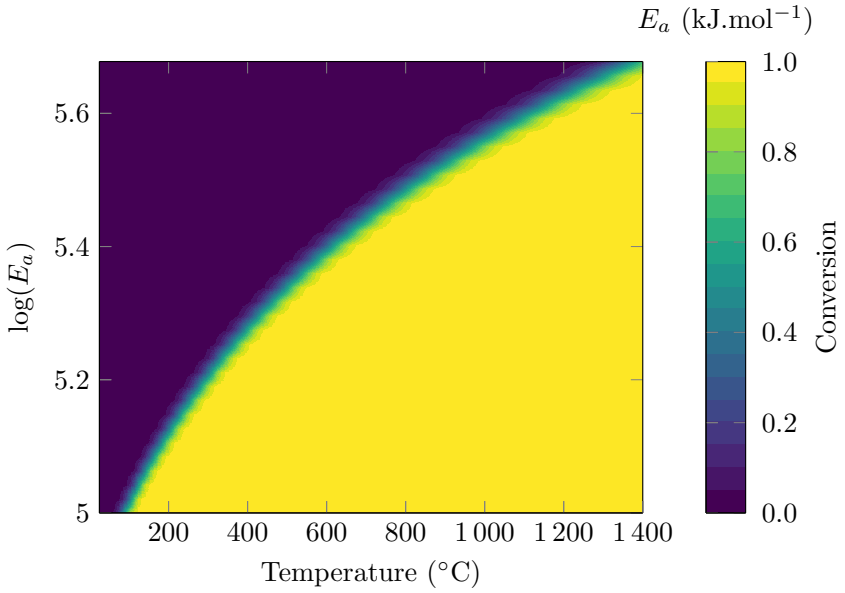

Figure 4.5: The effect of the E_a value in conversion curves. $m_0 = 10$ mg, $k_0 = 1 \times 10^{13}$ min^{-1}, and $n = 1.5$.

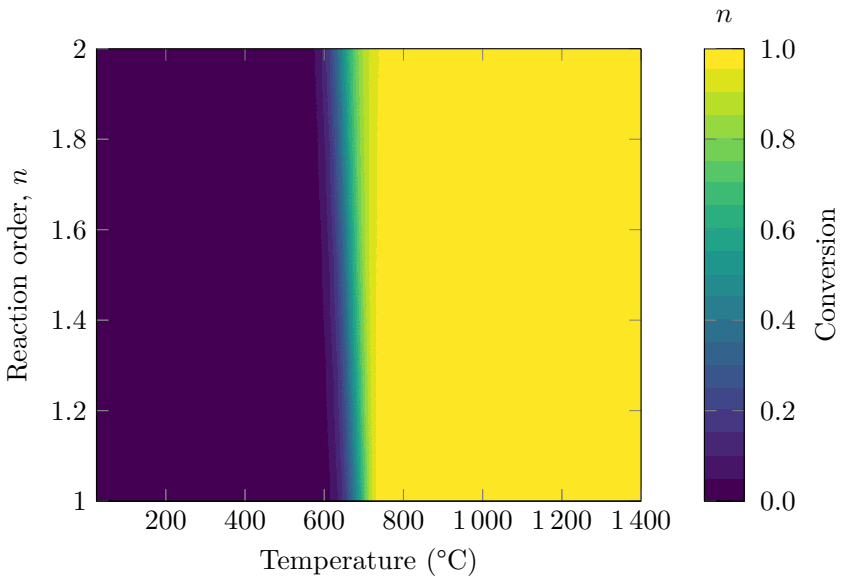

Figure 4.6: The effect of the n value in conversion curves. $m_0 = 10$ mg, $k_0 = 1 \times 10^{13}$ min^{-1}, and $E_a = 250$ kJ.mol^{-1}

The next section covers the parameter estimation algorithm used in the present work.

4.2 Parameter estimation

Two steps are necessary in the development of model. First, it is essential to define the relationship between the different variables involved in the system,

in other words, structuring the model. The next step is making the model being able to predict the results with quality. The latter is achieved by having the model's parameters well-tuned with the case study.[94,95]

The estimation of parameters comes as solution to minimize a global objective function, reducing to a minimal the differences between the experimental and model values. For example, if the model is structured as linear ($y = \alpha x + \beta$) and the objective function is defined as in Equation 4-11. The α and β parameters are estimated to bring the value of f_{Obj} to as low as possible (optimum).[95,96]

$$f_{\mathrm{Obj}} = \sum_{i=1}^{\mathrm{NE}} ({y_i}^{\mathrm{exp}} - {y_i}^{\mathrm{model}})^2 \tag{4-11}$$

where NE is the number of experiments, ${y_i}^{\mathrm{exp}}$ is the experimental value of the experiment i, and ${y_i}^{\mathrm{model}}$ is the value predicted by the model in the given experiment.

After the structuring of the model and the estimation of its parameters, the statistical analysis of the results is required. This last step is the benchmark that establishes if the model and the parameter estimation are of good quality.[94,95,97]

Therefore, a parameter estimation problem can be described in three steps:

1. Model structuring and definition of the objective function.
2. Minimization of the objective function (optimum value).
3. Statistical analysis of the estimated parameters.

4.2.1 Particle swarm optimization (PSO)

The PSO algorithm is a global optimization method first proposed by Kennedy and Eberhart.[98] The algorithm is based on the social aspect of animals. A common analogy made is a flock of birds flying in a determined space looking for food. None of the birds know the exact location of the food. But they can remember its own best site and the best place that any of the birds in the flock have already found. The birds then move towards the best location located by the flock.

In the algorithm, each individual is accounted as a particle with the coordinates correspondent to the parameters of the problem. A defined number of particles is placed in the desired search space (defining the upper and lower bounds for each coordinate). The objective function value is calculated for

every particle in each iteration. The particle with the lowest function value is considered the best global one. Furthermore, each particle can memorize which position had the best individual result. The movement of the particles is measured by considering its current value, its best personal position, and the swarm's best position. Throughout the optimization process, the particles have a tendency of moving towards the global minima of the objective function. The particles' velocity and position are show in Equations 4-12 and 4-13.

$$v_p^{k+1} = wv_p^k + c_1 r_1 (x_p{}^{\text{ind}} - x_p^k) + c_2 r_2 (x^{\text{global}} - x_p^k) \tag{4-12}$$

$$x_p^{k+1} = x_p^k + v_p^{k+1} \tag{4-13}$$

where v_p^k is the velocity of the particle p at the iteration k, x_p^k is the position of the particle p at the iteration k. $x_p{}^{\text{ind}}$ and x^{global} are the particle's best personal position and the swarm's best location, respectively. w, c_1, and c_2 are inertia and acceleration coefficients. r_1 and r_2 are random numbers from a uniform distribution in the range $[0, 1)$. Figure 4.7 displays how the particles' position and velocity are updated.

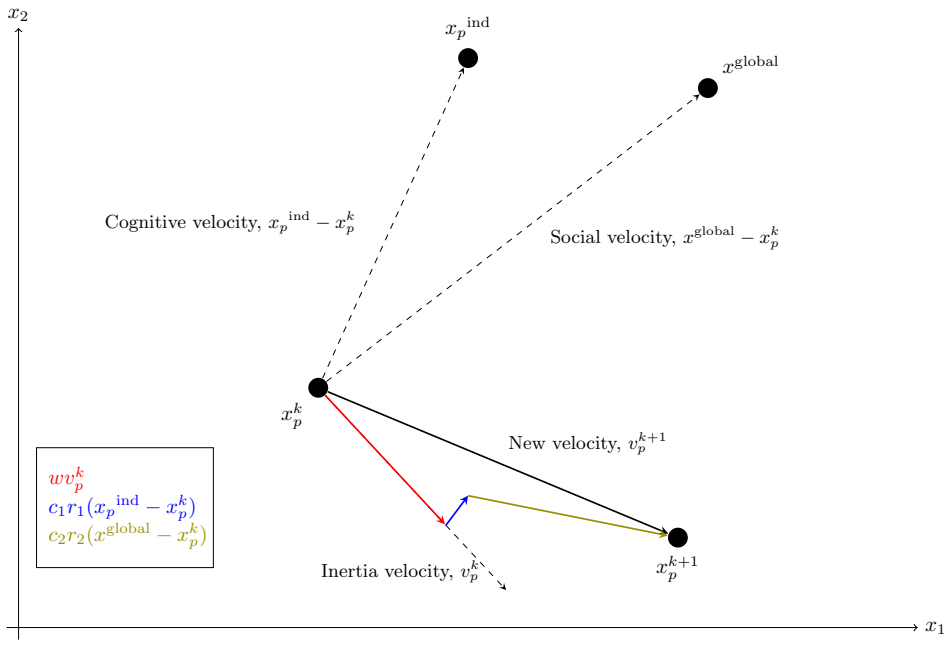

Figure 4.7: Update of the position and velocity of a particle in a two dimensions.

One advantage of using this optimization method is that is a derivative-free, such as gradient-descent or Newton, and is less dependent of the initial conditions, which makes it a simple and powerful tool to implement.[99,100] On the other hand, some cases can be time consuming as the each particle corresponds a set of parameters, with the necessity of a simulation to be made for each particle in every iteration. Nevertheless, this optimization method has been extensively used in chemical engineering problems, such as

polyremization.[96,101–103] Rego et al.[27] used the PSO algorithm to estimate the kinetic parameters of the thermal decomposition of potassium alum under inert atmosphere.

4.2.1.1 PSO parameters

An important aspect present in Equation 4-12 is the randomness associated with r_1 and r_2 values. These terms were not considered in the early works of Kennedy and Eberhart.[98] Without it, the authors observed that the swarm would settle, meaning that the particle were not moving. Therefore, they introduced the random terms ('craziness'), giving a stochastic characteristic to the method. Moreover, other PSO parameters are also noteworthy.

– Inertia weight constant (w): This value influences directly the first term in Equation 4-12 (wv_p^k), which corresponds to the inertial velocity term. The inertia constant has influence in how the previous velocity will affect the next velocity value.[104,105] Higher values ($w \geq 1$) tend to make the particle always be in inertia condition, not changing directions, which may be interesting for a complete global search. On the other hand, low inertia constant values ($0 \leq w < 1$) make the search for local minimum values easier, as more areas are searched due to the change in directions.[106] A good approach is to make the inertia constant a dynamic parameter throughout the optimization. At first, the value is set to a high value, and is lowered as the iterations are processed as seen in Equation 4-14.

$$w = w_{initial} - (w_{final} - w_{initial}) \times \frac{it}{it_{\max}} \tag{4-14}$$

– Acceleration coefficients (c_1 and c_2): These parameters influence the cognitive ($x_p{}^{\text{ind}} - x_p^k$) and social ($x^{\text{global}} - x_p^k$). The first one is related related to the value of the current particle's position and the best position it already had in the optimization. Therefore, as the particle move away from its best position, the cognitive term increases pulling the particle towards its best position. Therefore, the c_1 parameter is a weight to the individual-cognitive aspect of the particle.[105,106]

A similar approach is made with social aspect. As the particle gets far from the best position of the swarm (x^{global}) , the social term gets higher and makes the particle be attracted to the best position. This behavior allows the communication among all the particles to know which position

is the best one. Thus, the c_2 parameter is a weight for the social aspect of the swarm.[105,106]

There is no certain value established for these two parameters, usually being optimized empirically.[107] If they both are zero, then Equation 4-12 is reduced to the inertial velocity. Different values for c_1 and c_2 give different influences to the cognitive aspects. Both having the same values make all the particles being attracted to equally to both aspects.[108]

– Iteration number ($it_{\max}$): The total number of iterations in a given optimization process is not defined, being adopted with each individual problem. If the number is too low, the algorithm stops before the global minima is achieved by the particles. On the other hand, if the number is too high, the computational effort increases if the maximum iteration numbers is the stop criteria adopted for the optimization.[107,108]
– Swarm size (n): It defines number of particles that are present in optimization. A small quantity of particles can make some regions of the search space to be poorly investigated, possibly neglecting some promising minima locations, whereas a huge amount of particles can make all the areas properly searchable, but also increasing the computational time for the optimization to be performed, also making the algorithm inefficient. According to Talukder,[108] a proper number of particles is in range $[20, 60]$ in most cases.

4.2.1.2 Statistical evaluation

Finding the optimal parameters value does not represent the end of the estimation process. By the end of the algorithm described in the previous sections, the best fitted curve can be plotted, but other non-optimal data points are also viable answers to the estimation problem. By keeping track of all the particles' coordinates and its correspondent errors, it is possible to evaluate the uncertainties regarding the best particle's position and f_{Obj} minimum value.[109,110]

Building a confidence region is one possible way to do this type of evaluation. As the PSO algorithm evaluates the objective function for every particle in all the iterations, there is a huge set of data in the neighborhood of the optimal point at the end of estimation. Considering an confidence interval, it is possible to select the data points that are within the interval.[96,110] Beale[111] proposed the use of Equation 4-15 for building the confidence region.

$$f_{\mathrm{Obj}}(\underset{\sim}{x}) \leq f_{\mathrm{Obj}}(\underset{\sim}{x}_{\mathrm{opt}}) \left(1 + \frac{\mathrm{NP}}{\mathrm{N} - \mathrm{NP}} F^{1-\varphi}_{\mathrm{NP},\,\mathrm{N-NP}}\right) \tag{4-15}$$

where $\underset{\sim}{x}$ is array of estimated parameters, $\underset{\sim}{x}_{\text{opt}}$ is array of the optimal parameters found at the end of the estimation algorithm, NP is the number of estimated parameters, N is the amount of experimental data, and $1-\varphi$ is the confidence interval (0.95 in the present work). It is worthy mentioning that the N−NP, represents the degrees of freedom.

5
Materials and methods

5.1
Thermodynamic assessments

All the thermodynamic analyses were performed using HSC Chemistry 10.[112] In all cases, the initial composition consisted of 1 kmol of the hydrated sulfate species: $KAl(SO_4)_2 \cdot 12\,H_2O$, $ZnSO_4 \cdot 7\,H_2O$, and $FeSO_4 \cdot 7\,H_2O$. The atmosphere composition was considered as inert by only using (N_2) as the initial gaseous component. The list of all the phases, reactants and products, considered in each case study are detailed in further topics.

In all cases, the temperature range used was from 25 °C to 1400 °C using 250 steps to calculate the equilibrium composition. This temperature range was chosen to match the one used in the TG runs. The pressure was considered as 1.0 atm throughout the simulation, considering the gas flow present in the TG balance. The gas phases were considered to be ideal due to the low pressure and high temperature. Moreover, the solid phases were considered pure and stoichiometric.

5.2
Thermogravimetric analysis

The thermogravimetric analysis runs followed a dynamic regime, using a heating rate of 10 °C.min^{-1}, which provides precise TG signal with in reasonable run times. The analyzes were carried out in thermogravimetric balance (Netzsch model STA 449 F3 Jupyter) using inert atmosphere (N_2). The maximum temperature used in each experiment dependend on the initial material used. The samples were prepared using a mortar and a pestle to have a uniform material before transferring to the crucible of the thermogravimetric balance. Around 10 mg of reactant was used in each run.

The properties of every chemical used in the work are as follows:

- Aluminum sulfate – $Al_2(SO_4)_3 \cdot 18\,H_2O$ (Vetec, 99 %, 1690 kg.m^{-3})
- Potassium sulfate – K_2SO_4 (Merck, >99 %, 800 kg.m^{-3})
- Potassium alum – $KAl(SO_4)_2 \cdot 12\,H_2O$ (Merck, 99 %, 900 kg.m^{-3})
- Zinc sulfate - $ZnSO_4 \cdot 7\,H_2O$ (Sigma-Aldrich, >99.5%, 1970 kg.m^{-3})
- Iron (II) sulfate - $FeSO_4 \cdot 7\,H_2O$ (Proquímio, >99 %, 1895 kg.m^{-3})
- Nitrogen – N_2 (Linde AG, 99.9 %)

5.3
Modeling and optimization

All the simulations were performed in a microcomputer with the following specifications: Intel Core i7-8700 CPU @ 3.20 GHz and 32 GB of RAM. All the codes were written in Python 3.

The modeling used was the one concerning the set of ordinary differential equations (Section 4.1.2). The numerical method used to solve the ODE system was 'dopri5' of the SciPy library, a modified 4^{th} order explicit Runge-Kutta.[113]

All the parameters used in the PSO algorithm were defined empirically. The number of particles used was 45. The acceleration coefficients, c_1 and c_2, were both set as 1.0, and the initial inertia weight constant (w) was 0.9. As stop criteria, the sum all the velocities of all the particles was used (with a tolerance of 0.1), and the maximum number of iterations was set to 500. Figure 5.1 depicts the PSO algorithm used.

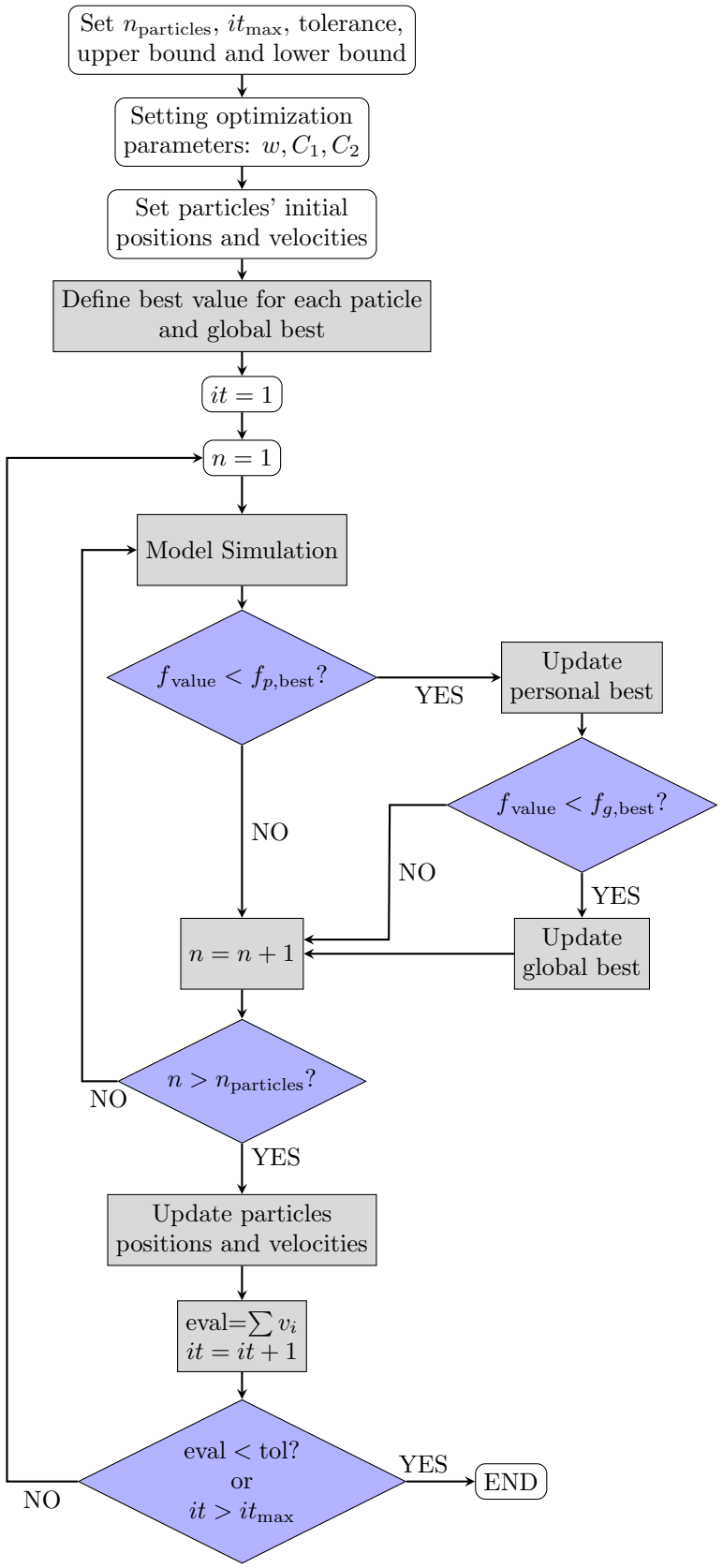

Figure 5.1: Flowchart of the PSO algorithm used in the present work.

6
Results and discussion

6.1
Potassium alum

6.1.1
Thermodynamic assessments

The solid and gaseous phases considered in the thermodynamic equilibrium simulations of the thermal decomposition of potassium alum are as follows:

- Solid phases: $KAl(SO_4)_2 \cdot 12\,H_2O$, $KAl(SO_4)_2 \cdot 3\,H_2O$, $KAl(SO_4)_2$, $Al_2(SO_4)_3$, K_2SO_4, Al_2O_3, $KHSO_4$, $K_2S_2O_7$.
- Gas species: N_2, H_2O, SO_3, SO_2, O_2, H_2SO_4, H_2S, H_2.

Figure 6.1 depicts the equilibrium composition of the solid phases of the thermal decomposition of 1.0 mole of potassium sulfate dodecahydrate as a function of the temperature. As expected, the first stage of the graph (from 25 °C to 200 °C) represents the dehydration process until the anhydrous potassium alum is obtained.

The dehydration stage occurs in two different steps. At first, the structure 'loses' 9 water molecules, which yields a trihydrated species. The further increase in temperature causes the last water molecules to sublimate, resulting in the potassium alum in its anhydrous state. The multi-step dehydration behaviour can be seen in the TGA curves of the thermal decomposition studies of Apte, Kiran and Chernosky,[26] Wojciechowska, Wojciechowski and Kamiński,[35] Kardos et al.,[39] and Souza et al..[21] The dehydration temperatures agree with the TG curves reported by Kardos et al.[39] and Souza et al.[21] in which the anhydrous phase is reached around 200 °C. The complete dehydration of $KAl(SO_4)_2 \cdot 12\,H_2O$ is theoretically described by Equations 3-1 and 3-2.

$$KAl(SO_4)_2 \cdot 12\,H_2O \xrightarrow{\Delta} KAl(SO_4)_2 \cdot 3\,H_2O + 9\,H_2O_{(g)} \tag{3-1}$$

$$KAl(SO_4)_2 \cdot 3\,H_2O \xrightarrow{\Delta} KAl(SO_4)_2 + 3\,H_2O_{(g)} \tag{3-2}$$

From 200 °C onward, the anhydrous potassium alum decomposes into three different sulfates: $Al_2(SO_4)_3$, K_2SO_4 and $KHSO_4$. The last one appears to be an intermediate phase, as it seems to be consumed as the temperature

increases, similar to the aluminum potassium. Souza et al.[21] reported another phase in an XRD analysis, $K_3H(SO_4)_2$, which could be explained by the formation of a solid solution of $KHSO_4$ and K_2SO_4 mixtures (Equation 6-1). $KHSO_4$ further decomposes into potassium sulfate, as seen by Equations 6-2 and 6-3.

$$K_3H(SO_4)_2 \xrightarrow{\Delta} KHSO_4 + K_2SO_4 \tag{6-1}$$

$$KHSO_4 \xrightarrow{\Delta} \frac{1}{2}\,K_2S_2O_7 + H_2O_{(g)} \tag{6-2}$$

$$\frac{1}{2}\,K_2S_2O_7 \xrightarrow{\Delta} \frac{1}{2}\,K_2SO_4 + SO_{3(g)} \tag{6-3}$$

The final product of the hydrated potassium alum's thermal decomposition is aluminum oxide (Al_2O_3) and potassium sulfate (K_2SO_4), which are very stable components. The complete thermal decomposition of anhydrous potassium alum could be described globally as in Equations 6-4, 6-5, and 6-6. The first one concerns a decomposition reaction with no mass loss, as both products constitute a solid phase.

$$KAl(SO_4)_2 \xrightarrow{\Delta} \frac{1}{2}\,K_2SO_4 + \frac{1}{2}\,Al_2(SO_4)_3 \tag{6-4}$$

$$\frac{1}{2}\,Al_2(SO_4)_3 \xrightarrow{\Delta} \frac{1}{2}\,Al_2O_3 + \frac{3}{2}\,SO_{3(g)} \tag{6-5}$$

$$SO_{3(g)} \xrightarrow{\Delta} SO_{2(g)} + \frac{1}{2}\,O_{2(g)} \tag{6-6}$$

A noticeable observation ought to be made about the presence of K_2SO_4 in thermal decomposition. As Apte et al.[26] reported, the presence of this salt reduced the temperature of the aluminum sulfate decomposition. Therefore, the potassium sulfate could have a catalytic effect in the system, which can be better observed through TG analysis.

The thermodynamic analysis of the gas phase can be seen in Figure 6.2. The graph has a much simpler approach than the one depicted in Figure 6.1. At first, there is a high amount of water due to the dehydration of the potassium alum until 500 °C. After that, the formation of SO_2, SO_3 and O_2 (Equations 6-5 and 6-6) is observed as the sulfates start to decompose and promoting water dilution in the reactional atmosphere. Despite the consideration of the other gas components, none of them had significant representation in the present analysis.

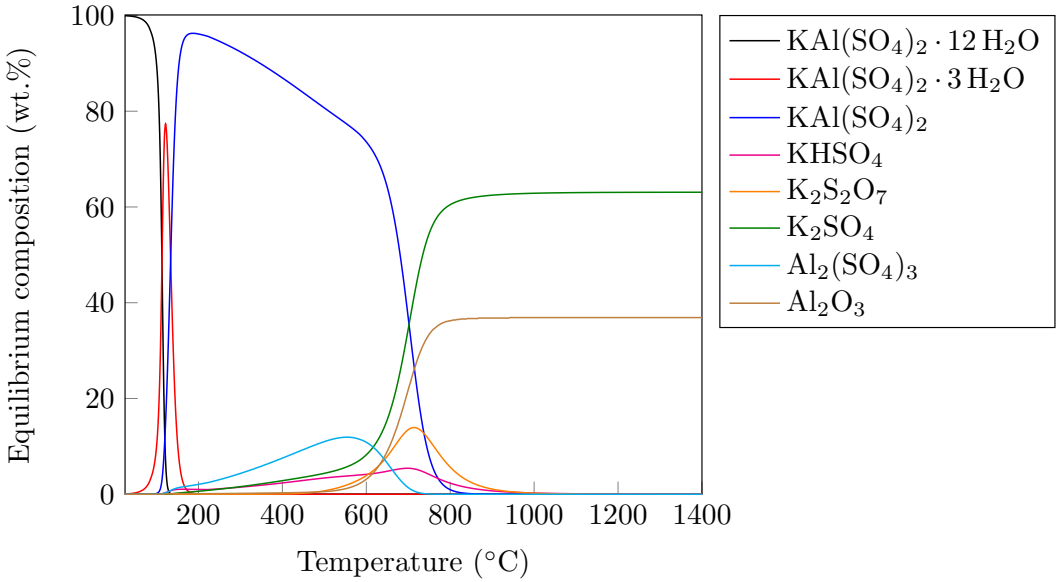

Figure 6.1: Equilibrium composition (wt.%) of the solid phases of the thermal decomposition of potassium alum dodecahydrate as a function of the temperature.

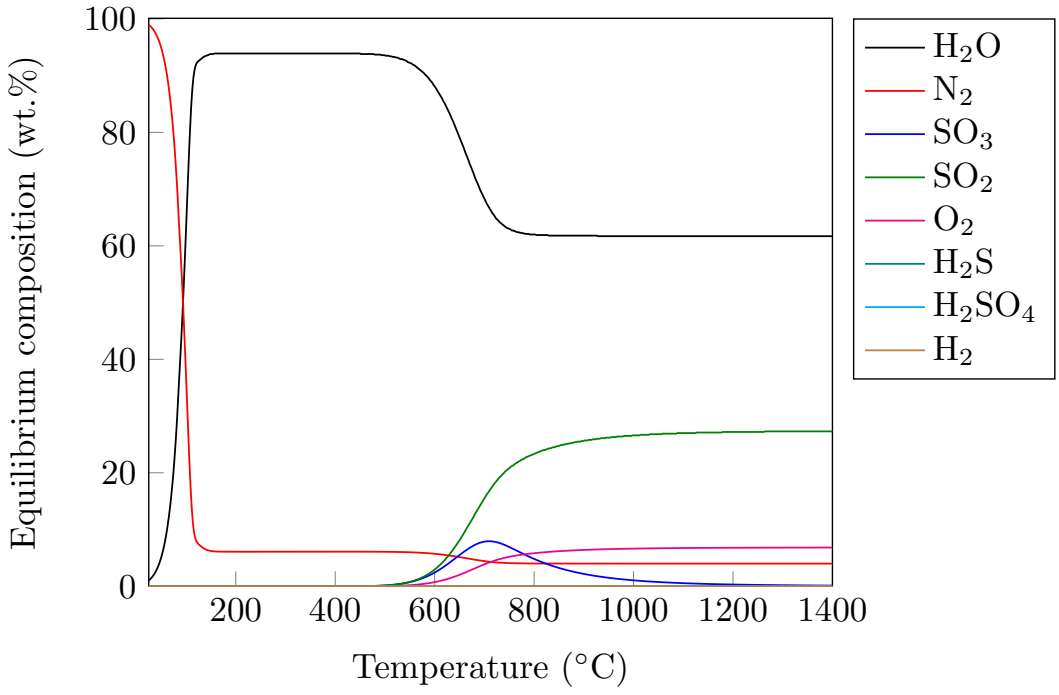

Figure 6.2: Equilibrium composition (wt.%) of the gaseous phases of the thermal decomposition of potassium alum dodecahydrate as a function of the temperature.

6.1.2 Thermogravimetric analysis

The TGA and DTA curves of the thermal decomposition of pure aluminum sulfate, potassium alum, and the mixture of potassium sulfate and aluminum sulfate are displayed in Figures 6.3 and 6.4. In the curve related to $KAl(SO_4)_2$, constant mass is reached at 250 °C due to the dehydration steps, corresponding to a mass loss of 43.82 %. This behavior agrees with the previous thermodynamic analysis (Figure 6.1 - Equations 3-1 and 3-2) and with the literature data.[21,35,38,39]

The desulfation process starts around 700 °C, also in agreement with the present thermodynamic simulations and literature studies.[32,35,41,42,51] This final decomposition step corresponds to a weight loss of 23.91 %, reaching a final fraction of 32.27 % of the initial mass used. Considering that the initial compound used was potassium alum dodecahydrate, this final mass percentage indicate that the solid products of the reaction are K_2SO_4 and Al_2O_3, as seen in Equation 6-4 and 6-5.

The theoretical weight loss for the dehydration and the desulfation steps involved in the thermal decomposition of $KAl(SO_4)_2 \cdot 12$ are shown in Table 6.1. The theoretical weight loss for the complete dehydration is 45.54 %, close to the one shown in TGA (43.82 %). As for the the desulfation stage, the theoretical weight loss is 25.32 %, close to the experimental one (23.91 %).

Table 6.1: Theoretical weight loss (wt.%) in each step of the decomposition of potassium alum dodecahydrate.

Reaction	Theoretical weight loss (wt.%)
Equation 3-1	34.16
Equation 3-2	11.38
Equation 6-4	0.00
Equation 6-5	25.32
Total	70.86

The signal of pure aluminum sulfate shows that the dehydration process ends around 400 °C (Equation 6-7). After that, the anhydrous $Al_2(SO_4)_3$ starts to decompose around 750 °C corresponding to a mass loss of 35.59 % (Equation 6-8/36.04 % - theoretical) related to the formation of Al_2O_3 and SO_3. According to the thermodynamic analysis (Figure 6.1), aluminum sulfate should start to decompose around 600 °C, and the decomposition should be completed at temperatures higher than 700 °C. However, it is well

known that during a TG dynamic analysis, the decomposition temperature is always shifted to higher values as the heating rate is increased. Also, the decompositon of $Al(SO_4)_3$ is affected under the presence of K_2SO_4, contributing to the decomposition temperature's reduction, as pointed out by Apte, Kiran and Chernosky.[26] Thus, the aluminum sulfate that comes from the thermal decomposition of potassium alum tends to decompose in lower temperatures than pure aluminum sulfate.

$$Al_2(SO_4)_3 \cdot 18\,H_2O \xrightarrow{\Delta} Al_2(SO_4)_3 + 18\,H_2O_{(g)} \tag{6-7}$$

$$Al_2(SO_4)_3 \xrightarrow{\Delta} Al_2O_3 + 3\,SO_{3(g)} \tag{6-8}$$

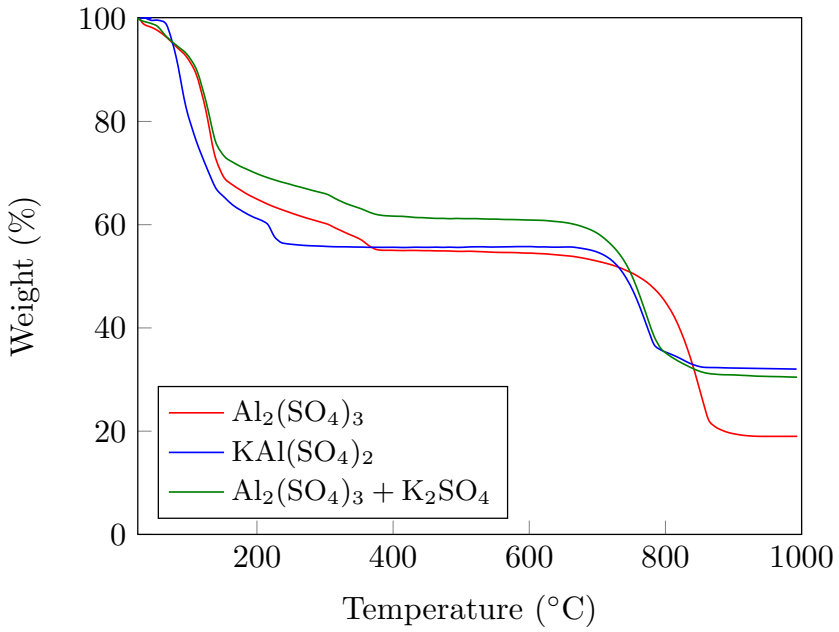

Figure 6.3: TGA curves of the thermal decomposition of pure aluminum sulfate, potassium alum, and mixture of potassium sulfate and aluminum sulfate at heating rate of 10 °C.min^{-1}.

To better investigate the effect of potassium sulfate in the decomposition of aluminum sulfate, a TGA run was performed using a mixture of both sulfates. The dehydration process shows a remarkable resemblance with the one related to pure aluminum sulfate, which is expected as K_2SO_4 does not present water molecules in its structure. On the other hand, the desulfation process shows resemblance with the one related to potassium alum, with a very similar decomposition temperature (around 700 °C).

The similarity between the curves can be better seen in the DTA signals are presented in Figure 6.4. The red and green curves follow almost the same pattern until 500 °C, showing that the dehydration reaction steps of the mixture is analogous to the pure aluminum sulfate (Equation 6-7). At higher

temperatures, the green curve resembles the blue one, showing apparently two peaks in the decomposition, whereas the pure aluminum sulfate signal displays only a single peak. Thus, the decomposition reaction steps of the sulfates mixture should be similar to the one of potassium sulfate. This behavior showcases the effect of the presence of potassium sulfate in the thermal decomposition.

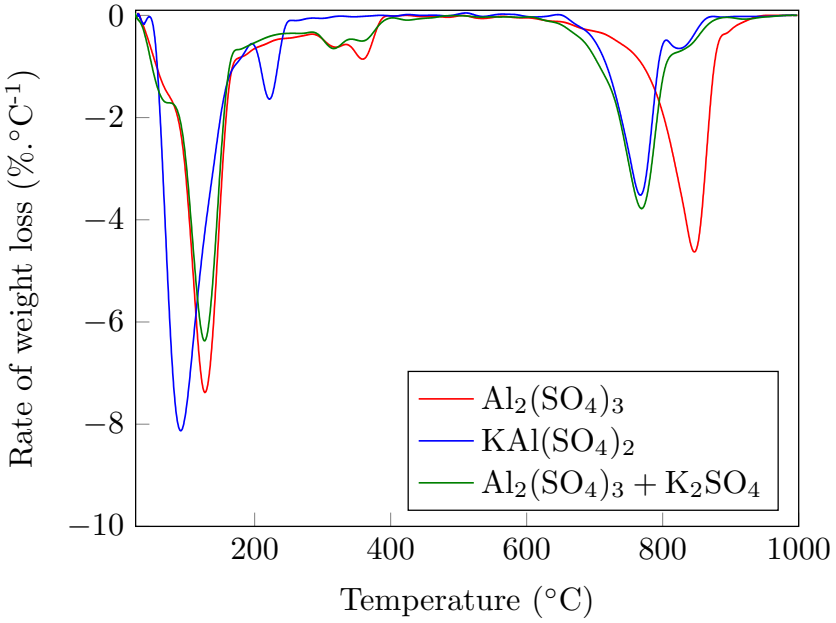

Figure 6.4: DTA curves of the thermal decomposition of pure aluminum sulfate, potassium alum, and mixture of potassium sulfate and aluminum sulfate at heating rate of 10 °C.min^{-1}.

6.1.3 Kinetic modeling

6.1.3.1 Graphical method

As mentioned in the previous sections, the anhydrous potassium alum dissociates into K_2SO_4 and $Al_2(SO_4)_3$, which further decomposes into Al_2O_3 (Equations 6-4 and 6-5). Thus, the application of the graphical method should be suitable in this case.[27] Figures 6.5, 6.6, and 6.7 depict the fitting of model using the graphical method compared to experimental data. In all cases, the determination coefficient is 0.99, corresponding to a good agreement of the model, with most of the experimental data fitted within the confidence region.

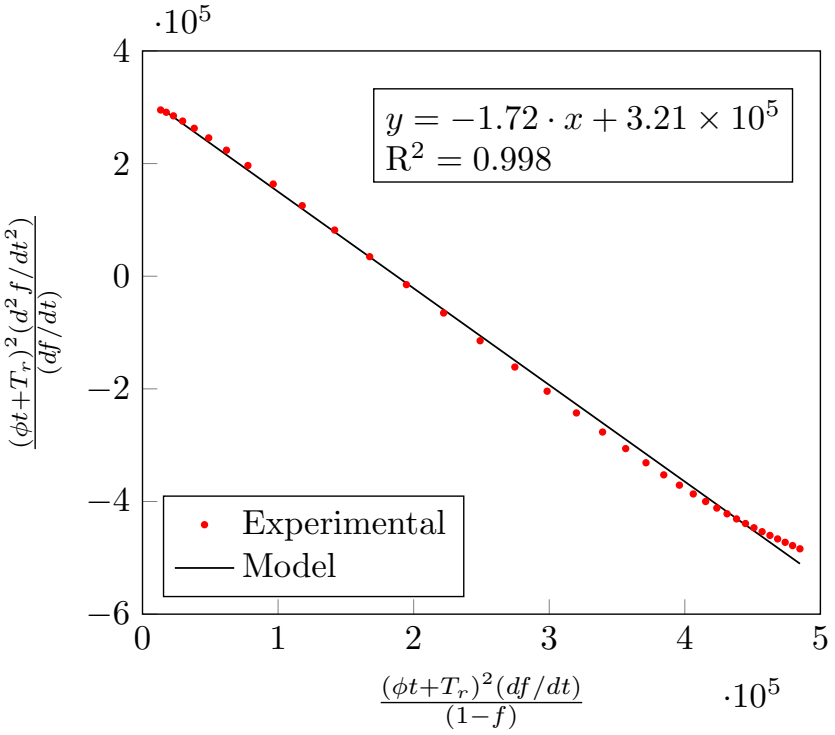

Figure 6.5: Linear plot of the thermal decomposition of pure aluminum sulfate.

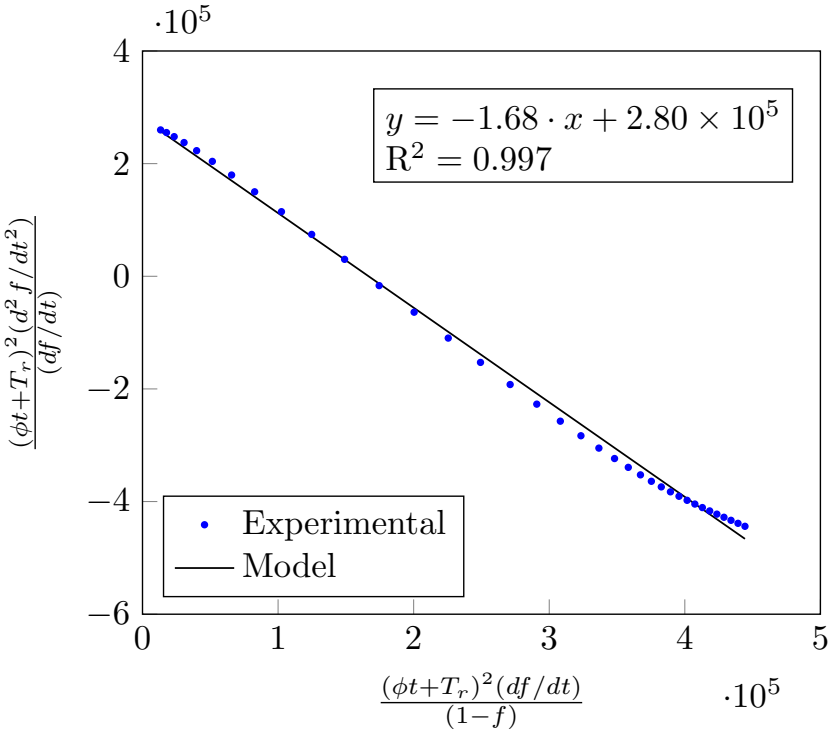

Figure 6.6: Linear plot of the thermal decomposition of potassium alum.

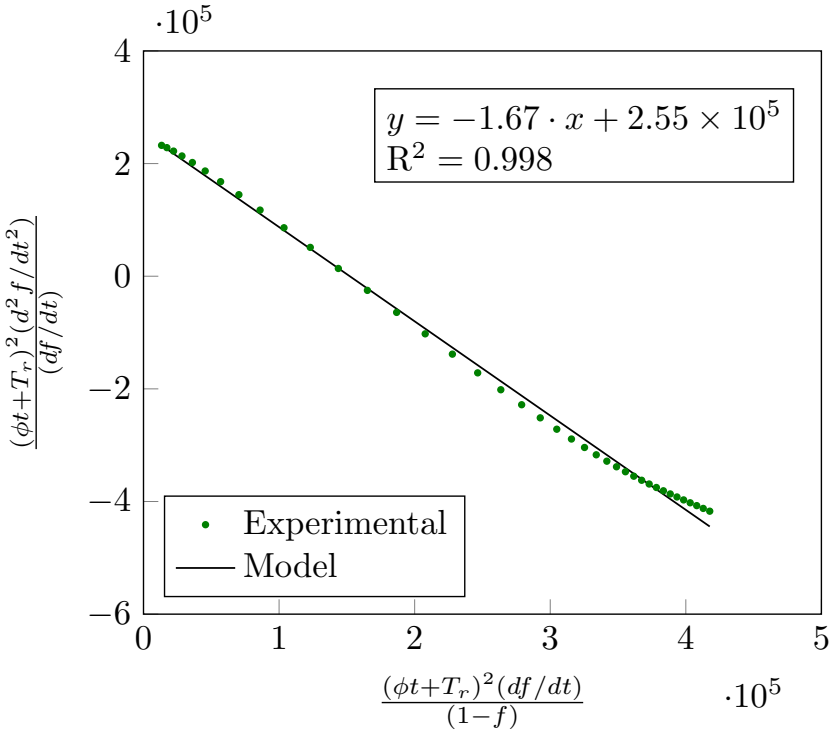

Figure 6.7: Linear plot of the thermal decomposition of the mixture of potassium sulfate and aluminum sulfate.

As mentioned in Section 4.1.1, the kinetic parameters are obtained using the slope and intercept values of the linear plot. Table 6.2 presents the kinetic parameters values as well as the R^2 values for each tested sample. All the reaction orders were similar, around 1.7. Chou and Soong[28] reported the thermal decomposition as first-order reaction, whereas Apte et al.[31] reported as a second-order reaction. Thus, the values obtained with this method are in the same range as observed in the literature. Furthermore, Papazian, Pizzolato and Orrell,[49] and Pelovski et al.[50] stated that different experimental procedures (atmosphere composition) can lead to differences in the reaction order and thermal decomposition rates.

Table 6.2: Kinetic parameters and R^2 values of the thermal decomposition of $Al_2(SO_4)_3$, $KAl(SO_4)_2$, and mixture of $Al_2(SO_4)_3$ and K_2SO_4.

Reactant	n	E_a (kJ.mol^{-1})	R^2
$Al_2(SO_4)_3$	1.72	264.4	0.998
$KAl(SO_4)_2$	1.68	233.1	0.997
$Al_2(SO_4)_3 + K_2SO_4$	1.67	209.3	0.998

On the other hand, the activation energies presented certain discrepancies, with the pure aluminum sulfate with the highest value (264.4 kJ.mol^{-1}),

followed by potassium alum (233.1 kJ.mol^{-1}), and the mixture of potassium and aluminum sulfate with the lowest one (209.3 kJ.mol^{-1}). The difference between the values found for potassium alum and sulfate mixture could be accounted for the different presence of potassium sulfate. In the first case, the K_2SO_4 is formed *in-situ*, and in the second the potassium sulfate is presented at the beginning of the decomposition, making the aluminum sulfate to be always in contact with K_2SO_4. Nevertheless, this results agrees to what is seen in the TG/DTG plots (Figures 6.3 and 6.4). Pure aluminum sulfate presents the highest decomposition temperature, around 750 °C, which explains the highest activation energy compared to the other cases.

Potassium alum and the mixture of sulfates presented lower activation energy values than the one of pure aluminum sulfate. Apte, Kiran and Chernosky[26] reported that the presence of K_2SO_4 should affect the kinetic of the $Al_2(SO_4)_3$ decomposition by lowering the reaction temperature, characterizing a catalytic effect. The present results, as already mentioned earlier, corroborate this hypothesis. However, by analyzing the TG/DTG plots (Figures 6.3 and 6.4), potassium alum and the sulfate mixture, should be associated to E_a values of not much different magnitude, as a similar initial decomposition temperature is observed (233.1 kJ.mol^{-1} and 209.3 kJ.mol^{-1}, respectively).

The fact that in the present case the E_a value for potassium alum decomposition is significantly higher than the one observed for the sulfate mixture could be explained by the residual presence of $KAl(SO_4)_2$ alongside the Al_2O_3 formation, as reported by Souza et al.,[21] which observed a small amount of non-reacted potassium alum for a sample colected at intermediate temperatures, more or less in the middle of the decomposition interval. These non-reacted potassium alum crystals could enhance the thermal resistance for energy transport, making the thermal activation of the $Al_2(SO_4)_3$ crystals more difficult. Another possible explanation was already pointed out earlier, and is based on the fact that the potassium alum thermal decomposition should be associated with a previous decompositions leading to a mixture of $Al_2(SO_4)_3$ and K_2SO_4, thus requiring an extra amount of thermal energy.

6.1.3.2 ODE method

As already mentioned (Section 4.1.2), the ODE system method could be also applied to handle thermal decomposition processes. As the decomposition consists of only one reaction, only a single differential equation is required. The results of the conversion obtained using the ODE method are depicted in Figures 6.8, 6.9, and 6.10. The agreement between experimental and model

values is good in all evaluated cases, even more taking into account the confidence region of 95 %. In the case of potassium alum, a deviation is observed between 800 and 850 °C, which could be accounted by the fact that the decomposition reaction steps is more complex and cannot be completely described by a single differential equation. The DTA signal shows that there is more than one peak, leading to more than one reaction.

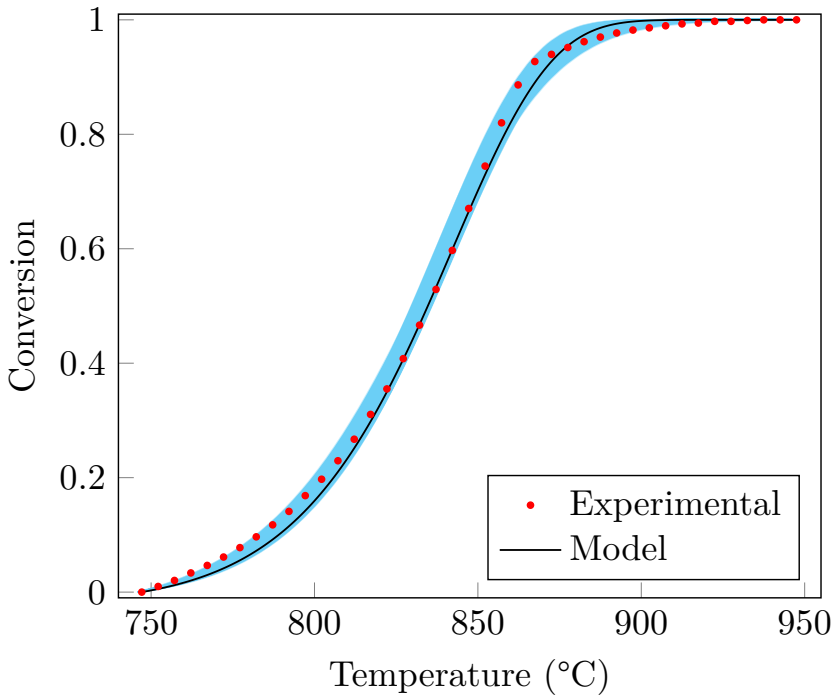

Figure 6.8: Experimental and model conversions of the thermal decomposition of pure aluminum sulfate.

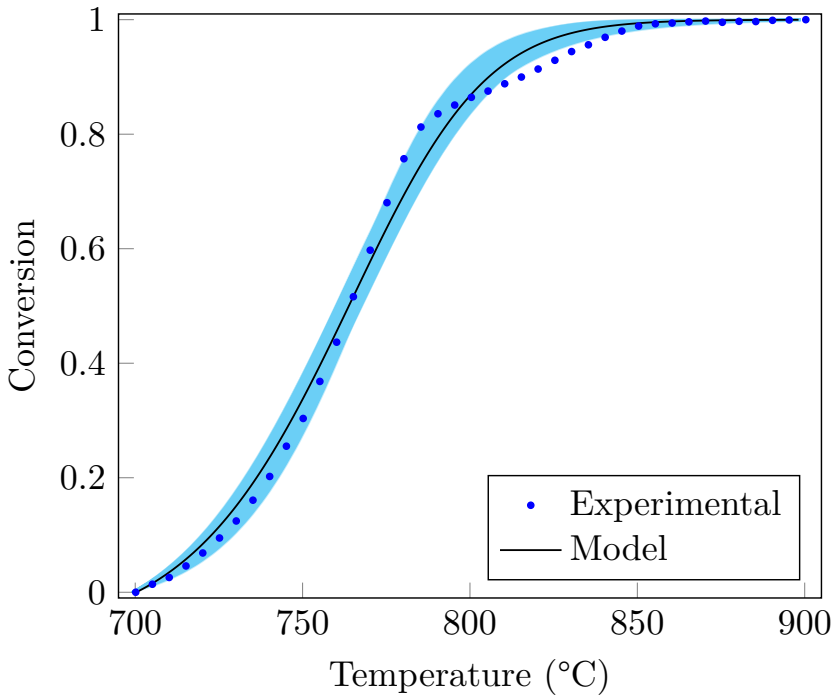

Figure 6.9: Experimental and model conversions of the thermal decomposition of potassium alum.

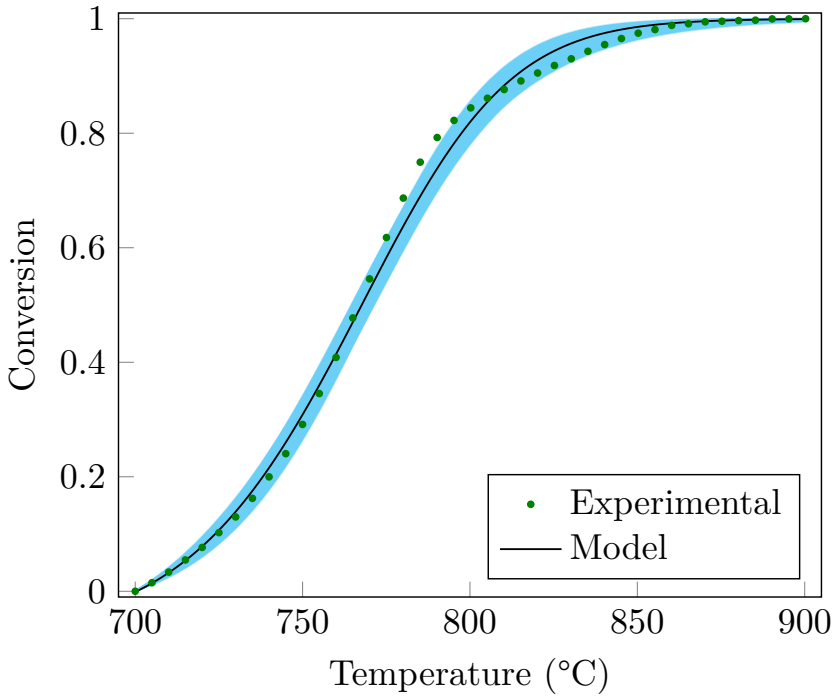

Figure 6.10: Experimental and model conversions of the thermal decomposition of the mixture of potassium sulfate and aluminum sulfate.

The performance of the estimation is depicted in Figure 6.11. In all cases, the error present a rapid decrease in the beginning of the optimization and the following iterations show that the error still show a slight variation due to the

convergence of the particles to the optimum value. The error value behavior can be explained by the sum of the particles' velocities. At first, the particles are scattered throughout the search space looking for their personal best values and the global best. As the optimization progresses, the particles start to converge towards the optimum region, lowering their speeds. In cases a new optimum value is found, there is a slight increase in the sum of the particles' velocities, meaning that the particles started migrating towards a new region. In all cases, 15 experimental data points were used to describe the decomposition and compute the error (Equation 4-11) and estimate the three kinetic parameters. This amount of experimental data was chosen taking into account a time-step of 1.5 min in the TG data, thus the time-step of the integration could be defined accordingly, lowering the simulation's computational cost.

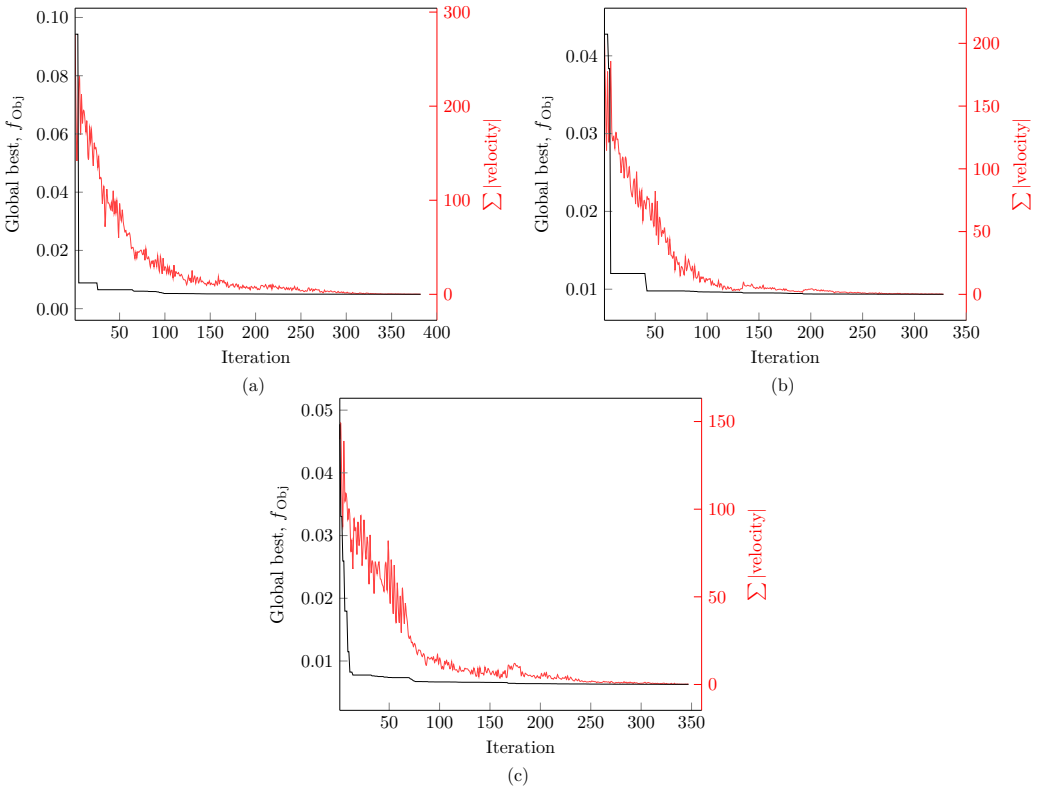

Figure 6.11: Progress of the parameter estimation (error and sum of particle's velocities) in each iteration: (a) pure aluminum sulfate; (b) potassium alum; (c) mixture of potassium and aluminum sulfates.

The estimated kinetic parameters are displayed in Table 6.3. Similar to what was observed in the graphical method, pure aluminum sulfate presents the highest activation energy (352.4 kJ.mol^{-1}), followed by potassium alum (328.3 kJ.mol^{-1}), and the mixture of potassium sulfate and aluminum sulfate with the lowest value (296.3 kJ.mol^{-1}). This trend is also observed in the pre-exponential values.

In comparison with the activation energy values presented by the graphical method, but with good agreement with the experimental data nonetheless. Moreover, these values are still in agreement with the ones reported in the literature.[32,35] These observed discrepancies in the activation energy values could be explained as a direct effect of the numerical method used to estimate the kinetic parameters. This behavior was addressed by Apte et al.[31] that used derivative and integral methods to determine the activation energies of the thermal decomposition of aluminum sulfate and observed that the values were not the same even when the same reaction rate model was used.

Table 6.3: Estimated kinetic parameters and R^2 values of the thermal decomposition of $Al_2(SO_4)_3$, $KAl(SO_4)_2$, and mixture of $Al_2(SO_4)_3$ and K_2SO_4 using PSO.

Reactant	k_0 (min^{-1})	n	E_a ($kJ.mol^{-1}$)	R^2
$Al_2(SO_4)_3$	1.05×10^{16}	1.02	352.4	0.999
$KAl(SO_4)_2$	5.09×10^{15}	1.46	328.3	0.995
$Al_2(SO_4)_3 + K_2SO_4$	1.02×10^{14}	1.44	296.3	0.997

Another noticeable difference between the results achieved through graphical and ODE system methods concerns the estimated reaction order. The reaction order was around 1.7 in all cases using the graphical method, and ranged from 1.0 to 1.5 for the ODE system method. For pure aluminum sulfate, the estimated reaction order was 1.0, which agrees to what is seen in the literature despite using different modeling techniques.[28,31,52]

Moreover, the reaction order of potassium alum, and the mixture of potassium sulfate and aluminum sulfate was 1.46 and 1.44, respectively. The similarity between these values corroborates the similar reaction steps, with the presence of K_2SO_4 acting as catalyst in the decomposition of aluminum sulfate. Perhaps the reaction steps can explain the nature of each reaction order. In the case of pure aluminum sulfate, the thermal decomposition is straightforward, with anhydrous $Al_2(SO_4)_3$ decomposing into aluminum oxide (Equation 6-8). Thus, the reaction order presents an elementary nature. On the other hand, potassium alum and the mixture of sulfates has a much more complex mechanism involving intermediate phases as seen in the thermodynamic assessment (6.1.1). therefore, the reaction order does not show an elementary tendency, and the values are close to each other due to the similarity of the decomposition reaction steps.

The discrepancies can be accounted by experimental factors, such as

mass and heat transfers effects which are not directly addressed by the model. Moreover, another reason why there are differences between the values of both models employed is the fact that in the case of the differential equation method using PSO, the k_0 is also taken into account. The arithmetic used in the graphical method to create a linear plot makes the k_0 to not be considered (Equation 4-5). Moreover, as seen in the works of Rego et al.[27] and Kurban et al.,[61] in the graphical method, the experimental data is first processed to fit in an analytical curve (sigmoid function) to reduce the error in the calculation of the first and second derivatives. Therefore, even considering the same base differential equation (Equation 4-1), the pointed differences can indeed lead to significant deviations in relation to the kinetic parameters obtained with both strategies tested.[31]

6.2 Zinc sulfate

6.2.1 Thermodynamic assessments

The solid and gaseous phases considered in the thermodynamic simulations of the thermal decomposition of zinc sulfate are as follows:

- Solid phases: $ZnSO_4 \cdot 7\,H_2O$, $ZnSO_4 \cdot 6\,H_2O$, $ZnSO_4 \cdot 2\,H_2O$, $ZnSO_4 \cdot H_2O$, $ZnSO_4$, $ZnO \cdot 2\,ZnSO_4$, ZnO, Zn.
- Gaseous species: N_2, H_2O, SO_3, SO_2, O_2, H_2SO_4, H_2S, Zn.

The equilibrium composition of the solid phases as function of the temperature of the thermal decomposition of 1.0 mole of zinc sulfate heptahydrate is depicted in Figure 6.12. The first stages of the decomposition are defined by dehydration reactions, with the presence of zinc sulfate at different hydration levels (hepta-, hexa-, di-, and monohydrates). The dehydration follows the reaction steps shown in Section 3.2 (Equations 3-10, 3-11, and 3-12), with the exception of the dihydrate phase, which is not observed in the literature.[24,34,55] Among all the different hydrate salts, the monohydrate phase is the most stable one, with anhydrous zinc sulfate beginning to be formed at around 150 °C.

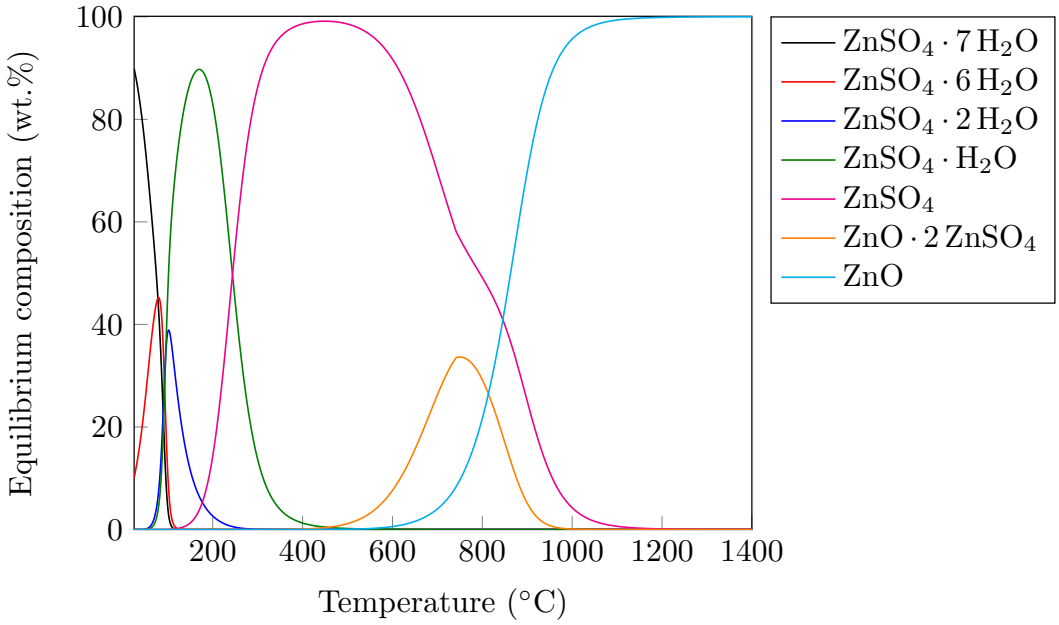

Figure 6.12: Equilibrium composition (wt.%) of the solid phases of the thermal decomposition of zinc sulfate heptahydrate as a function of the temperature.

At 200 °C, the $ZnSO_4 \cdot H_2O$ begins to decompose forming the anhydrous zinc sulfate, reaching 100 % of composition between 400 and 450 °C. The $ZnSO_4$ phase begins to decompose around 500 °C yielding an intermediate phase between zinc sulfate and zinc oxide (Equations 3-13 and 3-14), zinc oxysulfate ($ZnO \cdot 2\,ZnSO_4$).[24,25,57,60] The intermediate phase reaches its peak around 750 °C, which decomposes forming zinc oxide. Complete conversion to ZnO is reached around 1100 °C. The formation of metallic zinc from zinc oxide was not observed in the temperature range studied.

Figure 6.13 displays the equilibrium composition of the gas phases of the thermal decomposition of zinc sulfate heptahydrate. At first, the atmosphere is composed majorly by N_2. As the temperature increases and the dehydration process begins to take place, water starts to be predominant in the composition around 150 °C. As the desulfation process starts around 500 °C (decomposition of anhydrous zinc sulfate), the SO_3, SO_2, and O_2 phases begin to be observed in the equilibrium composition. At the end of the temperature range, only H_2O, SO_2, N_2, and O_2 are present. The other gas phases considered (H_2SO_4, H_2S, and Zn) did not show any considerable amount in the temperature range.

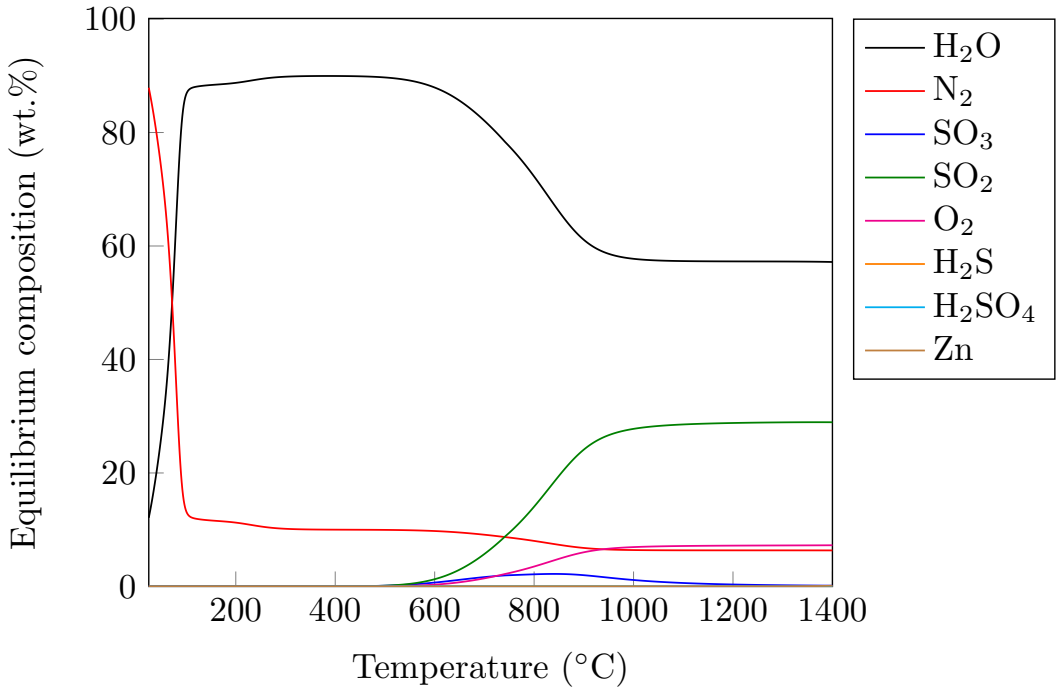

Figure 6.13: Equilibrium composition (wt.%) of the gas phases of the thermal decomposition of zinc sulfate heptahydrate as a function of the temperature.

Another analysis made was the influence of the partial pressure of SO_3 at a fixed temperature depicted in Figure 6.14.This analysis allows to understand the behavior of the transition between zinc sulfate and zinc oxide by observing the shift of Equations 3-13 and 3-14. In this case, the chosen temperature value was 650 °C, in which the desulfation process of $ZnSO_4$ has already begun and there are considerable amounts of zinc sulfate, zinc oxysulfate, and zinc oxide. At lower pressure values, ZnO is majorly observed due to SO_3 being a product of the thermal decomposition, as seen in Figure 6.13. Because of the equilibrium, the absence of SO_3 shifts the reaction towards the formation of the oxide phase. Additionally, the other phases ($ZnSO_4$ and $ZnO \cdot 2\,ZnSO_4$) are observed as the partial pressure increases. In this cases, as high quantities of SO_3 are present, the equilibrium shifts towards the reactants.

$$ZnSO_4 \xrightarrow{\Delta} \tfrac{1}{3}\,ZnO \cdot 2\,ZnSO_4 + \tfrac{1}{3}\,SO_{3(g)} \tag{3-13}$$

$$\tfrac{1}{3}\,ZnO \cdot 2\,ZnSO_4 \xrightarrow{\Delta} ZnO + \tfrac{2}{3}\,SO_{3(g)} \tag{3-14}$$

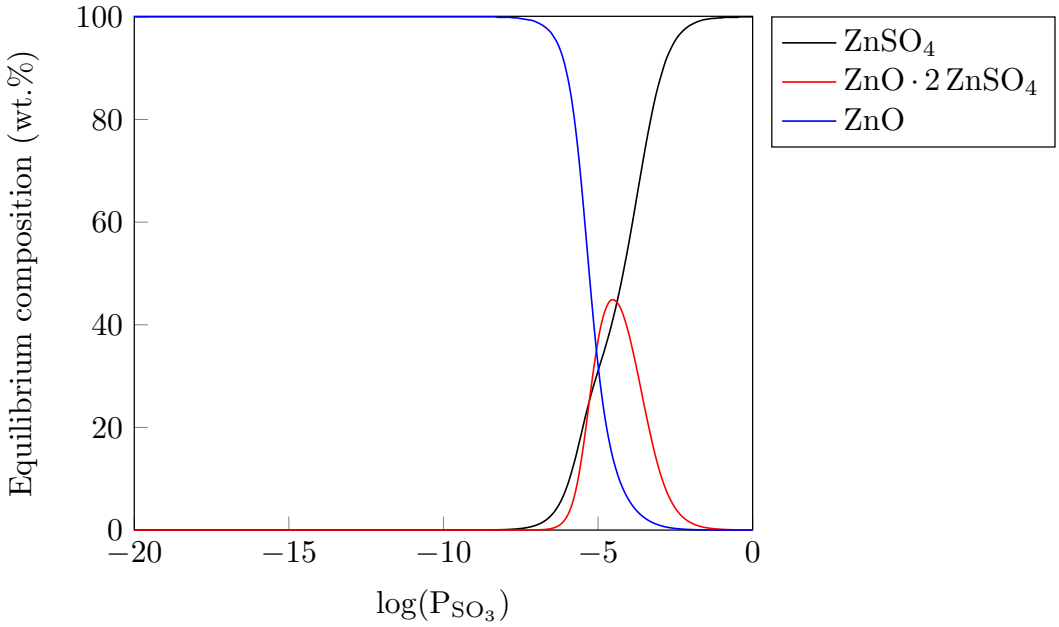

Figure 6.14: Equilibrium composition (wt.%) of the solid phases of the thermal decomposition of zinc sulfate heptahydrate as a function of the partial pressure of SO_3.

To better understand the influence of both variables (temperature and partial pressure of SO_3), the equilibrium composition surface of $ZnSO_4$, $ZnO \cdot 2\,ZnSO_4$, and ZnO was depicted in Figures 6.15, 6.16, and 6.17, respectively. At temperatures lower than 100 °C, only zinc sulfate is observed. For cases involving low partial pressure of SO_3, the temperature required to decompose zinc sulfate into zinc oxysulfate and zinc oxide reduces drastically when compared to equilibrium conditions of P_{SO_3} close to one atm (Figures 6.15 and 6.17). This behavior happens due to the shift in the equilibrium of the endothermic reaction, which means that for higher temperatures, more SO_3 is expected to be formed. Moreover, the intermediate phase (Figure 6.16) is present in all the evaluated conditions, which indicates that there is no direct path to obtain zinc oxide from zinc sulfate. Moreover, the maximum composition of $ZnO \cdot 2\,ZnSO_4$ is 76.59 %. Thus, there is no case in which the intermediate phase fully composes the system, enabling to describe the oxysulfate as an intermediate phase between the anhydrous zinc sulfate and zinc oxide.

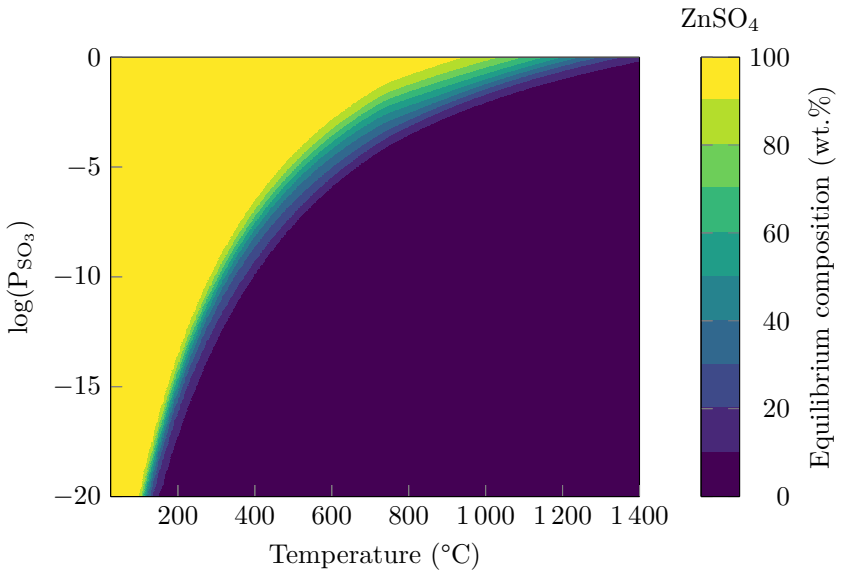

Figure 6.15: Equilibrium composition (wt.%) surface of $ZnSO_4$ as function of the temperature and partial pressure of SO_3.

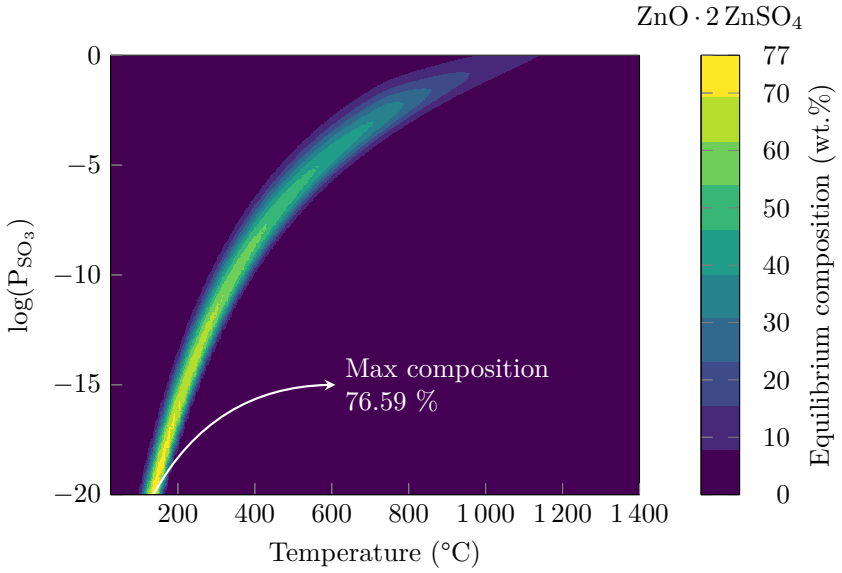

Figure 6.16: Equilibrium composition (wt.%) surface of $ZnO \cdot 2\,ZnSO_4$ as function of the temperature and partial pressure of SO_3.

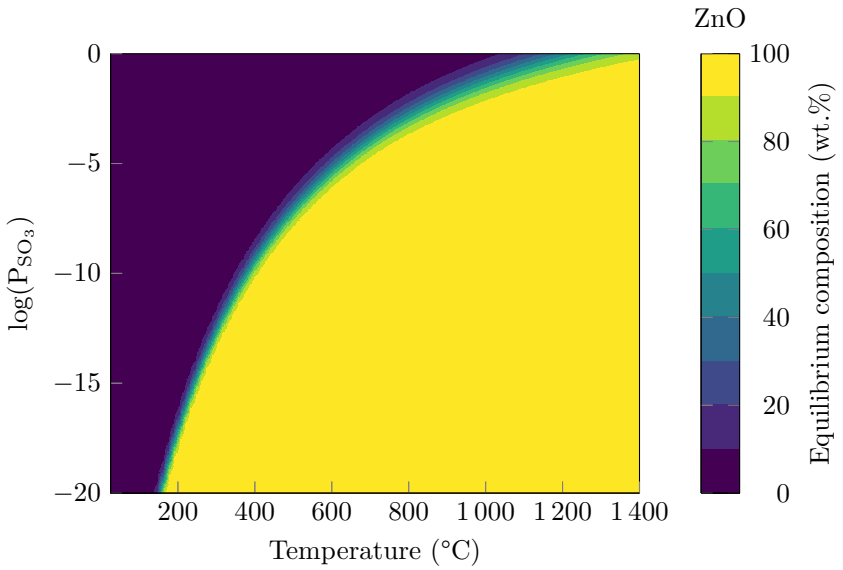

Figure 6.17: Equilibrium composition (wt.%) surface of ZnO as function of the temperature and partial pressure of SO_3.

6.2.2 Thermogravimetric analysis

The TGA and DTG curves obtained for zinc sulfate heptahydrate thermal decomposition are shown in Figure 6.18. By analyzing both curves, it may be noticed that the dehydration process takes place in three different stages, as already reported in the literature.[24,34] The first stage occurs at the beginning of the experiment, reaching its DTG peak around 70 °C. As the temperature increases, the weight is lost continuously until it reaches a plateau correspondent to the monohydrate salt ($ZnSO_4 \cdot H_2O$). The final dehydration stage occurs around 200 °C, yielding anhydrous zinc sulfate. The behavior of the TGA in Figure 6.18 is very similar to the one reported by Mu and Perlmutter,[24] whom claimed that their initial material consisted of $ZnSO_4 \cdot 5.4\,H_2O$, a mixture of zinc sulfate at different hydration degrees. This effect occurs due to the instability of zinc sulfate heptahydrate at room temperature.[24]

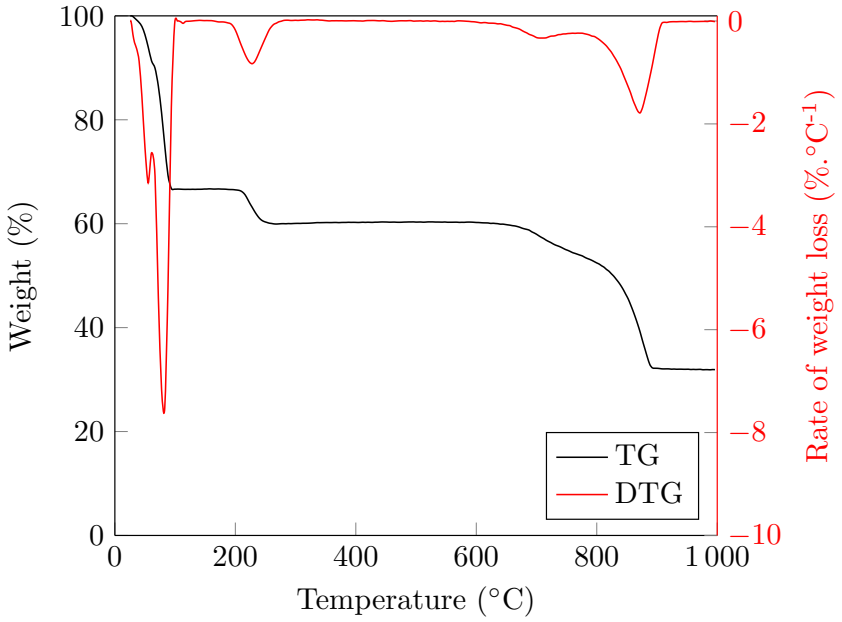

Figure 6.18: Thermogravimetric analysis of the thermal decomposition of $ZnSO_4 \cdot 7\,H_2O$ in inert atmosphere.

After full dehydration, the anhydrous zinc sulfate shows stability from 250 to 600 °C. At higher temperatures, the sulfate decomposes into what appears to be two sequential reactions (Equations 3-13 and 3-14), resulting in a total weight loss of around 30 %.[24,25,29,34,57] A similar analysis can be made when using the DTG curve, detecting two peaks. However, taking a closer look at the DTG curve, it is notable that the two peaks are not completely separated, which can be an indication that at some point the two reactions are not sequential, but occur simultaneously. Around 800 °C, the already formed $ZnO \cdot 2\,ZnSO_4$ can decompose into zinc oxide as $ZnSO_4$ is decomposing into new zinc oxysulfate. This behavior is somewhat seen in Figure 6.12, as the ZnO equilibrium composition starts to grow right after the zinc oxylsufate is present in the system.

Table 6.4 displays the theoretical and experimental weight losses in every dehydration and decomposition steps. It is notable that the first dehydration step shows great difference between the theoretical and experimental values. This could be accounted by the fact that the theoretical weight loss is calculated considering 1.0 mol of pure zinc sulfate heptahydrate. However, as seen in the experimental, the starting material used in TG runs seems to be a mixture of sulfates with different hydration degrees, similar to the work of Mu and Perlmutter.[24] The weight loss of the following reactions show agreement between theory and the experiments.

Table 6.4: Theoretical and experimental weight losses (wt.%) in each step of the decomposition of zinc sulfate heptahydrate.

Reaction	Weight loss (wt.%)	
	Theoretical	Experimental
Equation 3-10	6.26	3.58
Equation 3-11	31.32	29.83
Equation 3-12	6.26	6.53
Equation 3-13	9.29	8.73
Equation 3-14	18.59	19.31
Total	71.72	67.98

6.2.3 Kinetic modeling

The thermogravimetric analysis (Figure 6.18) suggests that the segmentation of the desulfation signal into two distinct contributions can be quite troublesome, which takes its toll in applying the graphical method.[36,61,86] Therefore, it is desirable to use the ODE method coupled with the PSO algorithm to simultaneously estimate the kinetic parameters of both decomposition reactions (Equations 3-13 and 3-14). The case of zinc sulfate is similar to the one seen with copper sulfate (Figure 4.2). In both cases, the decomposition of the anhydrous sulfate occurs in two steps, with the presence of an intermediate phase (oxysulfate). Thus, using the same approach should yield a similar result. The difference lies in the weights used to calculate the global conversion (Equation 4-10).

Considering 1.0 mole of anhydrous zinc sulfate, the conversion weights (w_i) can be determined by a simple mass balance of the theoretical reaction step. Using the data in Table 6.5, the conversion weights, w_1 and w_2, are roughly $\frac{1}{3}$ $\left(\approx \frac{16.53}{49.59}\right)$ and $\frac{2}{3}$ $\left(\approx \frac{33.06}{49.59}\right)$ for the decomposition of $ZnSO_4$ and $ZnO \cdot 2\,ZnSO_4$, respectively.

Table 6.5: Theoretical weight loss (wt.%) in each step of the decomposition of anhydrous zinc sulfate.

Reaction	Theoretical weight loss (wt.%)	w_i
Equation 3-13	16.53	0.333
Equation 3-14	33.06	0.667
Total	49.59	1.0

Figure 6.19 shows the result of the ODE method with PSO. The agreement between the model and the experimental values are excellent (R^2 = 0.9996). Considering the confidence region, all the experimental data fit within the model range.

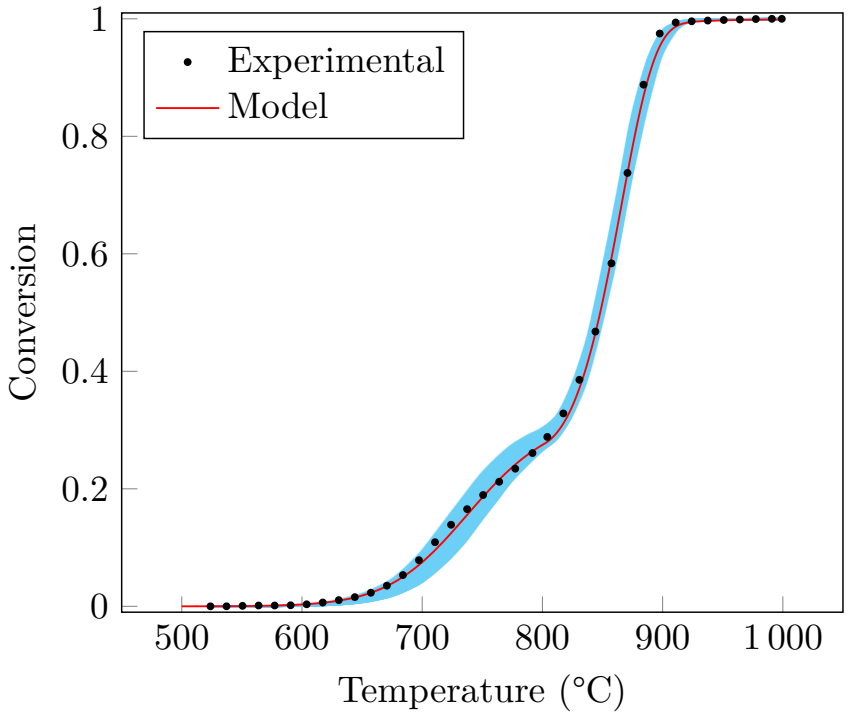

Figure 6.19: Experimental and model conversion of the thermal decomposition of zinc sulfate.

As mentioned in Section 4.1.2, one advantage of using a system of ODE to describe the decomposition is that the reactions can be observed individually. The individual decomposition of $ZnSO_4$ and $ZnO \cdot 2\,ZnSO_4$ are depicted in Figure 6.20. Around 600 °C, only the decomposition of anhydrous zinc sulfate into zinc oxysulfate takes place. The following reaction (decomposition of $ZnO \cdot 2\,ZnSO_4$ into ZnO) begins close to 770 °C. These results are in agreement to the thermodynamic presented previously, where the intermediate phase (zinc oxysulfate) is present in the temperature range of 600 and 1000 °C. Furthermore, the modeling results are in agreement to what is suggested in TGA data (Figure 6.18), indicating that the peaks are not completely separated from one another. This behavior may indicate that the reactions can occur simultaneously throughout the decomposition process.

The kinetic parameters estimated using PSO are shown in Table 6.6. The activation energy related to the decomposition of $ZnO \cdot 2\,ZnSO_4$ is higher than the one concerning the decomposition of $ZnSO_4$. This behavior is expected as the zinc oxysulfate decomposes at higher temperatures than zinc sulfate. The

estimated activation energy of the decomposition of $ZnSO_4$ was 272 kJ.mol^{-1}, which is in the range reported in the literature in dynamic studies in inert atmosphere. Kurban et al.[61] reported an activation energy of 238 kJ.mol^{-1}, and Mu and Perlmutter[24] reported 353 kJ.mol^{-1}.

The estimated activation energy value of the decomposition of $ZnO \cdot 2\,ZnSO_4$ was 367 kJ.mol^{-1}. There are not plenty of works concerning the decomposition of zinc oxysulfate. Ingraham and Marier[29] reported an activation energy of 242 kJ.mol^{-1}, Kurban et al.[61] reported an activation energy of 368 kJ.mol^{-1}. The value of the present work is very close to the one reported by Kurban et al..[61] Moreover, it follows the same tendency of the works of Narayan, Tabatabaie-Raissi and Antal,[25] and Kurban et al.,[61] which showed that the activation energy of zinc oxysulfate was higher than the one of zinc sulfate.

Table 6.6: Estimated kinetic parameters for the decomposition of $ZnSO_4$ and $ZnO \cdot 2\,ZnSO_4$ obtained using PSO.

Reaction	k_0 (min^{-1})	E_a (kJ.mol^{-1})	n
Equation 3-13	2.52×10^{12}	272	2.0
Equation 3-14	1.25×10^{16}	367	1.0

The reaction orders also presented differences. The decomposition of zinc sulfate appears as a second-order reaction, and the decomposition of zinc oxysulfate is a first-order reaction. The difference in the reaction orders was addressed in the work of Narayan, Tabatabaie-Raissi and Antal,[25] which reported a the decomposition of $ZnSO_4$ as a first-order reaction, whereas the decomposition of of $ZnO \cdot 2\,ZnSO_4$ is a pseudo-zero order reaction.

All these differences between the model and the literature data can be accounted in different causes. First, the experimental set/procedure significantly impacts the final results of the decomposition modeling. Narayan, Tabatabaie-Raissi and Antal[25] stated that the increase in the mass sample in the thermal studies shifted the temperature in which the decomposition started. In other context, Ingraham and Marier,[29] and Tagawa and Saijo[59] used zinc sulfate pellets instead of powdered samples. These differences in the sample preparation impact the thermogravimetric balance reading due to heat and mass transfer effects, which are deeply affected by geometry and sample sizes.

The atmosphere composition is also an important process variable in the thermal studies.[25,58] In the work of Narayan, Tabatabaie-Raissi and Antal,[25] the change in the atmosphere composition (inert and air) represented a difference in 50 kJ.mol^{-1} in the activation energy of the $ZnSO_4$ decomposition,

with air atmosphere showing a higher value than the inert atmosphere. This behavior is accounted by the shift in the equilibrium reaction. The decomposition of $ZnSO_4$ into $ZnO \cdot 2\,ZnSO_4$ and ZnO (Equations 3-13 and 3-14) releases gas products (SO_3, SO_2, and O_2). Thus, as the air atmosphere adds O_2, the equilibrium is shifted towards the formation of the reactants, which ends up making the decompositions of $ZnSO_4$ and $ZnO \cdot 2\,ZnSO_4$ more difficult to be completed and consequently having higher activation energy values.

Besides the experimental conditions, the modeling techniques used also cause changes in the numerical results. Isothermal runs are usually used to create Arrhenius' plots as shown in the works of Ducarroir et al.,[57] Tagawa and Saijo,[59] and Kolta and Askar.[84] Despite using the same modeling technique, all these authors reported different kinetic results, which might be explained by the difference in the experimental conditions used by each one of them.

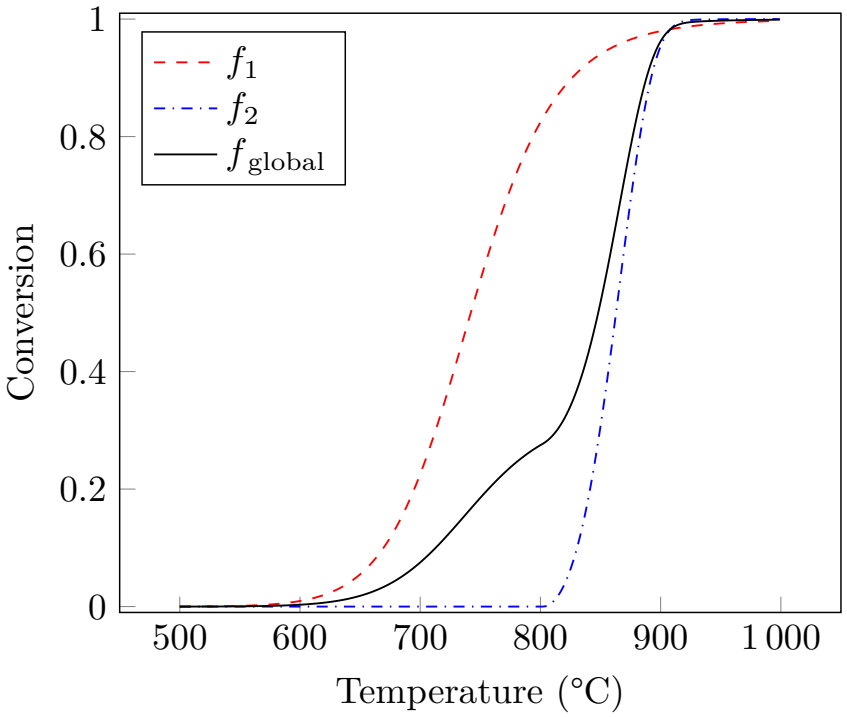

Figure 6.20: Individual and global conversions of the reactions involved in the thermal decomposition system of zinc sulfate.

The conversions curves presented in Figures 6.19 and 6.20 show how well the ODE method can be used alongside the PSO algorithm to describe more complex systems. Considering that the decomposition process can be breakdown into single reactions, the ODE method can be used to describe the whole thermal decomposition (including dehydration), by simply adding more differential equations and properly coupling them with the right weight

coefficients (Equation 4-10). This is a major advantage over the graphical method, which needs the conversions curves to be well-segmented in order to precisely work.

In respect to PSO, the consequence of adding more equations is that the amount of kinetic parameters required to estimate also increases. Taking into account that three kinetic parameters (pre-exponential factor, activation energy, and reaction order) are estimated for each chemical reaction considered, the computational effort and complexity should naturally increase. One way to reduce the computational effort is segment the process into different sub-processes. However, by performing this segmentation, it cannot be assured that the global minimum is going to be reached.

As an example, the complete modeling of the thermal decomposition of $ZnSO_4 \cdot 7\,H_2O$ would involve five equations (three concerning dehydration and two concerning desulfation), which leads to 15 estimated kinetic parameters. The whole estimation could be divided into two sub-sets of equations. The first three would describe the dehydration, and the other two concern the desulfation. Therefore, the decomposition would be completely modeled and the computational complexity reduced. In the end, with the solution of the sub-sets, the whole system can be simulated using the known kinetic parameters and new conversion weights that describe the system as only one set.

The performance of the parameter estimation for the thermal decomposition of zinc sulfate is depicted in Figure 6.21. The behavior is similar to the one related to the decomposition of the aluminum-bearing compounds (Figure 6.11), with a rapid decrease of the error value at the beginning of the estimation and further small decreases, which can be seen as a fine-tuning of the parameters. However, there is a notable difference in the error value. In previous cases, the reactions were simpler to model as there is only one decomposition involved, and thus only one differential equation.

Considering that simplicity, there was no need to use a huge set of experimental data points to well-describe the decomposition. In the case of zinc sulfate, there is a more complex behavior with the presence of an intermediate phase and simultaneous reactions occurring (Figure 6.20). Thus, there is a need to used more experimental data to properly describe the decomposition. The amount of experimental data points used to describe the process and compute the error (Equation 4-11) was 37 using the same methodology as seen in Section 6.1.3.2 to estimate the six kinetic parameters (three for each ODE).

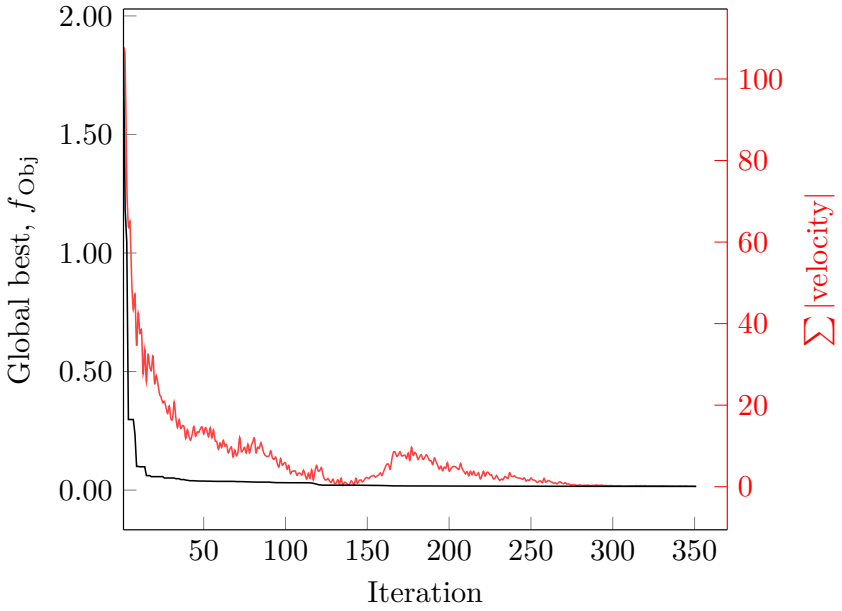

Figure 6.21: Progress of the parameter estimation (error and sum of particle's velocities) in each iteration for the decomposition of zinc sulfate.

6.3 Iron sulfate

6.3.1 Thermodynamic assessments

The solid and gaseous phases considered in the thermodynamic simulations of the thermal decomposition of iron (II) sulfate are as follows:

- Solid phases: $FeSO_4 \cdot 7\,H_2O$, $FeSO_4 \cdot 4\,H_2O$, $FeSO_4 \cdot H_2O$, $Fe_2(SO_4)_3$, $FeOHSO_4$, $FeSO_4$, $Fe_2(SO_4)_3 \cdot 9\,H_2O$, $Fe_2(SO_4)_3 \cdot 7\,H_2O$, $Fe_2(SO_4)_3(H_2O)_{5.03}$, Fe_2O_3, Fe_3O_4, FeO, Fe.
- Gaseous species: H_2O, O_2, SO_2, SO_3, N_2.

The equilibrium composition regarding the presence of the solid phases generated during thermal decomposition of 1.0 mole of iron (II) sulfate heptahydrate as function of the temperature is shown in Figure 6.22. Similar to the other studied cases, the first stages comprehend the dehydration of the salt. By the hydrated phases present in the thermodynamic analysis (hepta-, tetra-, and mono-), the dehydration reaction steps follow the one proposed in the literature[62–64] (Section 3.3 - Equations 3-15, 3-16, and 3-17). Around 150 °C, the monohydrate phase begins to decompose yielding the anhydrous iron (II) sulfate.

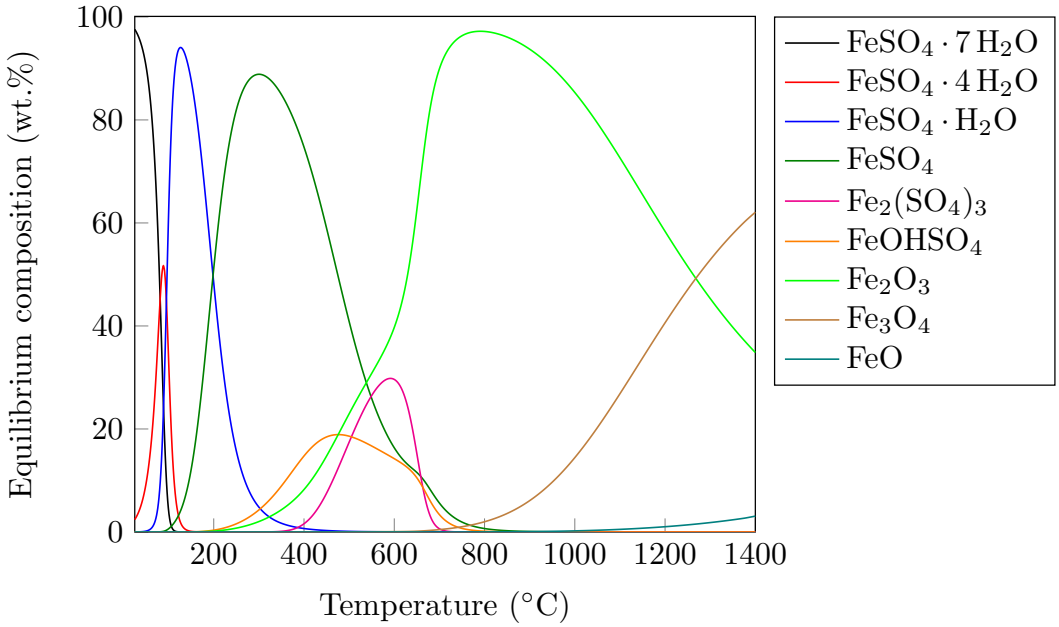

Figure 6.22: Equilibrium composition (wt.%) of the solid phases of the thermal decomposition of iron sulfate heptahydrate as a function of the temperature.

The desulfation of $FeSO_4$ is complex, with the presence of various intermediate phase between the sulfate and the oxide phases. Around 200 °C, it is noted the presence of hematite alongside the iron hydroxide sulfate ($FeOHSO_4$). The latter was observed in the experimental studies using XRD analysis.[60,74] At higher temperatures, around 350 °C, the $FeOHSO_4$ curve reaches its peaks, and the anhydrous iron (III) sulfate begins to be formed, showing similarity with the reaction steps proposed by Equations 3-21, 3-22, and 3-23. After 600 °C, the sulfated phases ($FeSO_4$, $FeOHSO_4$, and $Fe_2(SO_4)_3$)[74] begin to decompose and the oxide phases begin to comprise the majority of the system's equilibrium composition. At very high temperatures, above 95- °C, it is seen that hematite decomposes into magnetite, which then decomposes into FeO. The formation of metallic iron was not observed in the studied temperature range.

The thermodynamic results displayed in Figure 6.22 show how difficult is to set a definitive reaction steps over the decomposition of iron (II) sulfate. In the temperature range between 400 and 750 °C, 5 different solid phases are present, which may indicate that the decomposition steps are not sequential, but simultaneous. This behavior represents a challenge in the kinetic modeling as seen in the case of the thermal decomposition of zinc.

The equilibrium compositions concerning the gaseous phases on the thermal decomposition of 1.0 mole of iron (II) sulfate heptahydrate as function of the temperature are depicted in Figure 6.23. At first, the atmosphere is majorly composed by N_2 and, as the temperature is increased and the

dehydration of the salt begin to take place, H_2O begins to be the dominant gaseous species around 200 °C. Similar to what is seen in the solid phase equilibrium diagram, the equilibrium composition of the gas phase also shows some complexity. At 200 °C, the presence of SO_2 is observed as the desulfation process starts. Around 600 °C, as the curve seems to be entering into an equilibrium, another increase is observed, corresponding to the decomposition of $Fe_2(SO_4)_3$ into the oxide phases. After 900 °C, the equilibrium state does not change appreciably with temperature, Only a slight variation in O_2 concentration can be observed, a consequence from formation of FeO through Fe_2O_3 reduction.

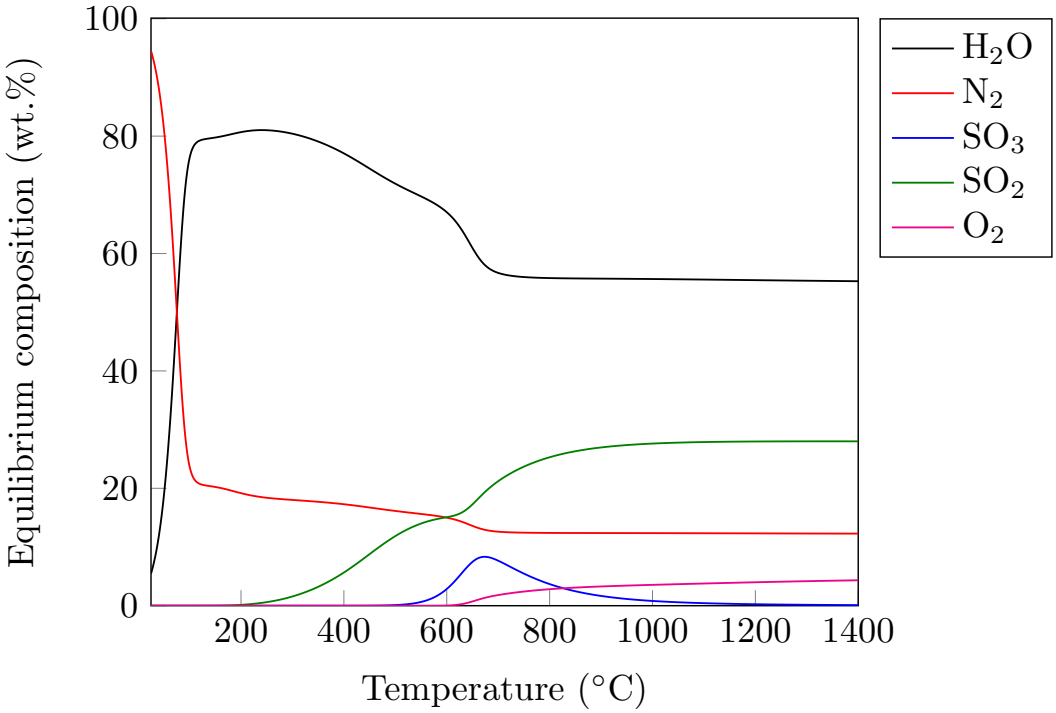

Figure 6.23: Equilibrium composition (wt.%) of the gas phases of the thermal decomposition of iron sulfate heptahydrate as a function of the temperature.

6.3.2 Thermogravimetric analysis

Figure 6.24 displays the TGA and DTA curves of the thermal decomposition of iron (II) sulfate heptahydrate. It is noted that the dehydration occurs in two different stages, which partially disagrees to what is seen in the literature. Wang, Debelak and Roth[62] used TGA and differential scanning calorimetry in their work, reporting three different dehydration stages. Lacalamita et al.[74] also reported three dehydration stages using TGA and XRD.

One possible explanation to this difference might be the equipment's sensitivity, as the first and second dehydration stages occurs at low temperatures,

which makes it hard to well-segment the reactions. Considering that the TGA curve in Figure 6.24 was made with a heating rate of 10 °C.min^{-1}, perhaps the dehydration could be better analyzed using lower heating rates, as seen in the work of Wang, Debelak and Roth.[62] Nevertheless, the first weight drop begins at room temperature, with a peak around 100 °C, ending around 150 °C.

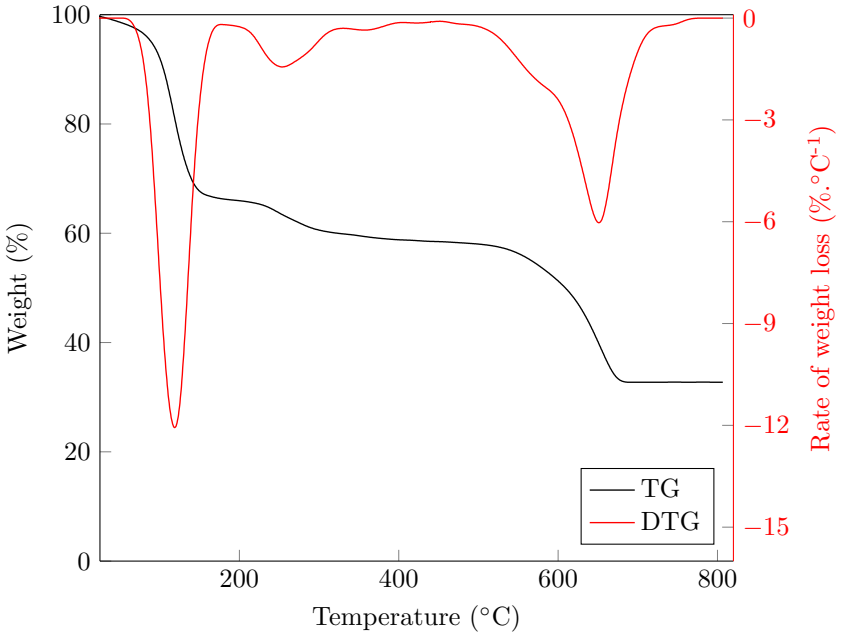

Figure 6.24: Thermogravimetric analysis of the thermal decomposition of $FeSO_4 \cdot 7\,H_2O$ in inert atmosphere.

This first weight drop correspond to around 33.6 % of weight loss, indicating that the initial material was not completely composed by iron (II) sulfate heptahydrate, but a mixture of the heptahydrate and the tetrahydrate salts, yielding the iron (II) sulfate at an intermediate hydration degree. This behavior was observed by Mu and Perlmutter[24] when working with zinc sulfate heptahydrate, regarding its higroscopicity, which is unstable at room temperature. The XRD results of Lacalamita et al.[74] show that their initial material is composed of 80 % of $FeSO_4 \cdot 7\,H_2O$ and 20 % of $FeSO_4 \cdot 4\,H_2O$. Considering the weight loss of 33.6 %, it can be assumed that the initial materials has a non-stoichiometric composition, with hydration water molecules between 4 and 7.By performing a mass balance with the TGA data, the initial material used in the present work is composed of 60 % of $FeSO_4 \cdot 7\,H_2O$ and 40 % of $FeSO_4 \cdot 4\,H_2O$.

The second weight drop begins around 200 °C, corresponding to a weight loss of circa 7.4 %. The decomposition from iron sulfate monohydrate to its anhydrous phase (Equation 3-17) has a theoretical weight loss of 7.0 %, whereas the oxidation of $FeSO_4 \cdot H_2O$ into $FeOHSO_4$ (Equation 3-21), would correspond

to around 0.6 % of weight. Therefore, by the TGA curve in Figure 6.24, it can be assumed that anhydrous iron (II) sulfate is indeed formed.

After 300 °C, the signal shows some stability until around 400 °C. At this point, there is another thermal event can be evidenced, representing the start of the desulfation.This process does not occur in a single step, as seen in the DTG signal. The segmentation of the two reactions is not as clear as seen in the case of zinc sulfate (Figure 6.18), but it is clear that the DTG peak does not represent only one reaction. This analysis agrees with the reaction steps showed in Equation 3-24 and 3-25. The residual weight at the end of the temperature range is around 32 %, corresponding to complete conversion into Fe_2O_3.

It is noticeable that the thermodynamic results indicate the presence of $FeOHSO_4$ (Figure 6.22), which is not observed in the mass balance in the TGA experiments (Figure 6.24). This difference may be caused by the different conditions that each one considers. In the case of the thermodynamic simulation, the system is closed, therefore the atmosphere can have different compositions as the temperature increases. This behavior is not used in the TGA experiments, which have a continuous flow of nitrogen, thus removing all the gaseous species that are formed throughout the experiment.

6.3.3 Kinetic modeling

As discussed in the previous sections, the decomposition reaction steps of iron (II) sulfate is extremely complex and not completely settled. As the proposed kinetic modeling uses the TGA data to estimate the kinetic parameters, the reactions used to develop the differential equations and define the conversion weights are as follows:

$$FeSO_4 \cdot 7\,H_2O \xrightarrow{\Delta} FeSO_4 \cdot 4\,H_2O + 3\,H_2O_{(g)} \tag{3-15}$$

$$FeSO_4 \cdot 4\,H_2O \xrightarrow{\Delta} FeSO_4 \cdot H_2O + 3\,H_2O_{(g)} \tag{3-16}$$

$$FeSO_4 \cdot H_2O \xrightarrow{\Delta} FeSO_4 + H_2O_{(g)} \tag{3-17}$$

$$FeSO_4 \xrightarrow{\Delta} \tfrac{1}{6}\,Fe_2(SO_4)_3 + \tfrac{1}{3}\,Fe_2O_3 + \tfrac{1}{2}\,SO_{2(g)} \tag{3-24}$$

$$\tfrac{1}{6}\,Fe_2(SO_4)_3 \xrightarrow{\Delta} \tfrac{1}{6}\,Fe_2O_3 + \tfrac{1}{2}\,SO_{2(g)} + \tfrac{1}{4}\,O_{2(g)} \tag{3-25}$$

Therefore, it would be necessary to estimate 15 different kinetic parameters to model the decomposition process as a whole. This quantity of parameters would cause the estimation process to be extremely computational expensive. However, as mentioned in Section 6.2.3, the computational cost can

be reduced by dividing the decomposition into two different sets: the dehydration reactions, and the desulfation reactions. Thus, the estimation is also divided into two different sets, one set regarding the dehydration reactions, and another set concerning the desulfation. As mentioned, by dividing the whole process into two sub-systems makes it uncertain that the global minimum is reached.

6.3.3.1 Dehydration

The methodology to model the dehydration reactions is the same as the one used in the previous desulfations (Sections 6.1.3.2 and 6.2.3). It is necessary to establish the reaction steps to properly set the differential equations and their correspondent conversion weights. This approach is similar to the one already used in the decomposition of zinc sulfate.

Considering 1.0 mole of a mixture of 60 % of iron (II) sulfate heptahydrate and 40 % of iron (II) sulfate tetrahydrate, the conversion weights (w_i) are determined by using the theoretical mass balance of the proposed reaction steps. Table 6.7 displays the values of the theoretical weight losses and their respective weight coefficients.

Table 6.7: Theoretical weight loss (wt.%) in each step of the dehydration of iron (II) sulfate heptahydrate.

Reaction	Theoretical weight loss (wt.%)	w_i
Equation 3-15	12.48	0.307
Equation 3-16	21.12	0.520
Equation 3-17	7.04	0.173
Total	40.64	1.0

Figure 6.25 displays the experimental and calculated values for the dehydration of iron (II) sulfate heptahydrate. The model does not fit well at lower temperatures (below 100 °C), perhaps due to the starting composition not being well-defined, which can make the model description not be fully accurate. This behavior is seen also in the following plateaus, which some discrepancies between the model curve and the experimental data.

For temperatures above 100 °C, the model presents a good fitting, even better considering the confidence region of 95 %. The assumption of the initial sample being composed of a ratio of 60 %:40 % of iron (II) sulfate heptahydrate and tetrahydrate, respectively, also seems to be justified as

the weight coefficients make the model curve follow the conversion plateaus correctly. The R^2 fo the whole dehydration process was 0.98, which indicates a excellent overall agreement between the model and experimental data.

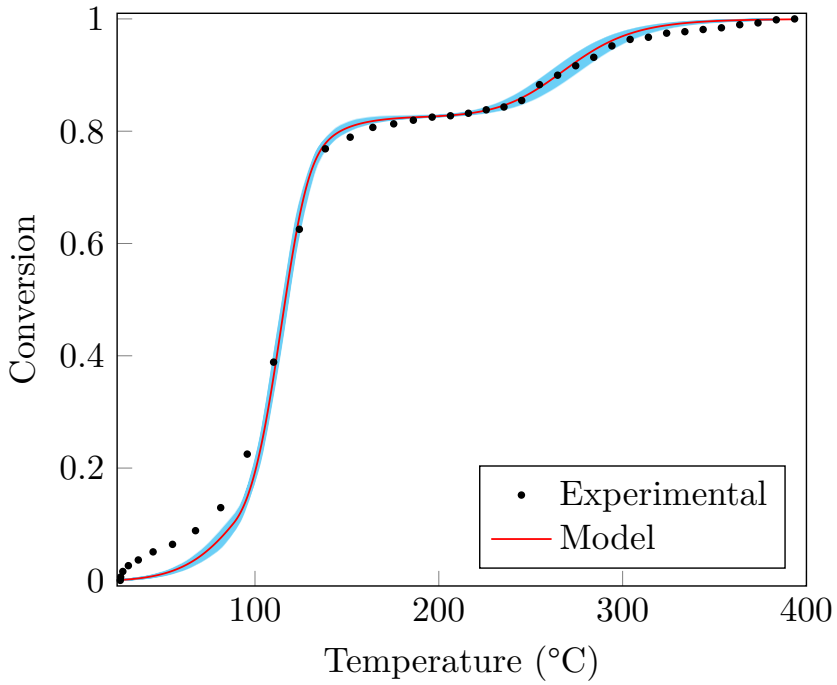

Figure 6.25: Experimental and model conversion of the dehydration of iron sulfate heptahydrate.

The individual conversions of the dehydration reactions are depicted in Figure 6.26. Until 90 °C, only the first of the dehydration occurs. At this temperature, the second dehydration stage begins with a fast behavior. The two stages take place simultaneously until around 150 °C. The difficulty in segmenting the first two dehydration stages in the TGA curve (Figure 6.24) is expressed in the behavior of the red and blue curves. Circa 200 °C, the first and second dehydration stages are finished and the third commences until around 390 °C.

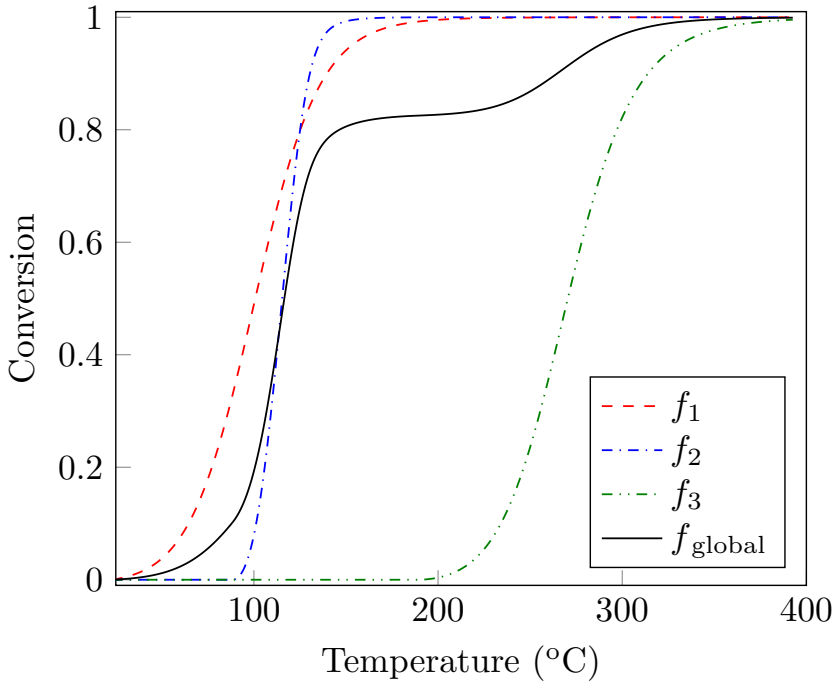

Figure 6.26: Individual and global conversions of the dehydration reactions of iron sulfate heptahydrate.

The performance of the PSO for the dehydration of iron (II) sulfate heptahydrate is shown in Figure 6.27. The behavior is slightly different from what was seen in the cases of the aluminum-bearing compounds (Figure 6.11) and zinc sulfate (Figure 6.21), with fewer iterations needed to reach the global minimum (less than 200). The error decreases greatly in the beginning with very few error decreases throughout the optimization process. This is also observed in the sum of the particles' velocities curve decreasing continuously with small fluctuations.

It is possible that the particles' positions were close to the optimal region, therefore needing less iterations to end the estimation. Another possibility is that the search space does not have a great amount of local minimum regions, which can lead to temporary solutions with more variations in the global error value. Nevertheless, the estimation reached a low error value and the model curve seems well-fitted. The amount of experimental data points used to in the estimation of the dehydration parameters was 38, following the same methodology mentioned in Section 6.1.3.2.

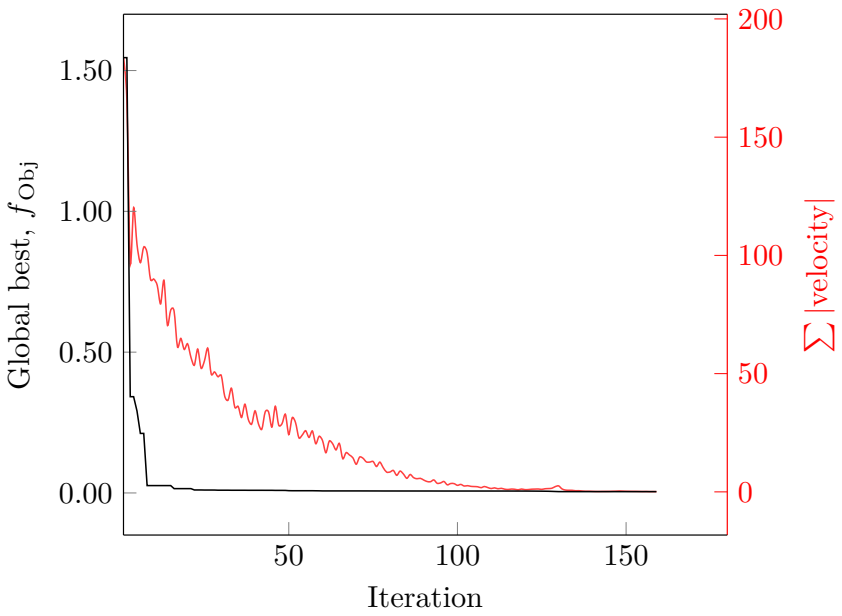

Figure 6.27: Progress of the parameter estimation (error and sum of particle's velocities) in each iteration for the dehydration of iron sulfate heptahydrate.

The kinetic parameters for the dehydration of $FeSO_4 \cdot 7\,H_2O$ estimated using PSO are displayed in Table 6.8. The activation energies show an increase for each reaction. This behavior is consistent with the proposed reaction steps, in which the temperature of dehydration of $FeSO_4 \cdot 7\,H_2O$ (53.3 kJ.mol^{-1}) is lowest one, followed by the dehydration temperature $FeSO_4 \cdot 4\,H_2O$ (88.8 kJ.mol^{-1}), and $FeSO_4 \cdot H_2O$ (124 kJ.mol^{-1}), with the highest dehydration temperature among the evaluated dehydration reactions. Moreover, the reaction orders also showed some discrepancies among each other. The first dehydration step presented a reaction order of 1.65, the second step was 1.12, and the third seems to be a second-order reaction.

Table 6.8: Estimated kinetic parameters for the dehydration of $FeSO_4 \cdot 7\,H_2O$ obtained using PSO.

Reaction	k_0 (min^{-1})	E_a (kJ.mol^{-1})	n
Equation 3-15	2.81×10^6	53.3	1.65
Equation 3-16	7.07×10^{11}	88.8	1.12
Equation 3-17	7.47×10^{10}	124	2.0

There is few kinetic data regarding the dehydration of iron (II) sulfate heptahydrate. Swamy and Prasad[63,80,83] used statistical method to evaluate the different decomposition stages. The author considered that the first dehydration stage consisted of a loss of six water molecules, thus turning Equations 3-15 and 3-16 into one single step. The activation energy determined

for this first dehydration step was 71 kJ.mol^{-1}, whereas the second stage ($FeSO_4 \cdot H_2O$ into $FeSO_4$) had an activation energy of 146 kJ.mol^{-1}. Considering the difference in the reaction steps and modeling technique, the values found in the present work agree with the one found in literature, with the trend of higher activation energy values for processes occurring at higher temperatures.

6.3.3.2 Desulfation

To model the desulfation of the anhydrous iron (II) sulfate, the Equations 3-24 and 3-25 were considered as the reaction steps. Considering 1.0 mole of $FeSO_4$, the conversion weights (w_i) are determined using the theoretical weight loss of the mass balance of the decomposition. The theoretical weight losses of the desulfation reactions and their respective conversion coefficients are displayed in Table 6.9.

Table 6.9: Theoretical weight loss (wt.%) in each step of the desulfation of anhydrous iron (II) sulfate.

Reaction	Theoretical weight loss (wt.%)	w_i
Equation 3-15	12.56	0.258
Equation 3-16	35.18	0.742
Total	47.44	1.0

The desulfation modeling result and the associated experimental data are depicted in Figure 6.28. Somewhat similar to the dehydration case, the model does not completely describe the beginning of the process (between 400 °C and 500 °C). However, the deviations are far less evident in the desulfation case than in the dehydration. For temperatures above 500 °C, the model presents a good fitting with the experimental data, even more considering the confidence region of 95 %. There is a big change in the slope of the model curve at 600 °C due to the action of the two ODEs and their conversion coefficients. Using this modeling technique makes it possible to capture this trend over the formation of an intermediate phase, as seen in the case of zinc (Section 6.2.3). The R^2 value for the desulfation of anhydrous iron (II) sulfate was 0.9994, indicating an excellent agreement of the model with the experimental data.

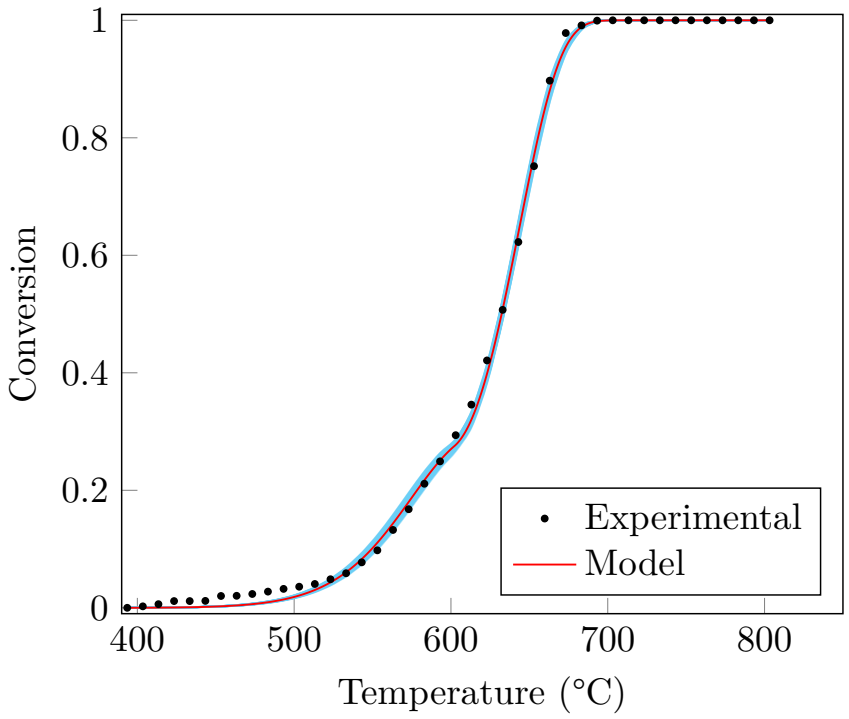

Figure 6.28: Experimental and model conversion of the thermal decomposition of anhydrous iron (II) sulfate.

The individual conversions of the desulfation reactions (Equations 3-24 and 3-25) are shown in Figure 6.29. Until 600 °C, only the first desulfation reactions seems to occur. At higher temperatures, the second reaction begins to take place when the first reaction has almost reached its maximum conversion.

The TGA curves may help to understand the difference in the behavior of the desulfation of the two sulfates. Even though both of them present an intermediate phase in their decomposition, the transition between the phases in much more evident in the case of zinc sulfate (Figure 6.18), where the DTG curve clearly show two separate peaks. In the case of iron (II) sulfate, the transition between phases in smoother, with the DTG curve showing two peaks very close to one another, which may indicate that the transitions occur faster when compared to zinc.

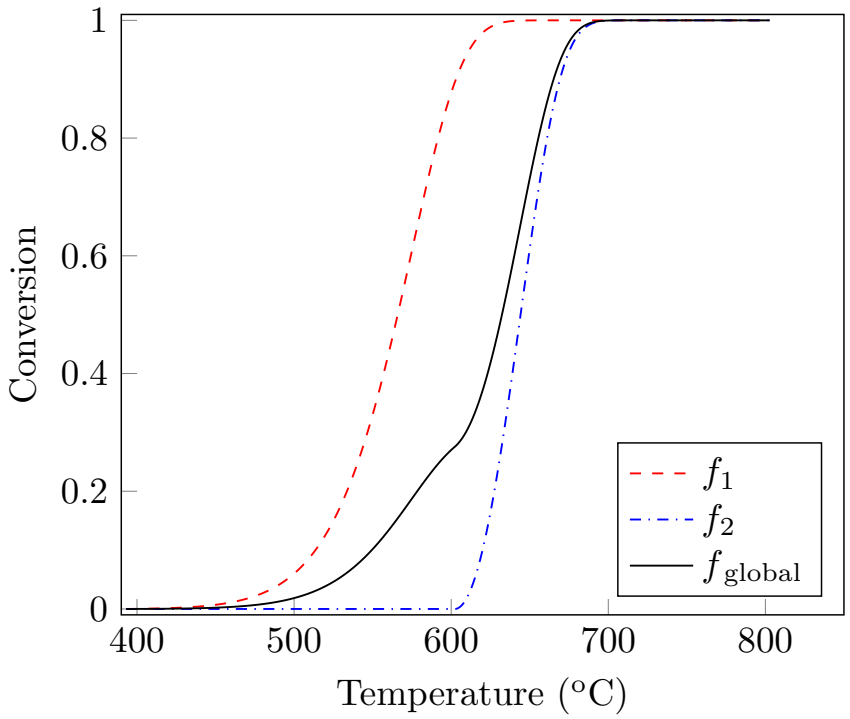

Figure 6.29: Individual and global conversions of the decomposition reactions of anhydrous iron (II) sulfate.

Figure 6.30 depicts the performance of the PSO for the desulfation of anhydrous iron (II) sulfate. The behavior is similar to what was seen in the cases of the aluminum-bearing compounds (Figure 6.11), and zinc (Figure 6.21). The error decreases rapidly at first, reaching a local minimum for a few iterations, and then shows a new great error decrease, leading to a fine-tuning in follow-up iterations. The change in global best error value is also evident in the sum of particles' velocities. Right after the second error decrease, the particles' velocities increase significantly. This trend shows that the particles begun to move to a new place in the search space, being attracted towards the best particle in the flock.

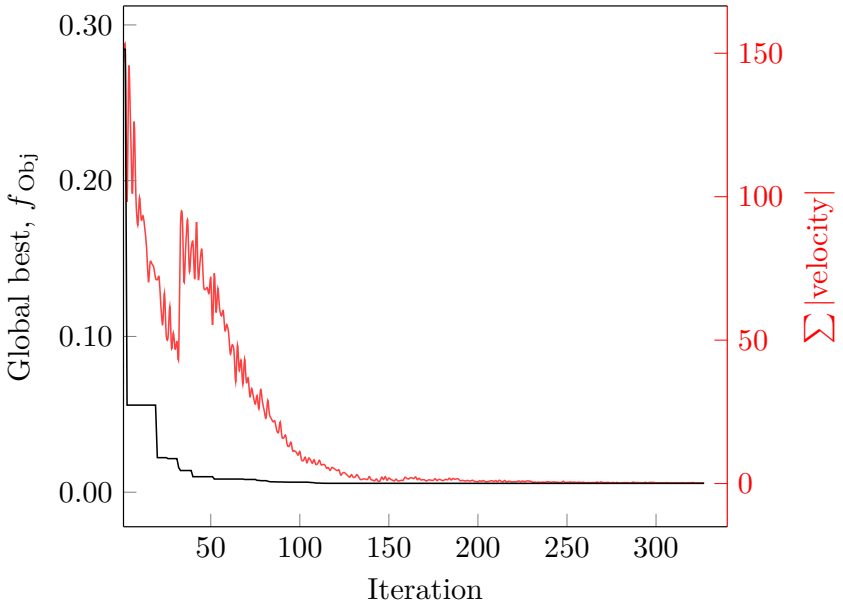

Figure 6.30: Progress of the parameter estimation (error and sum of particle's velocities) in each iteration for the desulfation of iron sulfate.

Table 6.10 shows the estimated kinetic parameters for the desulfation of iron (II) sulfate using PSO. The activation energy regarding to the decomposition of $Fe_2(SO_4)_3$ is higher than the one concerning the decomposition of $FeSO_4$. This trend is expected as the first one decomposes at a higher temperature than the latter. For the decomposition of iron (II) sulfate, the activation energy found was 184 kJ.mol^{-1}. The activation energy values found in the literature present a lot of variation, ranging from 106 kJ.mol^{-1} in the work of Kolta and Askar[84] and 619 kJ.mol^{-1} in the studies of Prasad.[80–83] In a more recent work, Kanari et al.[66] reported an activation energy value 238 kJ.mol^{-1} using inert atmosphere. Therefore, the E_a obtained using PSO is in the same range as the ones reported in the literature.

There is a lack of information in the literature concerning the reaction order data. Huang et al.[78] using different model-free equations reporting the Prout-Tompkins with reaction order of 2.16 as the one with the highest correlation coefficient. This value is very different from the one found using PSO (first-order reaction). This difference could be due to the differences in the modeling strategies employed.

Table 6.10: Estimated kinetic parameters for the desulfation of $FeSO_4$ obtained using PSO.

Reaction	k_0 (min^{-1})	E_a (kJ.mol^{-1})	n
Equation 3-24	6.69×10^{10}	184	1.0
Equation 3-25	4.52×10^{14}	264	1.0

The kinetic data concerning the thermal decomposition of $Fe_2(SO_4)_3$ is also scarce. This happen due to the fact that most of the literature works report the activation energy of iron oxysulfate ($Fe_2O(SO_4)_2$), which can be interpreted as a solid solution of iron (III) sulfate and hematite.

Nevertheless, there are some studies that reported the activation energy of pure $Fe_2(SO_4)_3$. All of them used the Arrhenius plot as the modeling technique to determine the activation energy of the thermal decomposition, which uses isothermal runs to calculate the kinetic parameters. Kolta and Askar[84] used a TG isothermal runs in air atmosphere and reported an activation energy of 106 kJ.mol^{-1}, whereas Wu et al.[85] used a similar approach but using inert atmosphere, reporting 114 kJ.mol^{-1}. Other authors[25,52] stated that the difference in the atmosphere composition affect the initial decomposition temperature and also the activation energy.

Tagawa and Saijo[59] determined the activation energy for the decomposition of $Fe_2(SO_4)_3$ using isothermal runs of pellet samples. The atmosphere composition was high-purity nitrogen. In this case, the reported activation energy was 211.8 kJ.mol^{-1}, which is discordant with the works discussed previously. This happen probably due to the use of pellets instead of powdered samples, as it adds some diffusional effects that can affect mass and heat transfers, the added resistance reflects in the increase in the activation energy values.

The activation energy estimated in the present work was 264 kJ.mol^{-1} for $Fe_2(SO_4)_3$ decomposition. This value is far from the ones reported by the literature, between 106 and 211.8 kJ.mol^{-1}. However, it is worth mentioning that the experimental conditions and modeling techniques were different. Non-isothermal runs were used in the present work instead of the isothermal runs from the authors in the literature.[59,84,85] Furthermore, the modeling was also different, with the estimation of three different kinetic parameters. Hence, it is expected to observe different results, even though the same phenomena is observed.

With the estimated kinetic parameters of the dehydration and desulfation of iron (II) sulfate in hands, it is possible to model the process as a whole. First, it is necessary to define the conversion weights considering 1.0 mole of a mixture of 60 of % $FeSO_4 \cdot 7\,H_2O$ and 40 % of $FeSO_4 \cdot 4\,H_2O$. The theoretical weight losses and the w_i values for every step in the decomposition are displayed in Table 6.11.

Table 6.11: Theoretical weight loss (wt.%) in each step of the decomposition iron (II) sulfate heptahydrate.

Reaction	Theoretical weight loss (wt.%)	w_i
Equation 3-15	12.48	0.181
Equation 3-16	21.12	0.307
Equation 3-17	7.04	0.102
Equation 3-24	7.27	0.106
Equation 3-25	20.89	0.304
Total	68.8	1.0

The complete decomposition of iron (II) sulfate heptahydrate is depicted in Figure 6.31. The model agrees with most of the experimental as seen in Figures 6.25 and 6.28. There is a notable deviation in the beginning of the dehydration process, probably because the initial salt composition not being well-defined. The R^2 value in this case was 0.9993, showing an excellent fitting. Moreover, the advantage of using the PSO in two sub-processes (dehydration and desulfation) is that each estimation takes less time and computational effort than optimizing the whole process at once.

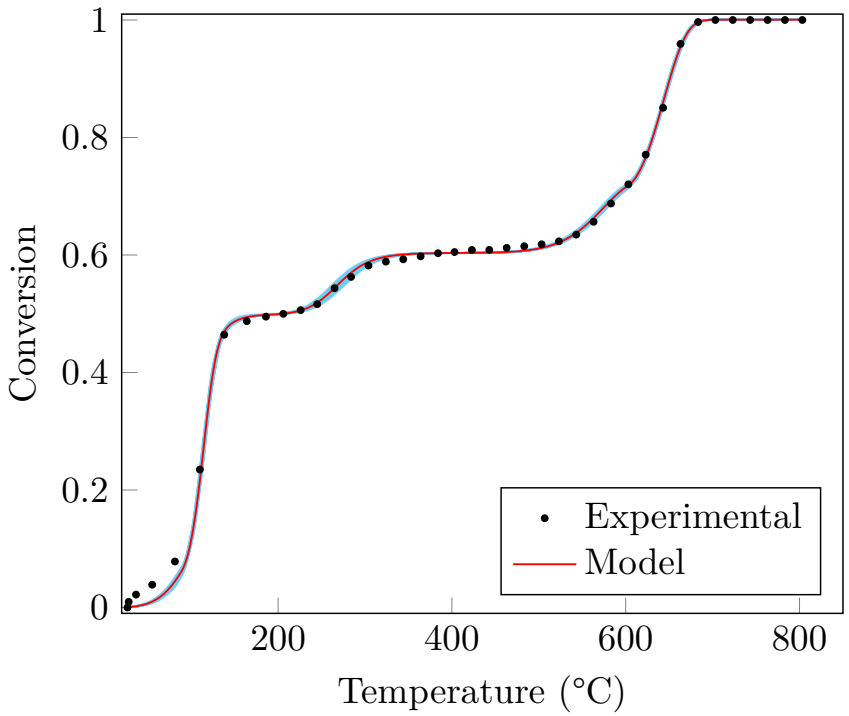

Figure 6.31: Experimental and model conversion of the thermal decomposition of iron (II) sulfate heptahydrate.

7
Conclusions

The thermodynamic simulations helped to understand the theoretical possibilities of the reaction mechanisms. By performing simulations of the equilibrium composition as a function of the temperature, it was possible to know which solid phases and gaseous were probably present in the tests' conditions, allowing the development of the mechanisms.

In the case of the aluminum-bearing compounds, it was noted that pure aluminum sulfate decomposed at higher temperatures than potassium alum, and the mixture of aluminum sulfate and potassium sulfate. This behavior indicated that the presence of potassium sulfate may catalyze the decomposition of aluminum sulfate.

By the graphical method, the activation energies were 264.4 kJ.mol^{-1} for $Al_2(SO_4)_3$, 233.1 kJ.mol^{-1} for $KAl(SO_4)_2$, and 209.3 kJ.mol^{-1} for the mixture of $Al_2(SO_4)_3$ and K_2SO_4. The apparent reaction order in all cases were close to 1.7. For the ODE method, the estimated activation energies were higher than the ones of the graphical method but they were consistent as aluminum sulfate showed the highest value (352.4 kJ.mol^{-1}), followed by potassium alum (328.3 kJ.mol^{-1}), and mixture of aluminum sulfate and potassium sulfate (296.3 kJ.mol^{-1}). When using the ODE method, the reaction order was around 1.5 for potassium alum and mixture of sulfates, and 1.0 for pure aluminum sulfate. This might indicate that potassium alum, and the mixture of sulfates may have a similar decomposition mechanism, which cannot be seen in graphical method. Moreover, the activation energy for both methods showed that the presence of potassium sulfate reduced the activation energy in the decomposition.

The thermal runs of zinc sulfate showed that the salt did not decompose in a single-step reaction. First, the salt decomposed into an intermediate phase (zinc oxysulfate), and then into zinc oxide. This behavior makes it difficult to use the graphical method, therefore only the ODE method was used. The activation energy of the decomposition of $ZnO \cdot 2\,ZnSO_4$ (367 kJ.mol^{-1}) was higher than the one related to the decomposition of $ZnSO_4$ (272 kJ.mol^{-1}). Regarding the reaction orders, the decomposition of zinc sulfate was a second-order reaction, and the decomposition of zinc oxysulfate was a first-order reaction.

The three dehydration reactions presented increasing activation energies: 53.3 kJ.mol^{-1}, 88.8 kJ.mol^{-1}, and 124 kJ.mol^{-1}. This behavior is expected as there is crescent demand of energy to remove water molecules that may be

within the molecular structure. The reaction order values were different from one another: 1.65, 1.12, and 2.0. As for the desulfation, the decomposition of anhydrous $FeSO_4$ presented an activation energy of 184 kJ.mol^{-1}, and the intermediate phase ($Fe_2(SO_4)_3$) had an activation energy of 264 kJ.mol^{-1}. Both reaction turned out to be of first-order.

The kinetic modeling technique developed using system of differential equations, and PSO as an estimation tool was successful in simulating all the sulfates systems. In all cases the R^2 values were higher than 0.98, showing that the ODE method had an excellent performance when comparing the model and experimental values. Moreover, the proposed method was able to successfully describe both simple and complex systems, which is not possible when using the graphical method. In the present case, the desulfation of zinc sulfate, and the dehydration and desulfation of iron (II) sulfate would probably yield not very accurate results due to the difficulty in segmenting the different reactions involved in these mechanisms.

8
Future works

- Perform the TGA in dynamic heating rates to better segment certain decomposition steps;
- Perform multiple TG runs in the same conditions to ensure experimental reproducibility;
- Simultaneously optimize the 15 kinetic parameters of the iron (II) sulfate system;
- Characterize (XRD and SEM/EDS) studied materials before and after the decomposition to better give support for the mechanisms proposed;
- Apply the ODE method coupled with PSO in other systems. Use it in other inorganic systems, such as other sulfates, carbonates, and nitrates, as well as organic systems, such as biomass pyrolisis;
- Simulate the reaction mechanisms in computational fluid dynamics software, such as COMSOL, using the estimated kinetic parameters to study the diffusional aspects of the decomposition;
- Use the estimated kinetic parameters in runs with heating rates that were not used in the estimation of the present work.
- Analyze the effect of each parameter and systematic errors in the model by using more sensitive statistical analysis, such as the residual standard deviation analysis.

9
Bibliography

1 ASSELT, H. van. Governing fossil fuel production in the age of climate disruption: Towards an international law of 'leaving it in the ground'. **Earth System Governance**, v. 9, p. 100118, set. 2021.

2 WELSBY, D.; PRICE, J.; PYE, S.; EKINS, P. Unextractable fossil fuels in a 1.5 °C world. **Nature**, v. 597, n. 7875, p. 230–234, set. 2021.

3 MCGLADE, C.; EKINS, P. The geographical distribution of fossil fuels unused when limiting global warming to 2 °C. **Nature**, v. 517, n. 7533, p. 187–190, jan. 2015.

4 MEINSHAUSEN, M.; MEINSHAUSEN, N.; HARE, W.; RAPER, S. C. B.; FRIELER, K.; KNUTTI, R.; FRAME, D. J.; ALLEN, M. R. Greenhouse-gas emission targets for limiting global warming to 2 °C. **Nature**, v. 458, n. 7242, p. 1158–1162, abr. 2009.

5 CARMO, M.; FRITZ, D. L.; MERGEL, J.; STOLTEN, D. A comprehensive review on PEM water electrolysis. **International Journal of Hydrogen Energy**, v. 38, n. 12, p. 4901–4934, abr. 2013.

6 CAVALIERE, P. D.; PERRONE, A.; SILVELLO, A. Water Electrolysis for the Production of Hydrogen to Be Employed in the Ironmaking and Steelmaking Industry. **Metals**, v. 11, n. 11, p. 1816, nov. 2021.

7 SAID, S. A.; WASEEUDDIN, M.; SIMAKOV, D. S. A review on solar reforming systems. **Renewable and Sustainable Energy Reviews**, v. 59, p. 149–159, jun. 2016.

8 MATSUMURA, Y.; NAKAMORI, T. Steam reforming of methane over nickel catalysts at low reaction temperature. **Applied Catalysis A: General**, v. 258, n. 1, p. 107–114, fev. 2004.

9 WANG, B.; PENG, Y.; YAO, S. Oxidative reforming of n-heptane in gliding arc plasma reformer for hydrogen production. **International Journal of Hydrogen Energy**, v. 44, n. 41, p. 22831–22840, ago. 2019.

10 ISMAIL, A. A.; BAHNEMANN, D. W. Photochemical splitting of water for hydrogen production by photocatalysis: A review. **Solar Energy Materials and Solar Cells**, v. 128, p. 85–101, set. 2014.

11 BHOSALE, R. R.; KUMAR, A.; BROEKE, L. J. van den; GHARBIA, S.; DARDOR, D.; JILANI, M.; FOLADY, J.; AL-FAKIH, M. S.; TARSAD, M. A. Solar hydrogen production via thermochemical iron oxide–iron sulfate water splitting cycle. **International Journal of Hydrogen Energy**, v. 40, n. 4, p. 1639–1650, jan. 2015.

12 BHOSALE, R.; KUMAR, A.; ALMOMANI, F.; GUPTA, R. B. Solar thermochemical $ZnO/ZnSO_4$ water splitting cycle for hydrogen production. **International Journal of Hydrogen Energy**, v. 42, n. 37, p. 23474–23483, set. 2017.

13 SAFARI, F.; DINCER, I. A review and comparative evaluation of thermochemical water splitting cycles for hydrogen production. **Energy Conversion and Management**, v. 205, p. 112182, fev. 2020.

14 MELLO, N. M.; REGO, A. S. C.; BROCCHI, E. A.; CAMPOS, J. B. d.; MOURA, F. J.; SOUZA, R. F. M. Effect of an Alumina Supported Palladium Catalyst on the Magnesium Sulfate Decomposition Kinetics. **Materials Research**, v. 23, n. 6, p. e20200344, 2020.

15 OSTROFF, A.; SANDERSON, R. Thermal stability of some metal sulphates. **Journal of Inorganic and Nuclear Chemistry**, v. 9, n. 1, p. 45–50, jan 1959.

16 MENICACCI, E.; ROTUREAU, P.; FAYET, G.; ADAMO, C. Toward the Mechanistic Understanding of the Additives' Role on Ammonium Nitrate Decomposition: Calcium Carbonate and Calcium Sulfate as Case Studies. **ACS Omega**, v. 5, n. 10, p. 5034–5040, mar. 2020.

17 BHOSALE, R. R. Thermochemical H_2 production via solar driven hybrid $SrO/SrSO_4$ water splitting cycle. **International Journal of Hydrogen Energy**, v. 44, n. 1, p. 118–127, jan. 2019.

18 BHOSALE, R. R.; ALMOMANI, F.; RASHID, S. Solar thermochemical H_2 production via $MnSO_4/MnO$ water splitting cycle: Thermodynamic equilibrium and efficiency analysis. **International Journal of Hydrogen Energy**, v. 45, n. 17, p. 10324–10333, mar. 2020.

19 BHOSALE, R. R. A novel three-step GeO_2/GeO thermochemical water splitting cycle for solar hydrogen production. **International Journal of Hydrogen Energy**, v. 45, n. 10, p. 5816–5828, fev. 2020.

20 BHOSALE, R. R. Solar hydrogen production via thermochemical magnesium oxide – Magnesium sulfate water splitting cycle. **Fuel**, v. 275, p. 117892, set. 2020.

21 SOUZA, R.; NAVARRO, R.; GRILLO, A. V.; BROCCHI, E. Potassium alum thermal decomposition study under non-reductive and reductive conditions. **Journal of Materials Research and Technology**, v. 8, n. 1, p. 745–751, 2019.

22 SOUZA, B.; SOUZA, R.; SANTOS, I.; BROCCHI, E. $MgSO_4$ carbothermic reductive decomposition to produce a highly reactive MgO powder. **Journal of Materials Research and Technology**, v. 9, n. 2, p. 1847–1855, mar. 2020.

23 SOTO-DÍAZ, O.; OROZCO-MENA, R. E.; ROMÁN-AGUIRRE, M.; ROMERO-PAREDES, H.; CAMACHO-DÁVILA, A. A.; RAMOS-SÁNCHEZ,

V. H. Metal sulfate decomposition using green pd-based catalysts supported on γAl_2O_3 and SiC: a common step in sulfur-family thermochemical cycles. **International Journal of Hydrogen Energy**, Elsevier, v. 44, n. 24, p. 12309–12314, 2019.

24 MU, J.; PERLMUTTER, D. D. Thermal decomposition of inorganic sulfates and their hydrates. **Industrial & Engineering Chemistry Process Design and Development**, v. 20, n. 4, p. 640–646, oct 1981.

25 NARAYAN, R.; TABATABAIE-RAISSI, A.; ANTAL, M. J. A Study of Zinc Sulfate Decomposition at Low Heating Rates. **Industrial & Engineering Chemistry Research**, American Chemical Society, v. 27, n. 6, p. 1050–1058, jun 1988.

26 APTE, N. G.; KIRAN, E.; CHERNOSKY, J. V. Thermal decomposition of aluminium-bearing compounds. **Journal of Thermal Analysis**, Kluwer Academic Publishers, v. 34, n. 4, p. 975–981, jul 1988.

27 REGO, A. S.; MARPRATES, C. V.; SILVA, T. S.; NETO, J. G.; NAVARRO, R. C.; SOUZA, R. F.; BROCCHI, E. A. $KAl(SO_4)_2$ thermal decomposition kinetics modeling through graphical and PSO methods. **Journal of Materials Research and Technology**, p. 1975–1984, jul. 2021.

28 CHOU, K.-S.; SOONG, C.-S. Kinetics of the thermal decomposition of aluminum sulfate. **Thermochimica Acta**, v. 78, n. 1-3, p. 285–295, jul 1984.

29 INGRAHAM, T. R.; MARIER, P. Kinetics of the thermal decomposition of $ZnSO_4$ and $ZnO \cdot 2\,ZnSO_4$. **Canadian Metallurgical Quarterly**, v. 6, n. 3, p. 249–261, jul. 1967.

30 ONUKI, K.; SHIMIZU, S.; NAKAJIMA, H.; IKEZOE, Y.; SATO, S. Kinetics of the Thermal Decomposition of Nickel Sulfate. **Bulletin of the Chemical Society of Japan**, v. 56, n. 11, p. 3294–3296, nov 1983.

31 APTE, N. G.; KIRAN, E.; HASSLER, J. C.; CHERNOSKY, J. V. Kinetic Modeling of Thermal Decomposition of Aluminum Sulfate. **Chemical Engineering Communications**, v. 74, n. 1, p. 47–61, 1988.

32 KÜÇÜK, F.; YILDIZ, K. The decomposition kinetics of mechanically activated alunite ore in air atmosphere by thermogravimetry. **Thermochimica Acta**, v. 448, n. 2, p. 107–110, sep 2006.

33 ÇILGI, G. K.; CETIŞLI, H. Thermal decomposition kinetics of aluminum sulfate hydrate. **Journal of Thermal Analysis and Calorimetry**, v. 98, n. 3, p. 855–861, dec 2009.

34 STRASZKO, J.; OLSZAK-HUMIENIK, M.; MOZEJKO, J. Kinetics of Thermal Decomposition of $ZnSO_4 \cdot 7\,H_2O$. **Thermochimica Acta**, v. 292, n. 1-2, p. 145–150, may 1997.

35 WOJCIECHOWSKA, R.; WOJCIECHOWSKI, W.; KAMIŃSKI, J. Thermal decompositions of ammonium and potassium alums. **Journal of Thermal Analysis**, Kluwer Academic Publishers, v. 33, n. 2, p. 503–509, jun 1988.

36 VACHUŠKA, J.; VOBOŘIL, M. Kinetic data computation from non-isothermal thermogravimetric curves of non-uniform heating rate. **Thermochimica Acta**, v. 2, n. 5, p. 379–392, jul. 1971.

37 HELMBOLDT, O.; HUDSON, L. K.; MISRA, C.; WEFERS, K.; HECK, W.; STARK, H.; DANNER, M.; RÖSCH, N. Aluminum Compounds, Inorganic. In: **Ullmann's Encyclopedia of Industrial Chemistry**. Weinheim, Germany: Wiley-VCH Verlag GmbH & Co. KGaA, 2007.

38 KISHIMURA, H.; IMASU, Y.; MATSUMOTO, H. Thermal dehydration of potash alum studied by Raman spectroscopy and X-ray diffraction analysis. **Materials Chemistry and Physics**, v. 149-150, p. 99–104, jan 2015.

39 KARDOS, A. F.; TÓTH, J.; TRIF, L.; GYENIS, J.; FECZKÓ, T. Preparation of spherical agglomerates from potash alum. **RSC Advances**, v. 6, n. 7, p. 5466–5473, 2016.

40 PACEWSKA, B.; PYSIAK, J.; KLEPAŃSKA, A. The investigations of thermal decomposition process of basic aluminium potassium sulfate in the reduced conditions. **Thermochimica Acta**, Elsevier, v. 92, n. C, p. 657–659, sep 1985.

41 PYSIAK, J.; GLINKA, A. Thermal decomposition of basic aluminium potassium sulphate. Part I. Stages of decomposition. **Thermochimica Acta**, v. 44, n. 1, p. 21–28, 1981.

42 PYSIAK, J.; GLINKA, A. Thermal decomposition of basic aluminium potassium sulfate. Part II. Kinetics of the reaction. **Thermochimica Acta**, v. 44, n. 1, p. 29–36, 1981.

43 DAI, J. F.; LING, R. Q.; WANG, K. Z. Thermal Performance and Dehydration Kinetics of $KAl(SO_4)_2 \cdot 12\,H_2O$ as Phase Change Material. **Advanced Materials Research**, Trans Tech Publications Ltd, v. 418-420, p. 282–285, dec 2011.

44 MESHRAM, A.; GAUTAM, D.; SINGH, K. K. Recycling of White Aluminium Dross: Production of Potash Alum. **Transactions of the Indian Institute of Metals**, Springer India, v. 73, n. 5, p. 1239–1248, may 2020.

45 DMITRICHEVA, E. V.; MAKAROVA, I. P.; GREBENEV, V. V.; DOLBININA, V. V.; VERIN, I. A. Preparation and studies of new crystals in the $K_3H(SO_4)_2 - (NH_4)_3H(SO_4)_2 - H_2O$ system. **Crystallography Reports**, v. 59, n. 3, p. 344–352, maio 2014.

46 NODA, Y.; UCHIYAMA, S.; KAFUKU, K.; KASATANI, H.; TERAUCHI, H. Structure Analysis and Hydrogen Bond Character of $K_3H(SO_4)_2$. **Journal of the Physical Society of Japan**, v. 59, n. 8, p. 2804–2810, ago. 1990.

47 CHISHOLM, C. R. I.; HAILE, S. M. High-temperature phase transitions in $K_3H(SO_4)_2$. **Solid State Ionics**, v. 145, n. 1, p. 179–184, dez. 2001.

48 VRIES, K. J. D.; GELLINGS, P. J. The thermal decomposition of potassium and sodium-pyrosulfate. **Journal of Inorganic and Nuclear Chemistry**, v. 31, n. 5, p. 1307–1313, maio 1969.

49 PAPAZIAN, H.; PIZZOLATO, P.; ORRELL, R. The Thermal Decomposition of Aluminum Sulfate and Hafnium Sulfate. **Thermochimica Acta**, v. 4, n. 2, p. 97–103, 1972.

50 PELOVSKI, Y.; PIETKOVA, W.; GRUNCHAROV, I.; PACEWSKA, B.; PYSIAK, J. The thermal decomposition of aluminum sulfate in different gas phase environments. **Thermochimica Acta**, v. 205, p. 219–224, aug 1992.

51 KÜÇÜK, A.; GÜLABOĞLU, M. c. Thermal Decomposition of şaphane Alunite Ore. **Industrial & Engineering Chemistry Research**, v. 41, n. 24, p. 6028–6032, nov. 2002.

52 JOHNSON, D. W.; GALLAGHER, P. K. Kinetics of the Decomposition of Freeze-Dried Aluminum Sulfate and Ammonium Aluminum Sulfate. **Journal of the American Ceramic Society**, v. 54, n. 9, p. 461–465, set. 1971.

53 WARNER, N. A.; INGRAHAM, T. R. Kinetic studies of the thermal decomposition of ferric sulphate and aluminum sulphate. **The Canadian Journal of Chemical Engineering**, v. 40, n. 6, p. 263–267, dez. 1962.

54 HABASHI, F. (Ed.). **Handbook of extractive metallurgy**. Weinheim ; New York: Wiley-VCH, 1997. ISBN 978-3-527-28792-5.

55 TABATABAIE-RAISSI, A.; NARAYAN, R.; MOK, W. S. L.; ANTAL, M. J. Solar Thermal, Decomposition Kinetics of Zinc Sulfate at High Heating Rates. **Industrial & Engineering Chemistry Research**, McGraw-Hill, v. 28, n. 3, p. 355–362, mar 1989.

56 IBANEZ, J. G.; WENTWORTH, W. E.; BATTEN, C. F.; CHEN, E. C. M. Kinetics of the thermal decomposition of zinc sulfate. **Revue Internationale des Hautes Temperatures et des Refractaires**, v. 21, n. 2, p. 113–124, 1984.

57 DUCARROIR, M.; ROMEROPAREDES, H.; STEINMETZ, D.; SIBIEUDE, F.; TMAR, M. On the kinetics of the thermal decomposition of sulfates related with hydrogen water splitting cycles. **International Journal of Hydrogen Energy**, v. 9, n. 7, p. 579–585, 1984.

58 TAGAWA, H. Thermal decomposition temperatures of metal sulfates. **Thermochimica Acta**, Elsevier, v. 80, n. 1, p. 23–33, oct 1984.

59 TAGAWA, H.; SAIJO, H. Kinetics of the thermal decomposition of some transition metal sulfates. **Thermochimica Acta**, v. 91, p. 67–77, sep 1985.

60 SIRIWARDANE, R. V.; Poston Jr, J. A.; FISHER, E. P.; SHEN, M.; MILTZ, A. L. Decomposition of the sulfates of , iron (II), iron (III), nickel, and zinc: XPS, SEM, DRIFTS, XRD, and TGA study. **Applied Surface Science**, Elsevier Science Publishers B.V., v. 152, n. 3-4, p. 219–236, nov 1999.

61 KURBAN, G. V. T.; REGO, A. S. C.; MELLO, N. M.; BROCCHI, E. A.; NAVARRO, R. C. S.; SOUZA, R. F. M. Thermodynamics and kinetic modeling of the $ZnSO_4 \cdot H_2O$ thermal decomposition in the presence of a Pd/Al_2O_3 catalyst. **Energies**, v. 15, n. 2, p. 548, jan. 2022.

62 WANG, T.; DEBELAK, K. A.; ROTH, J. A. Dehydration of iron(II) sulfate heptahydrate. **Thermochimica Acta**, v. 462, n. 1-2, p. 89–93, out. 2007.

63 SWAMY, M.; PRASAD, T. Kinetics of the thermal decomposition of iron(II) sulphate heptahydrate in air. **Thermochimica Acta**, v. 62, n. 2-3, p. 229–236, abr. 1983.

64 MITCHELL, A. G. The preparation and characterization of ferrous sulphate hydrates. **Journal of Pharmacy and Pharmacology**, v. 36, n. 8, p. 506–510, abr. 1984.

65 PETKOVA, V.; PELOVSKI, Y.; PANEVA, D.; MITOV, I. Influence of gas media on the thermal decomposition of second valence iron sulphates. **Journal of Thermal Analysis and Calorimetry**, v. 105, n. 3, p. 793–803, set. 2011.

66 KANARI, N.; MENAD, N.-E.; OSTROSI, E.; SHALLARI, S.; DIOT, F.; ALLAIN, E.; YVON, J. Thermal Behavior of Hydrated Iron Sulfate in Various Atmospheres. **Metals**, v. 8, n. 12, p. 1084, dez. 2018.

67 VENTRUTI, G.; VENTURA, G. D.; GOMEZ, M. A.; CAPITANI, G.; SBROSCIA, M.; SODO, A. High-temperature study of basic ferric sulfate, $FeOHSO_4$. **Physics and Chemistry of Minerals**, v. 47, n. 10, p. 43, out. 2020.

68 SWAMY, M. S. R.; PRASAD, T. P.; SANT, B. R. Thermal analysis of ferrous sulphate heptahydrate in air: Part I. Some general remarks and methods. **Journal of Thermal Analysis**, v. 15, n. 2, p. 307–314, abr. 1979.

69 SWAMY, M. S. R.; PRASAD, T. P.; SANT, B. R. Thermal analysis of ferrous sulphate heptahydrate in air: II. The oxidation-decomposition path. **Journal of Thermal Analysis**, v. 16, n. 2, p. 471–478, ago. 1979.

70 KAMEL, A. H.; SAWIRES, Z.; KHALIFA, H.; SALEH, S. A.; ABDALLAH, A. M. The thermal decomposition of ferrous sulphate heptahydrate. I. Dehydration and oxidation. **Journal of Applied Chemistry and Biotechnology**, v. 22, n. 5, p. 591–598, abr. 1972.

71 GALLAGHER, P. K.; JOHNSON, D. W.; SCHREY, F. Thermal Decomposition of Iron(II) Sulfates. **Journal of the American Ceramic Society**, v. 53, n. 12, p. 666–670, dez. 1970.

72 PELOVSKI, Y.; PETKOVA, V.; NIKOLOV, S. Study of the mechanism of the thermochemical decomposition of ferrous sulphate monohydrate. **Thermochimica Acta**, v. 274, p. 273–280, mar. 1996.

73 NETO, K.; GARG, V. Mössbauer thermal decomposition studies of Fe(II) sulphate. **Journal of Inorganic and Nuclear Chemistry**, v. 37, n. 11, p. 2287–2290, nov. 1975.

74 LACALAMITA, M.; VENTRUTI, G.; VENTURA, G. D.; RADICA, F.; MAURO, D.; SCHINGARO, E. In Situ High-Temperature X-ray Powder Diffraction and Infrared Spectroscopic Study of Melanterite, $FeSO_4 \cdot 7\,H_2O$. **Minerals**, v. 11, n. 4, p. 392, abr. 2021.

75 MASSET, P.; POINSO, J. Y.; POIGNET, J. C. TG/DTA/MS Study of the thermal decomposition of $FeSO_4 \cdot 6\,H_2O$. **Journal of Thermal Analysis and Calorimetry**, v. 83, n. 2, p. 457–462, fev. 2006.

76 TRIVEDI, M. K.; JANA, S. Evaluation of the physicochemical, thermal and behavioural properties of consciousness energy healing treated iron (II) sulphate. **Biointerface Research in Applied Chemistry**, v. 9, n. 5, p. 4292–4300, out. 2019.

77 JOHNSON, D. W.; GALLAGHER, P. K. Kinetics of the decomposition of freeze-dried iron(II) sulfate. **The Journal of Physical Chemistry**, v. 75, n. 9, p. 1179–1185, abr. 1971.

78 HUANG, P.; DENG, S.; ZHANG, Z.; WANG, X.; CHEN, X.; YANG, X.; YANG, L. A sustainable process to utilize ferrous sulfate waste from titanium oxide industry by reductive decomposition reaction with pyrite. **Thermochimica Acta**, v. 620, p. 18–27, nov. 2015.

79 KUBO, T.; TANIGUCHI, M.; SHIRASAKI, S.-i. The Thermal Decomposition of Ferrous Sulphate Hepta-hydrate. **The Journal of the Society of Chemical Industry, Japan**, v. 64, n. 2, p. 256–261, 1961.

80 PRASAD, T. P. Kinetics of the thermal decomposition of hydrates and basic salts of $FeSO_4$. **Journal of Thermal Analysis**, v. 35, n. 7, p. 2539–2542, nov. 1989.

81 PRASAD, T. P. Kinetics of thermal decomposition of intermediate hydrates and basic salts of iron(II) sulphate heptahydrate. **Journal of Thermal Analysis**, v. 31, n. 3, p. 553–557, maio 1986.

82 PRASAD, T. Thermal decomposition of commercial ferric sulphates. **Journal of Inorganic and Nuclear Chemistry**, v. 34, n. 3, p. 1094–1098, mar. 1972.

83 PRASAD, T. Kinetics from thermogravimetric traces. **Thermochimica Acta**, v. 65, n. 1, p. 147–149, jul. 1983.

84 KOLTA, G.; ASKAR, M. Thermal decomposition of some metal sulphates. **Thermochimica Acta**, Elsevier, v. 11, n. 1, p. 65–72, jan 1975.

85 WU, H.; JESPERSEN, J. B.; FRANDSEN, F. J.; GLARBORG, P.; AHO, M.; PAAKKINEN, K.; TAIPALE, R. Modeling of ferric sulfate decomposition and sulfation of potassium chloride during grate-firing of biomass. **AIChE Journal**, v. 59, n. 11, p. 4314–4324, nov. 2013.

86 SPEYER, R. F. **Thermal analysis of materials**. New York: Marcel Dekker, 1994. (Materials engineering, 5). ISBN 978-0-8247-8963-3.

87 BEJAOUI, A.; SOUAMTI, A.; KAHLAOUI, M.; LOZANO-GORRÍN, A. D.; Morales Palomino, J.; Ben Hassen Chehimi, D. Synthesis, characterization, thermal analysis and electrical properties of $(NH_4)_2M(SO_4)_2 \cdot 6\,H_2O$ (M = Cu, Co, Ni). **Materials Science and Engineering: B**, Elsevier Ltd, v. 240, p. 97–105, jan 2019.

88 KOGA, N.; KAMENO, N.; TSUBOI, Y.; FUJIWARA, T.; NAKANO, M.; NISHIKAWA, K.; MURATA, A. I. Multistep thermal decomposition of granular sodium perborate tetrahydrate: a kinetic approach to complex reactions in solid–gas systems. **Physical Chemistry Chemical Physics**, v. 20, n. 18, p. 12557–12573, 2018.

89 ZHANG, M.-h.; CHEN, X.; DONG, H. A study on multistep thermal decomposition behavior and kinetics of magnesium nitrate hydrate. **Thermochimica Acta**, v. 701, p. 178951, jul. 2021.

90 GONG, L.; GUO, Y.; MENG, L.; LI, J.; YANG, R. Kinetics Model Reconstruction for Multistep Overlapping Thermal Decomposition of Ammonium Perchlorate with and without the Copper Oxide Compound Catalyst. **Combustion Science and Technology**, v. 193, n. 16, p. 2856–2871, dez. 2021.

91 MURAVYEV, N. V.; KOGA, N.; MEEROV, D. B.; PIVKINA, A. N. Kinetic analysis of overlapping multistep thermal decomposition comprising exothermic and endothermic processes: thermolysis of ammonium dinitramide. **Physical Chemistry Chemical Physics**, v. 19, n. 4, p. 3254–3264, 2017.

92 HILDENBRAND, D. L.; LAU, K. H.; BRITTAIN, R. D. Mechanistic Aspects of Metal Sulfate Decomposition Processes. In: **Materials Chemistry at High Temperatures**. Totowa, NJ: Humana Press, 1990. v. 26, n. pt 1, p. 427–440.

93 GADALLA, A. M. Kinetics of thermal decomposition of $CuSO_4 \cdot 5\,H_2O$ to CuO: THERMAL DECOMPOSITION OF $CuSO_4 \cdot 5\,H_2O$ TO CuO. **International Journal of Chemical Kinetics**, v. 16, n. 6, p. 655–668, jun. 1984.

94 NOFAL, R. B. **Modelagem, simulação e estimação de parâmetros da decomposição térmica do alúmen de potássio**. Tese (Master) — Pontifícia Universidade Católica do Rio de Janeiro, Rio de Janeiro, Brazil, dez. 2018.

95 SCHWAAB, M.; PINTO, J. C. **Análise de Dados Experimentais: I. Fundamentos de Estatística e Estimação de Parâmetros**. Rio de Janeiro, Brazil: Editora E-papers, 2007. ISBN 978-85-7650-136-7.

96 ROS, S. D.; SCHWAAB, M.; PINTO, J. C. Parameter Estimation and Statistical Methods. In: **Reference Module in Chemistry, Molecular Sciences and Chemical Engineering**. [S.l.]: Elsevier, 2017. p. 1–20. ISBN 978-0-12-409547-2.

97 BRANDÃO, A. L. T. **Discriminação de modelos cinéticos de ramificação usando dados de distribuição de massa molar em sistemas de polimerização**. Tese (Master) — PEQ/COPPE, Rio de Janeiro, Brazil, abr. 2014.

98 KENNEDY, J.; EBERHART, R. Particle swarm optimization. In: **Proceedings of ICNN'95 - International Conference on Neural Networks**. Perth, WA, Australia: IEEE, 1995. v. 4, p. 1942–1948. ISBN 978-0-7803-2768-9.

99 DAS, S.; ABRAHAM, A.; KONAR, A. Particle Swarm Optimization and Differential Evolution Algorithms: Technical Analysis, Applications and Hybridization Perspectives. In: KACPRZYK, J.; LIU, Y.; SUN, A.; LOH, H. T.; LU, W. F.; LIM, E.-P. (Ed.). **Advances of Computational Intelligence in Industrial Systems**. Berlin, Heidelberg: Springer Berlin Heidelberg, 2008. v. 116, p. 1–38. ISBN 978-3-540-78296-4 978-3-540-78297-1.

100 LEE, K.; PARK, J.-b. Application of Particle Swarm Optimization to Economic Dispatch Problem: Advantages and Disadvantages. In: **2006 IEEE PES Power Systems Conference and Exposition**. Atlanta, Georgia, USA: IEEE, 2006. p. 188–192. ISBN 978-1-4244-0177-2.

101 REGO, A. S. C.; BRANDÃO, A. L. T. Parameter Estimation and Kinetic Monte Carlo Simulation of Styrene and n -Butyl Acrylate Copolymerization through ATRP. **Industrial & Engineering Chemistry Research**, v. 60, n. 23, p. 8396–8408, jun. 2021.

102 BRANDÃO, A. L. T.; OECHSLER, B. F.; GOMES, F. W.; SOUZA, F. G.; PINTO, J. C. Modeling and parameter estimation of step-growth polymerization of poly(ethylene-2,5-furandicarboxylate). **Polymer Engineering & Science**, v. 58, n. 5, p. 729–741, maio 2018.

103 SCHWAAB, M.; BISCAIA JR., E. C.; MONTEIRO, J. L.; PINTO, J. C. Nonlinear parameter estimation through particle swarm optimization. **Chemical Engineering Science**, v. 63, n. 6, p. 1542–1552, mar. 2008.

104 BANSAL, J. C.; SINGH, P.; SARASWAT, M.; VERMA, A.; JADON, S. S.; ABRAHAM, A. Inertia weight strategies in particle swarm optimization. In: IEEE. **2011 Third world congress on nature and biologically inspired computing**. [S.l.], 2011. p. 633–640.

105 ZHANG, Y.; WANG, S.; JI, G. A Comprehensive Survey on Particle Swarm Optimization Algorithm and Its Applications. **Mathematical Problems in Engineering**, v. 2015, p. 1–38, 2015.

106 ALMEIDA, B. S. G. de; LEITE, V. C. Particle Swarm Optimization: A Powerful Technique for Solving Engineering Problems. In: SER, J. D.; VILLAR, E.; OSABA, E. (Ed.). **Swarm Intelligence - Recent Advances, New Perspectives and Applications**. [S.l.]: IntechOpen, 2019. ISBN 978-1-78984-536-5 978-1-78984-537-2.

107 ENGELBRECHT, A. P. **Computational intelligence: an introduction**. 2nd ed. ed. Chichester, England ; Hoboken, NJ: John Wiley & Sons, 2007. ISBN 978-0-470-03561-0.

108 TALUKDER, S. **Mathematicle modelling and applications of particle swarm optimization**. Tese (Master) — Blekinge Institute of Technology, Karlskrona, Sweden, fev. 2011.

109 NETO, J. G. **Modeling of suspension copolymerization of poly(vinyl acetate-co-methyl methacrylate) for vascular embolization procedures**. Tese (Master) — Pontifícia Universidade Católica do Rio de Janeiro, Rio de Janeiro, Brazil, dez. 2021.

110 SCHWAAB, M.; BISCAIA JR., E. C.; MONTEIRO, J. L.; PINTO, J. C. Nonlinear parameter estimation through particle swarm optimization. **Chemical Engineering Science**, v. 63, n. 6, p. 1542–1552, mar. 2008.

111 BEALE, E. M. L. Confidence Regions in Non-Linear Estimation. **Journal of the Royal Statistical Society: Series B (Methodological)**, v. 22, n. 1, p. 41–76, jan. 1960.

112 ROINE, A. **HSC Chemistry [Software], Outotec**. Pori, Finland: Outotec, 2018.

113 HAIRER, E.; NØRSETT, S. P.; WANNER, G. **Solving ordinary differential equations I: nonstiff problems**. 2nd rev. ed. ed. Heidelberg ; London: Springer, 2009. (Springer series in computational mathematics, 8). ISBN 978-3-540-56670-0.

114 OLSZAK-HUMIENIK, M.; MOZEJKO, J. Thermodynamic functions of activated complexes created in thermal decomposition processes of sulphates. **Thermochimica Acta**, Elsevier, v. 344, n. 1-2, p. 73–79, jan 2000.

A
Mathematical models

A.1
Aluminum-bearing compounds

$$\begin{cases} \dfrac{df}{dt} = m_0^n (1-f)^n k_0 \exp\left(-\dfrac{E_a}{RT}\right) \\ f(0) = 0 \end{cases} \tag{A-1}$$

A.2
Zinc sulfate

$$\begin{cases} \dfrac{df_1}{dt} = m_{0,1}^{n_1} (1-f_1)^{n_1} k_{0,1} \exp\left(-\dfrac{E_{a,1}}{RT}\right) \\ \dfrac{df_2}{dt} = m_{0,2}^{n_2} (1-f_2)^{n_2} k_{0,2} \exp\left(-\dfrac{E_{a,2}}{RT}\right) - \\ \qquad \left[m_{0,1}^{n_1} (1-f_1)^{n_1} k_{0,1} \exp\left(-\dfrac{E_{a,1}}{RT}\right)\right] \\ f_1(0) = f_2(0) = 0 \end{cases} \tag{A-2}$$

A.3
Iron(II) sulfate

A.3.1
Dehydration

$$\begin{cases} \dfrac{df_1}{dt} = m_{0,1}^{n_1} (1-f_1)^{n_1} k_{0,1} \exp\left(-\dfrac{E_{a,1}}{RT}\right) \\ \dfrac{df_2}{dt} = m_{0,2}^{n_2} (1-f_2)^{n_2} k_{0,2} \exp\left(-\dfrac{E_{a,2}}{RT}\right) - \\ \qquad \left[m_{0,1}^{n_1} (1-f_1)^{n_1} k_{0,1} \exp\left(-\dfrac{E_{a,1}}{RT}\right)\right] \\ \dfrac{df_3}{dt} = m_{0,3}^{n_3} (1-f_3)^{n_3} k_{0,3} \exp\left(-\dfrac{E_{a,3}}{RT}\right) - \\ \qquad \left[m_{0,2}^{n_2} (1-f_2)^{n_2} k_{0,2} \exp\left(-\dfrac{E_{a,2}}{RT}\right)\right] \\ f_1(0) = f_2(0) = f_3(0) = 0 \end{cases} \tag{A-3}$$

A.3.2
Desulfation

$$\begin{cases} \dfrac{df_1}{dt} = m_{0,1}^{n_1}(1-f_1)^{n_1} k_{0,1} \exp\left(-\dfrac{E_{a,1}}{RT}\right) \\ \dfrac{df_2}{dt} = m_{0,2}^{n_2}(1-f_2)^{n_2} k_{0,2} \exp\left(-\dfrac{E_{a,2}}{RT}\right) - \\ \qquad \left[m_{0,1}^{n_1}(1-f_1)^{n_1} k_{0,1} \exp\left(-\dfrac{E_{a,1}}{RT}\right)\right] \\ f_1(0) = f_2(0) = 0 \end{cases} \tag{A-4}$$

B
Confidence regions

B.1
Aluminum sulfate

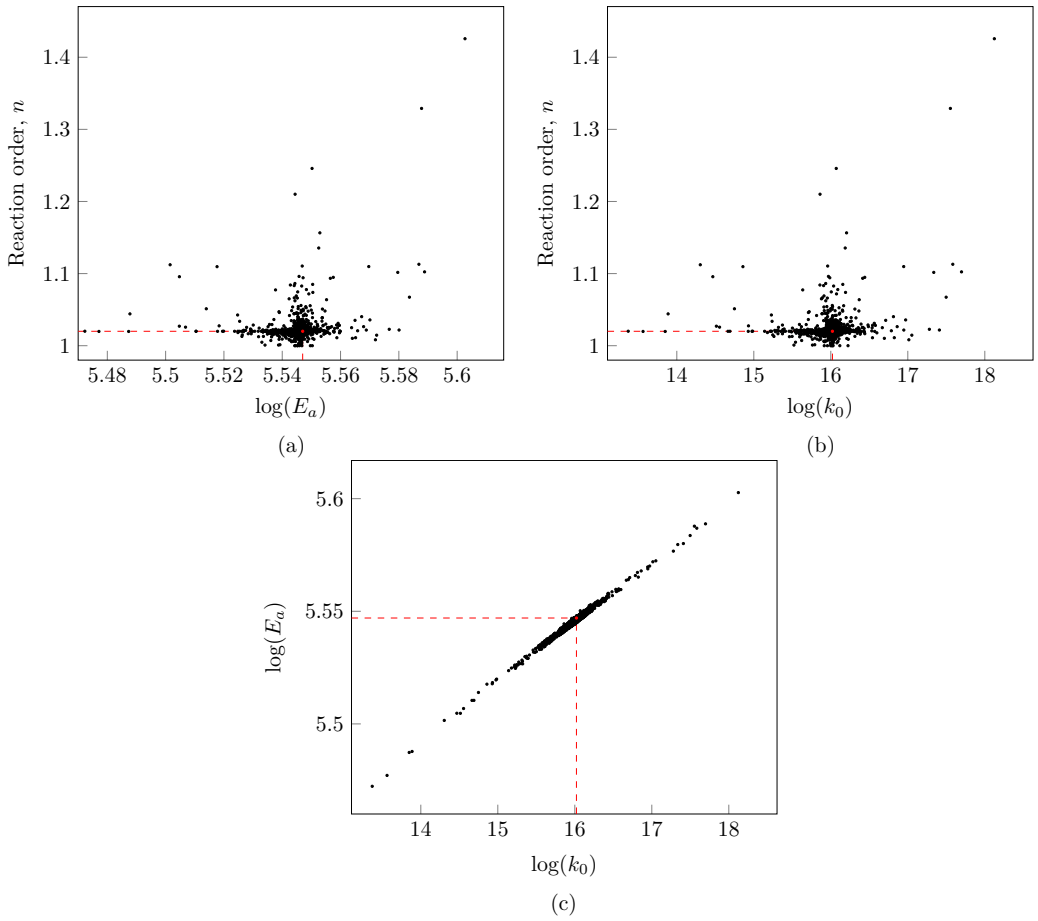

Figure B.1: Confidence region of the optimization of the thermal decomposition of aluminum sulfate: (a) E_a vs. n; (b) k_0 vs. n; (c) k_0 vs. E_a.

B.2
Potassium alum

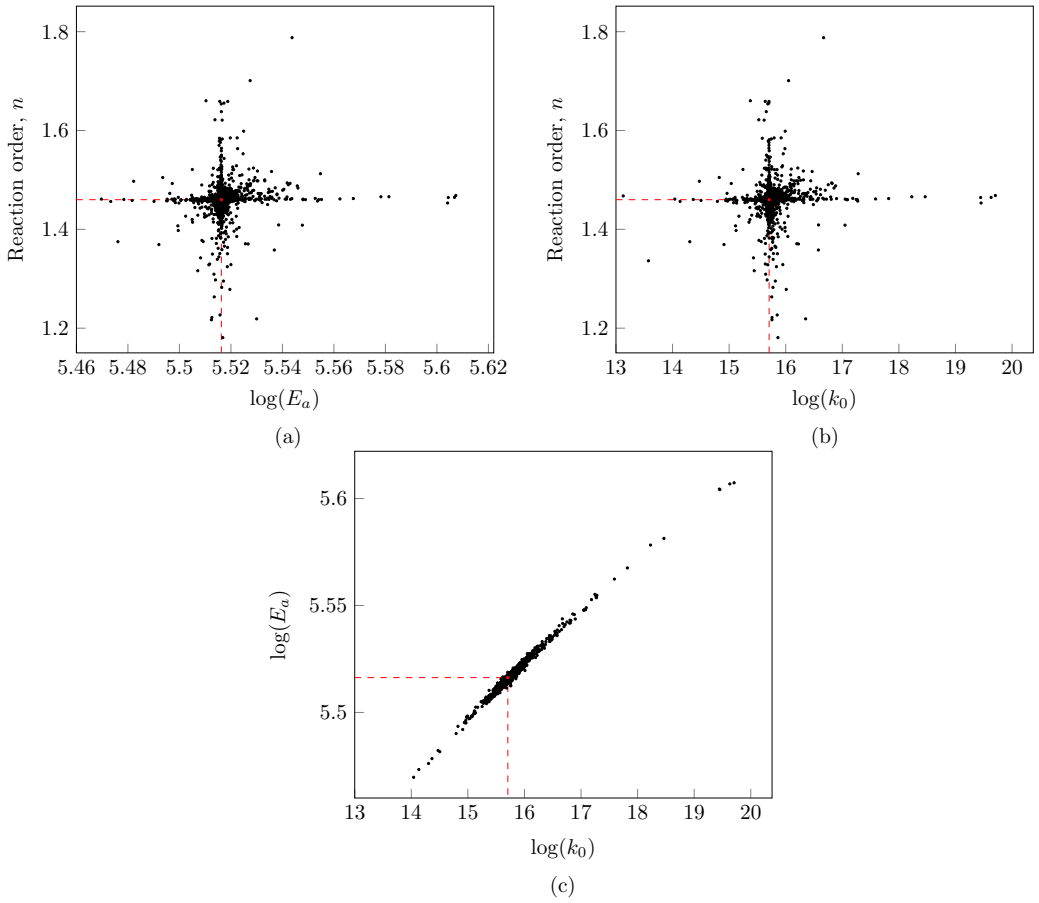

Figure B.2: Confidence region of the optimization of the thermal decomposition of potassium alum: (a) E_a vs. n; (b) k_0 vs. n; (c) k_0 vs. E_a.

B.3
Mixture of potassium and aluminum sulfates

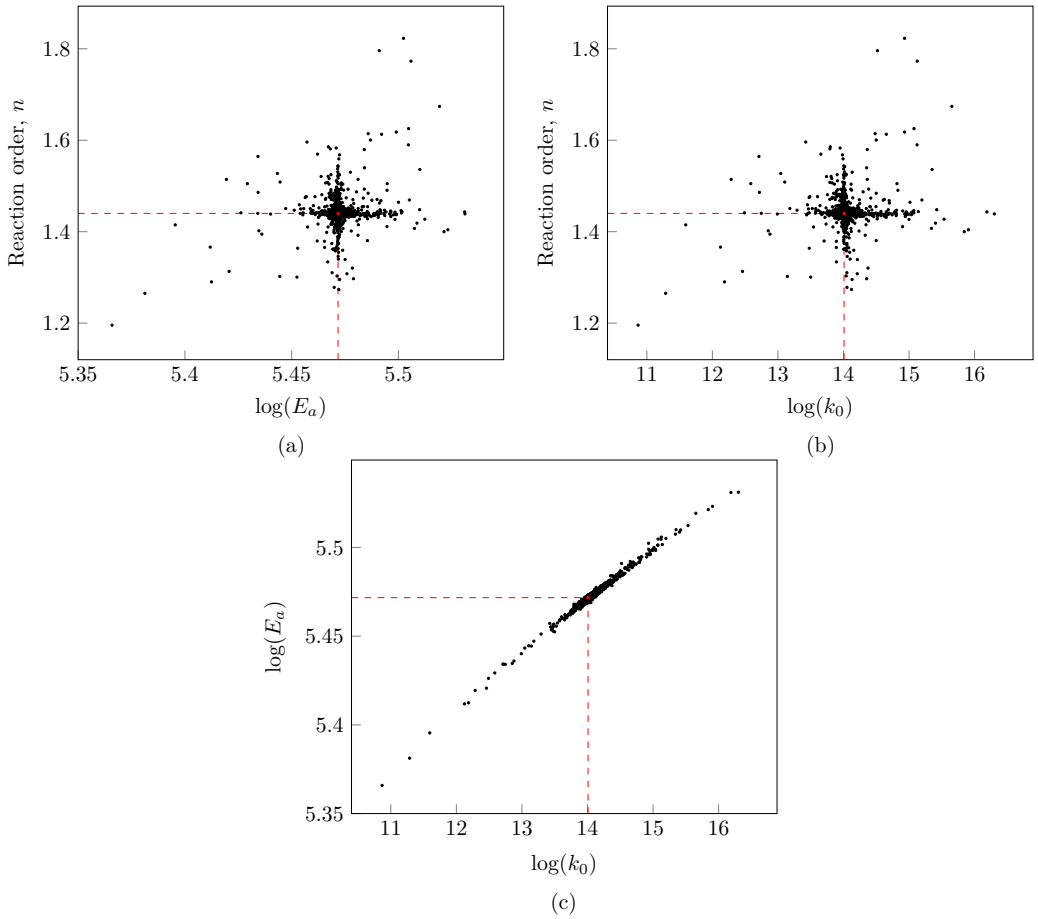

Figure B.3: Confidence region of the optimization of the thermal decomposition of mixture of sulfates: (a) E_a vs. n; (b) k_0 vs. n; (c) k_0 vs. E_a.

B.4
Zinc sulfate

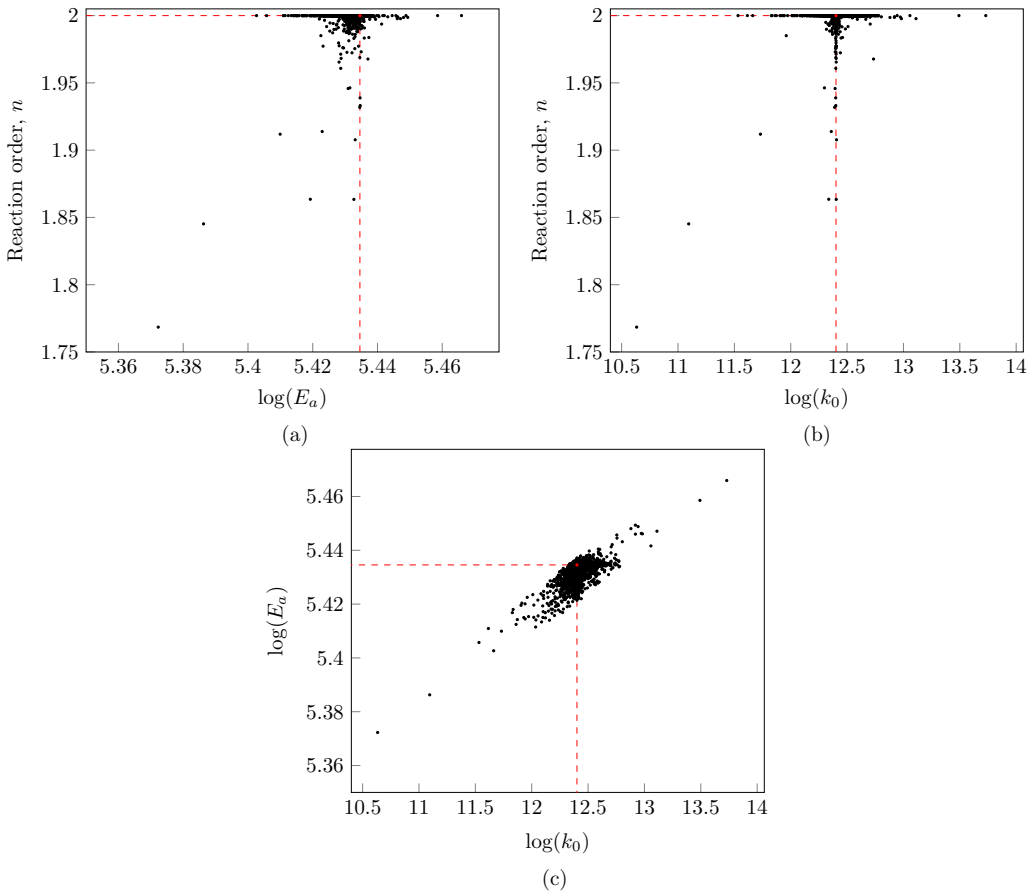

Figure B.4: Confidence region of the optimization of the thermal decomposition of zinc sulfate: (a) E_a vs. n; (b) k_0 vs. n; (c) k_0 vs. E_a.

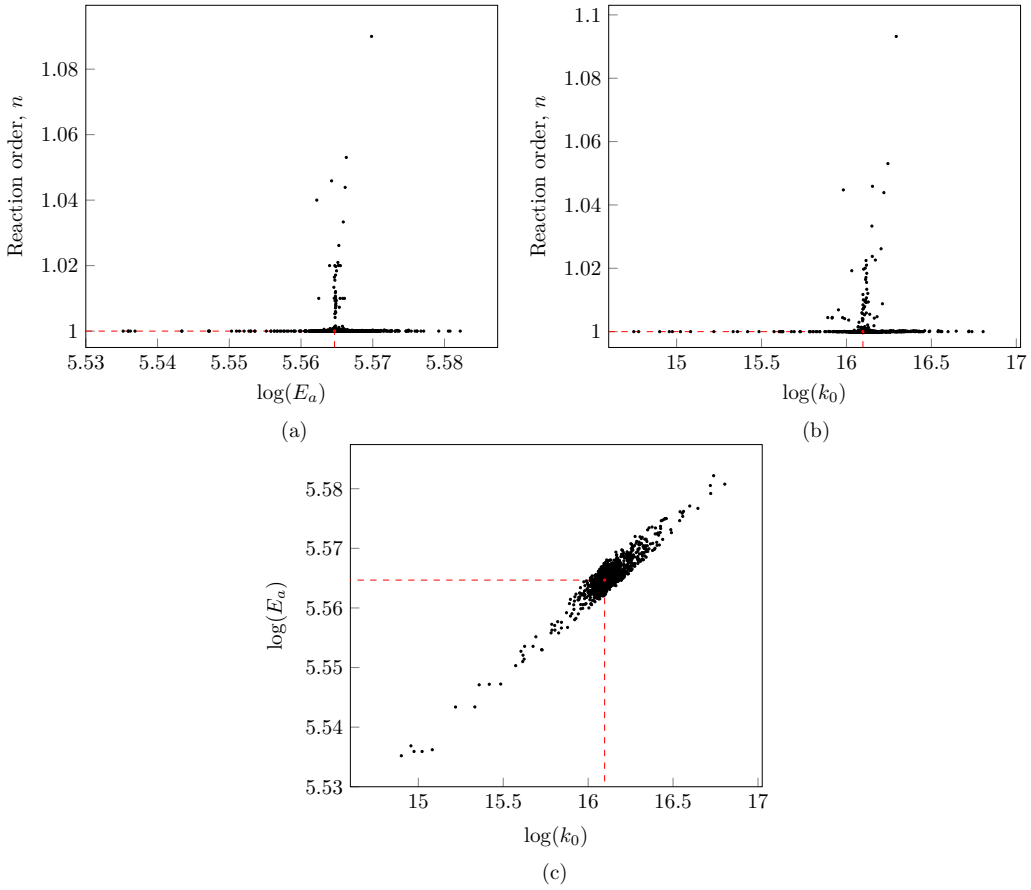

Figure B.5: Confidence region of the optimization of the thermal decomposition of zinc oxysulfate: (a) E_a vs. n; (b) k_0 vs. n; (c) k_0 vs. E_a.

B.5
Iron sulfate

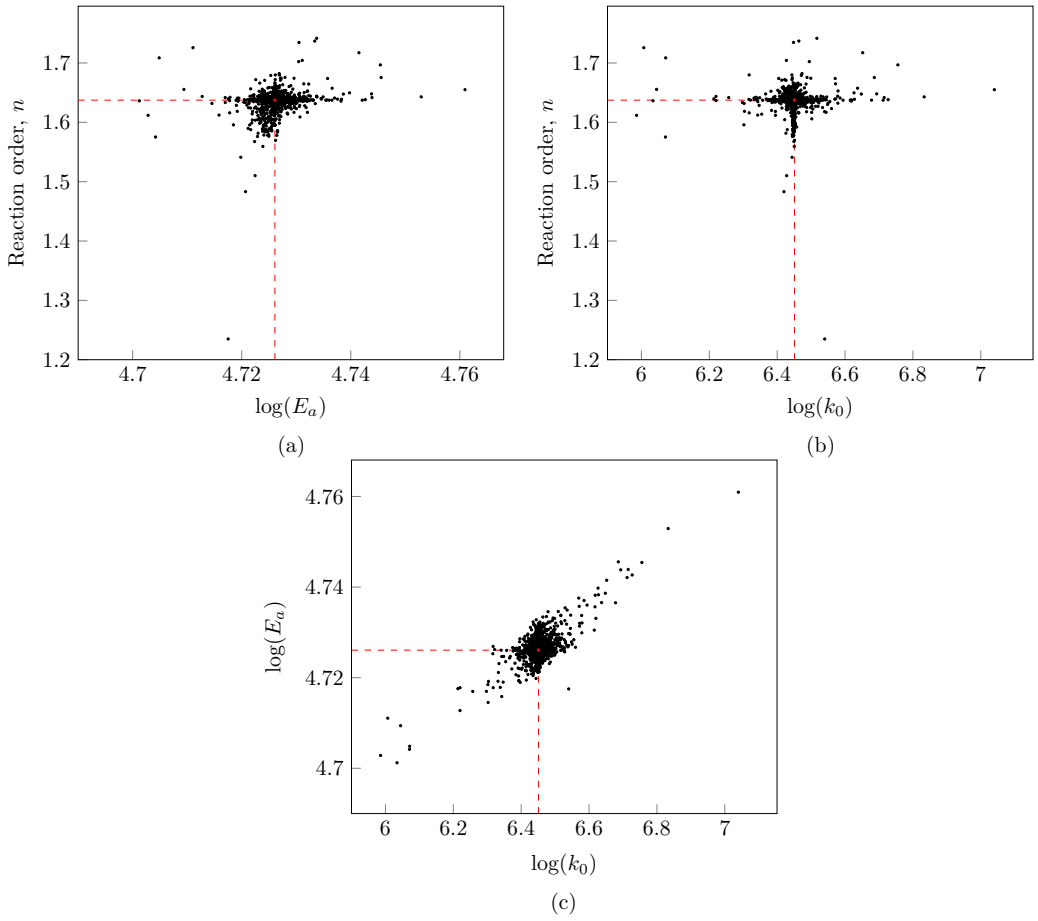

Figure B.6: Confidence region of the optimization of the thermal decomposition of iron sulfate heptahydrate: (a) E_a vs. n; (b) k_0 vs. n; (c) k_0 vs. E_a.

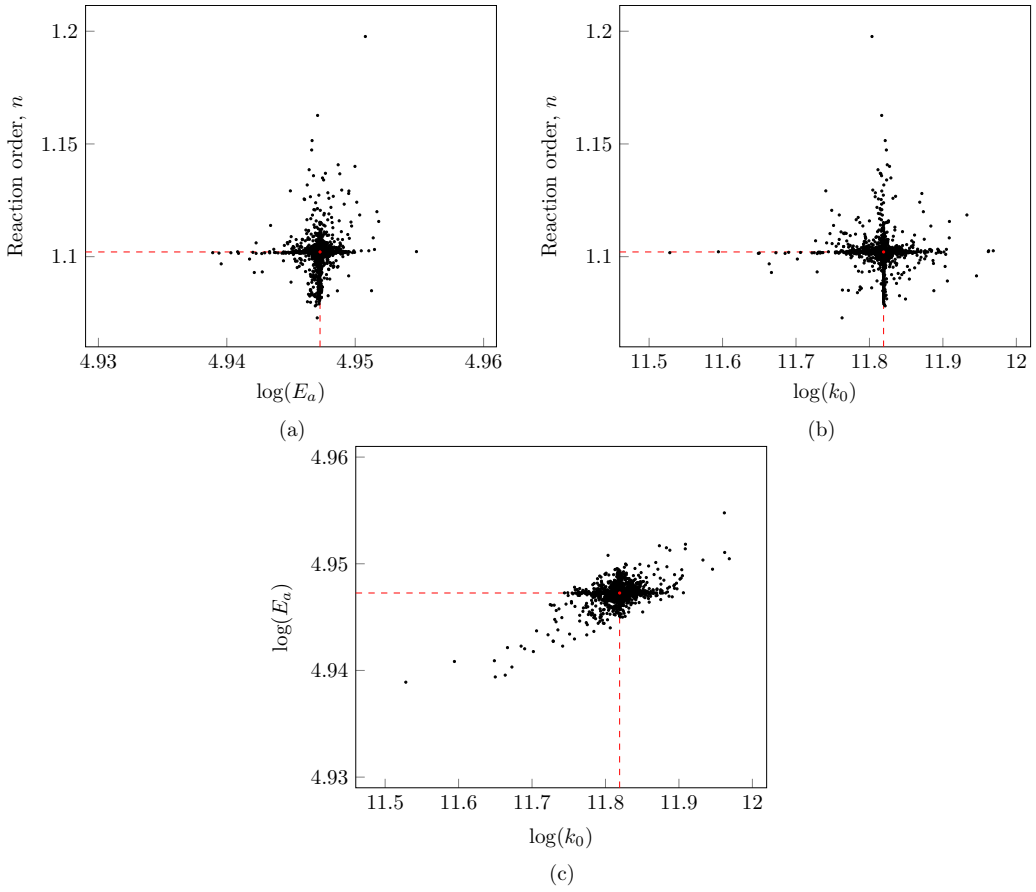

Figure B.7: Confidence region of the optimization of the thermal decomposition of iron sulfate tetrahydrate: (a) E_a vs. n; (b) k_0 vs. n; (c) k_0 vs. E_a.

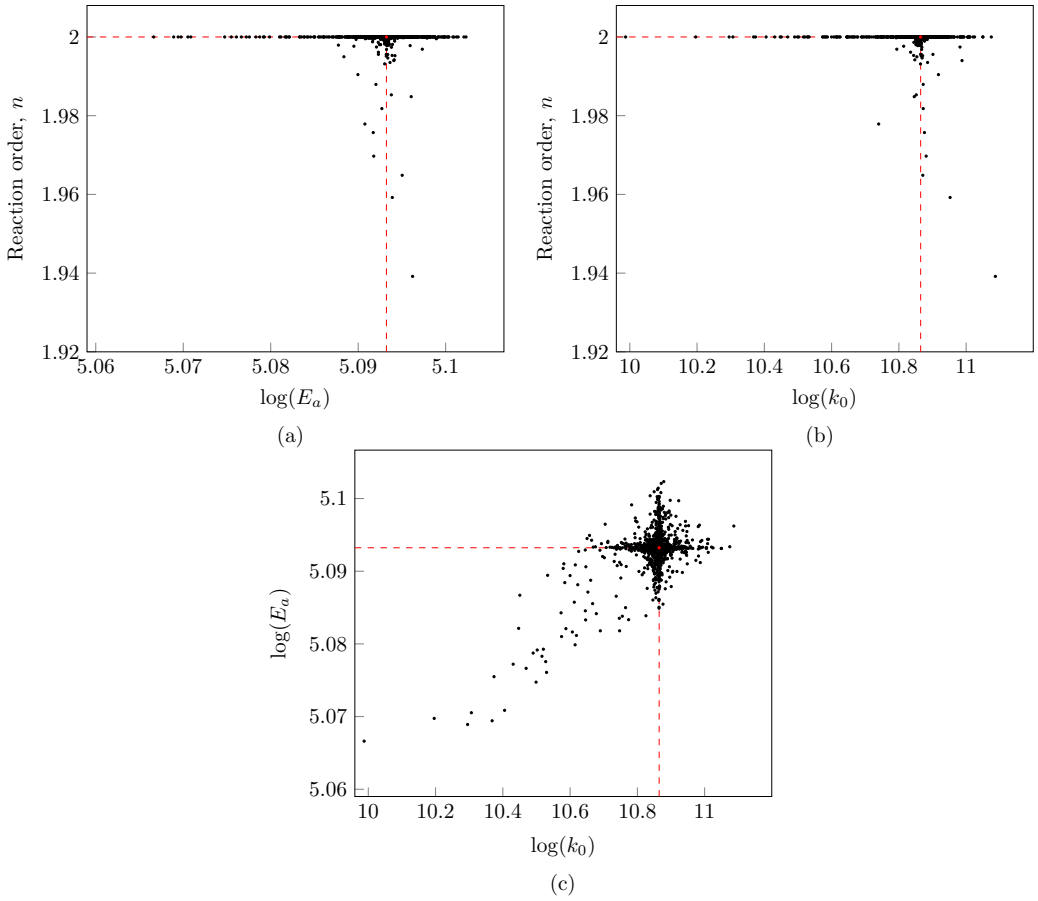

Figure B.8: Confidence region of the optimization of the thermal decomposition of iron sulfate monohydrate: (a) E_a vs. n; (b) k_0 vs. n; (c) k_0 vs. E_a.

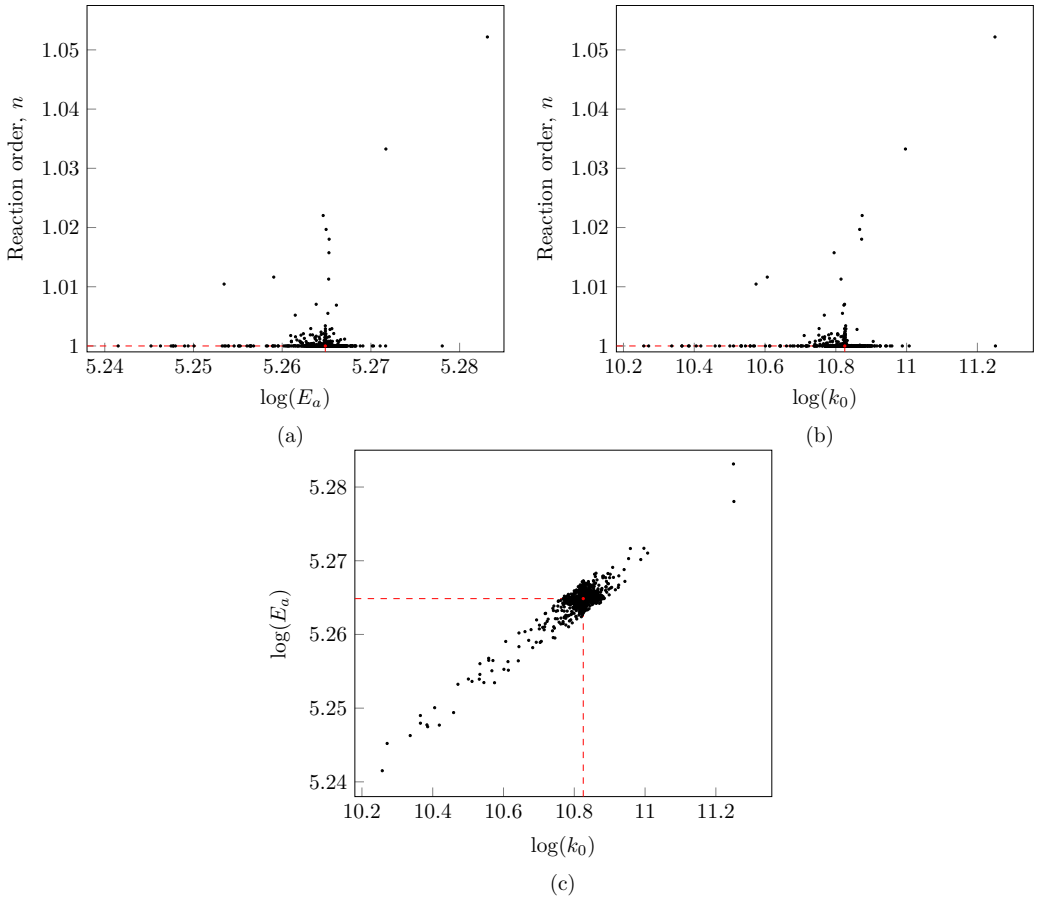

Figure B.9: Confidence region of the optimization of the thermal decomposition of iron sulfate: (a) E_a vs. n; (b) k_0 vs. n; (c) k_0 vs. E_a.

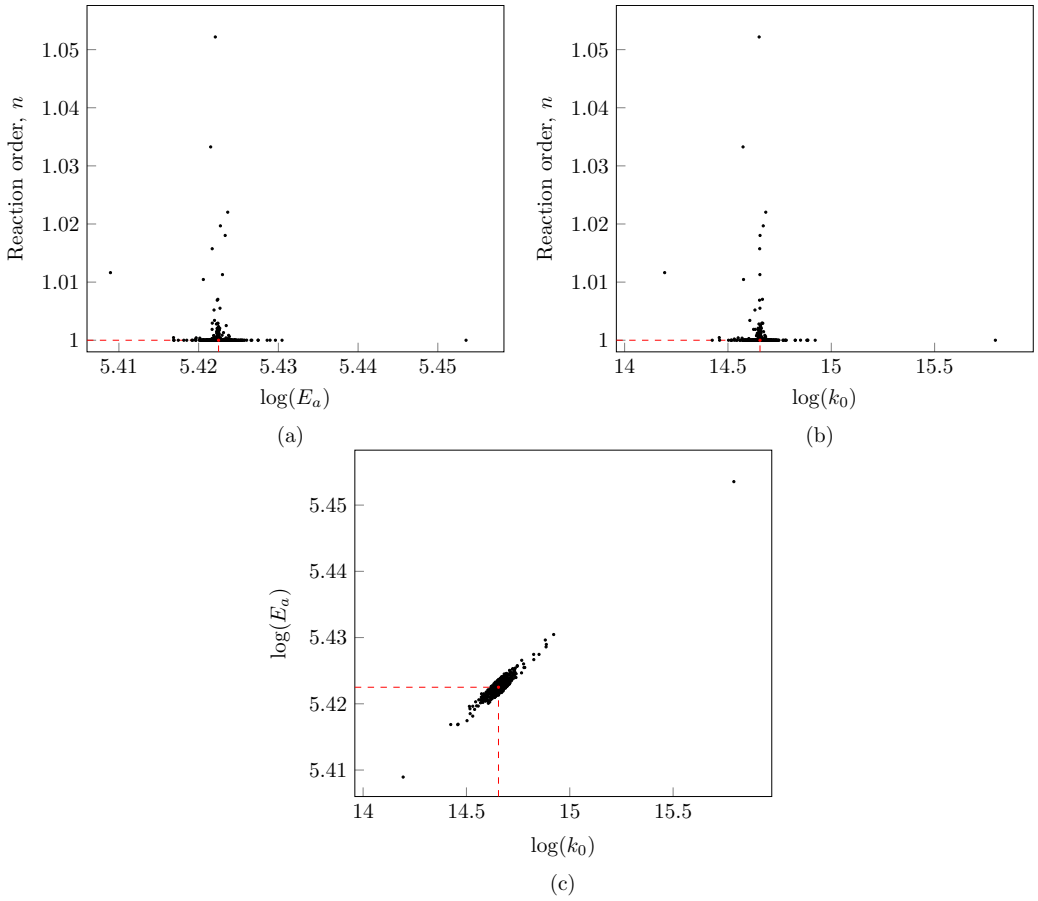

Figure B.10: Confidence region of the optimization of the thermal decomposition of iron oxysulfate: (a) E_a vs. n; (b) k_0 vs. n; (c) k_0 vs. E_a.

C
PSO codes

– PSO_estimation.py: Python script that estimates the unknown parameters. The number of particles, maximum number of iterations, the tolerance, and the lower and upper boundaries are defined before entering the PSO call. The PSO function defines all the initial estimation parameters (acceleration coefficients, and initial inertia weight coefficient). When one criteria stop is met (number of iterations or tolerance), the PSO function returns the best particle's position (best parameters estimation), the iteration in which the best result was obtained, the lowest objective function error value, and the information of the best particles throughout the estimation process.

```
import matplotlib.pyplot as plt
import numpy as np
import time
import random
import os
import sys
from Organized_PSO_form import decomp_reac
from Report import *

random.seed(time.time()**2.0)

def PSO(func, XMinMax, tol, number_of_particles, itmax,
    exp_time, exp_conversion):

    global confidence_region, vet_error, vet_it, vet_speed

    # Constants
    n = number_of_particles  # number of particles
    x_min = XMinMax[:, 0]   # array of minimuns
    x_max = XMinMax[:, 1]   # array of maximuns
    tot_param = len(x_min)  # number of parameters
    w_initial = 0.9 # initial inertia
    w_final = 0 # final inertia
    c1 = 1  # acceleration coefficient
    c2 = 1  # acceleration coefficient
    particle_pos = np.zeros((n, tot_param))  # Position of
    each particle
    best_ind_pos = np.zeros((n, tot_param))  # Best position
    for each particle
```

```
27      best_ind_value = np.zeros(n)  # Best function value for
    each particle
28      particle_speed = np.zeros((n, tot_param))  # Will be
    initially keept 0
29      confidence_region = np.empty(shape=[0, tot_param+1])
30
31      vet_error = np.zeros(itmax)
32      vet_speed = np.zeros(itmax)
33      vet_it = np.zeros(itmax)
34
35      best_particle_pos_hist = np.zeros((itmax, tot_param))
36      print('STARTED')
37      print('DEFINING INITIAL CONDITIONS')
38      # Initial condition for each particle
39      for k in range(0, n):
40          for i in range(0, tot_param):
41              lambda_rand = random.random()
42              particle_pos[k, i] = x_min[i]
43                  + lambda_rand * (x_max[i] - x_min[i])
44              best_ind_pos[k, i] = particle_pos[k, i]
45
46      # Could have put another line to change particles'
    initial speed
47
48      best_particle_pos = particle_pos[0]
49      # Best global position initial value
50      best_value = func(best_particle_pos)  # Best global value
     initial value
51
52      print('INITIAL BEST VALUE SEARCH STARTED')
53
54      # Defining the individual best value for each particle
    and the global best initial position/value
55      for k in range(0, n):
56          best_ind_value[k] = func(particle_pos[k])
57          if best_ind_value[k] < best_value:  # < because it is
     intended to find the minimum value of the function
58              best_particle_pos = particle_pos[k]
59              best_value = best_ind_value[k]
60      evaluation = 10
61      print('GLOBAL SEARCH STARTED')
62      # Global minimum search
63      for i in range(0, itmax):
64          os.system('cls' if os.name == 'nt' else 'clear')
65          print('previous evaluation: %f of %f tolerance' % (
    evaluation, tol))
66          print('Current best error value = ', best_value)
```

```
67          print('Current best position = ', 10**
    best_particle_pos)
68          print('%i of at most %i' % (i + 1, itmax))
69
70          w = w_initial + (w_final - w_initial) * (i / itmax)
71
72          for k in range(0, n):
73              sys.stdout.write('\rProcessing Particle ' + str(k
     + 1) + ' of ' +
74                               str(n))
75              for j in range(0, tot_param):
76                  lambda_rand = random.random()
77                  mu_rand = random.random()
78                  particle_speed[k, j] = w * particle_speed[k,
    j]
79                      + c1 * lambda_rand * (best_ind_pos[k, j]
    - particle_pos[k, j])
80                      + c2 * mu_rand * (best_particle_pos[j] -
    particle_pos[k, j])
81              particle_pos[k] = particle_pos[k] +
    particle_speed[k]
82              for j in range(0, tot_param):
83                  if particle_pos[k, j] > x_max[j]:
84                      particle_pos[k, j] = x_max[j]
85                      particle_speed[k, j] = 0
86                  if particle_pos[k, j] < x_min[j]:
87                      particle_pos[k, j] = x_min[j]
88                      particle_speed[k, j] = 0
89              f_value = func(particle_pos[k])
90              array = np.zeros(tot_param+1)
91
92              for l in range(tot_param):
93                  array[l] = particle_pos[k, l]
94
95              array[tot_param] = f_value
96              confidence_region = np.append(confidence_region,
    array)
97              confidence_region = confidence_region.reshape(int
    (np.size(confidence_region, 0) / (tot_param+1)), (
    tot_param+1))
98              if f_value < best_ind_value[k]:  # < because it
    is intended to find the minimum value of the function
99                  best_ind_value[k] = f_value
100                 best_ind_pos[k] = particle_pos[k]
101             if f_value < best_value:  # < because it is
    intended to find the minimum value of the function
102                 best_value = f_value
```

```
103                 best_particle_pos = np.array(particle_pos[k])
104                 #print(10 ** best_particle_pos, best_value, i
    ) # tests purpose
105         evaluation = sum(sum(abs(particle_speed)))
106         vet_error[i] = best_value
107         vet_speed[i] = evaluation
108         vet_it[i] = i
109 
110         best_particle_pos_hist[i, :] = best_particle_pos
111         if (evaluation < tol):
112             break
113         sys.stdout.flush()  # cleans print last line
114     return best_particle_pos, i, best_value,
    best_particle_pos_hist
115 
116 global expData
117 
118 initialTime = time.process_time()
119 expDataPartial = np.loadtxt('Experimental/expFile.txt',
120                             dtype=float,
121                             unpack=True)
122 m, n = expDataPartial.shape
123 
124 temperatureExp = expDataPartial[0, :] + 273.15
125 timeExp = expDataPartial[1, :]
126 conversionExp = np.zeros(n, dtype=np.float64)
127 for i in range(n):
128     conversionExp[i] = (expDataPartial[2, i] - expDataPartial
    [2, 0]) / (
129         expDataPartial[2, -1] - expDataPartial[2, 0])
130     if conversionExp[i] < 0:
131         conversionExp[i] = 0
132     if conversionExp[i] > 1:
133         conversionExp[i] = 1
134 
135 def Fobj(estParams):
136     func_parameteres = np.array([10 ** estParams[0], 10 **
    estParams[1], 10 ** estParams[2])
137     obj_func_error = decomp_reac(func_parameteres, timeExp,
    conversionExp)
138     return obj_func_error
139 
140 
141 # PSO Parameters
142 tol = 1.e-1
143 itmax = 500
144 number_of_particles = 45
```

```
145
146 # PSO Call
147 bounds = np.array([[1e4, 1e20], [1.e2, 1.e5], [1.0, 2.0]])
148 MinMaxMatrix = np.log10(bounds)
149 Results = PSO(Fobj, MinMaxMatrix, tol, number_of_particles,
        itmax, timeExp, conversionExp)
150 estimated_variables = Results[0]
151 procTime = time.process_time() - initialTime
152 print('Estimation prossessing time = %f seconds' % procTime)
153
154 nPar = 3
155 Nexp = 1
156 NVSai = 17
157 NVEnt = 1
158 GL = float(Nexp*NVSai - nPar)
159 fopt = Results[2]
160 print('GL = ',GL)
161
162 alpha = 0.05
163
164 xopt = estimated_variables
165
166 report(Nexp, NVEnt, NVSai, nPar, GL, alpha, fopt, xopt)
167 report_pso(vet_error, vet_it, vet_speed, itmax)
168 report_confidence_region(nPar, fopt, GL, alpha,
        confidence_region)
```

– Organized_PSO_form.py: Python script that represents the simulation of given parameter set. The 'decomp_reac' function is called every time a particle is evaluated in the PSO function in the 'PSO_estimation.py' script. Moreover, the 'reac' function represents the set of differential equations of the studied system. The 'decomp_reac' function returns the objective function error correspondent to a set of parameters.

```
1 import numpy as np
2 import os
3 import sys
4 from scipy.integrate import ode
5 import matplotlib.pyplot as plt
6
7 def reac(t, Y, params):
8     R = 8.314
9     T = 10.02204373 * t + 21.37484961 + 273.15
10    m0 = 5.5
11
```

```
12      dy = np.zeros(1)
13      dy[0] = params[0] * m0**(params[2] - 1) * (1 - Y[0])**
    params[2] * np.exp(
14          -params[1] / (R * T))
15      return dy
16
17  def decomp_reac(est_params, t_exp, f_exp, temp_exp,
    plot_decision):
18
19      t0 = t_exp[0]  # [min] reaction initial time
20      tf = t_exp[-1]  # [min] reaction end time
21      tArray = np.arange(t0, tf, 0.05)  #np.linspace(t0, tf, Nt
    ) # Time vector
22      Nt = len(tArray)
23
24      NInputVar = 1  # number of input variables
25      InputVar = np.zeros(NInputVar)  # input variables vector
    for integration
26
27      InputVar[0] = 0.0
28
29      YY = np.zeros(NInputVar, dtype=float)
30      YY = ode(reac).set_integrator('dopri5').set_f_params(
    est_params)
31      YY.set_initial_value(InputVar, t0)
32      Y = np.zeros((int(Nt), len(YY.y)), dtype=float)
33      dt = (tf - t0) / (Nt)  #[min] integration interval
34      j = 0
35
36      while YY.successful() and YY.t < tf and j < Nt:
37          for k in range(len(YY.y)):
38              if YY.y[k] < 0:
39                  YY.y[k] = 0.0
40          Y[j, :] = YY.y[:]
41          j = j + 1
42
43          if (YY.t > 10000):
44              os.system("PAUSE")
45
46          YY.integrate(YY.t + dt)
47
48      conversion_calc = Y[:, 0]
49      error = 0
50      j = 0
51      f_calc = []
52      for i in range(0, len(tArray)):
53          if (j < len(t_exp)):
```

```
            if (abs(tArray[i] - t_exp[j]) < 1.e-2):

                error += (conversion_calc[i] - f_exp[j])**2
                j = j + 1
    return error
```

– Report.py: Python script called after the estimation process is completed. The 'report' function performs the statistical evaluation of the estimation. The 'report_pso' function creates a text file containing all the information regarding the swarm (error and sum of velocity) at each iteration. The 'report_confidence_region' function creates a text file with the coordinates of the particles which are within a confidence level previously defined.

```
from scipy.stats import f
from scipy import stats  # Statistical functions
import os
import numpy as np

def report(Nexp, NVEnt, NVSai, nPar, GL, alpha, fopt, xopt):
    file = "Report_aluminum_sulfate.txt"
    fileR = open(file, 'w')
    fileR.write('                PARAMETER ESTIMATION REPORT
                \n')
    fileR.write('\n')
    fileR.write('\n')
    fileR.write('Number of Experiments:')
    fileR.write("%i\n" % Nexp)
    fileR.write('Number of Inlet Variables:')
    fileR.write("%i\n" % NVEnt)
    fileR.write('Number of Outlet Variables:')
    fileR.write("%i\n" % NVSai)

    fileR.write(' \n')
    fileR.write('Number of Measured Data Types:')
    fileR.write("%i\n" % NVSai)
    fileR.write(' \n')
    fileR.write('Fobj:')
    fileR.write("%12.8f\n" % fopt)
    fileR.write('Chi2 Upper:')
    fileR.write("%8.2f\n" % stats.chi2.ppf((1.e0 + alpha) /
    2.e0, GL))
    print('CHI2 < Fopt < CHI2')
    print(stats.chi2.ppf((1.e0 - alpha) / 2.e0, GL), fopt,
          stats.chi2.ppf((1.e0 + alpha) / 2.e0, GL))
```

```
30      fileR.write('Chi2 Lower:')
31      fileR.write("%8.2f\n" % stats.chi2.ppf((1.e0 - alpha) /
    2.e0, GL))
32      fileR.write(' \n')
33
34      fileR.write('Estimate Parameters \n')
35      fileR.write("   Param          \n")
36      for i in range(0, nPar):
37          P = np.array([xopt[i]])
38          fileR.write("%12.6e\n" % (xopt[i]))
39      fileR.write('\n')
40      fileR.write('\n')
41      fileR.close()
42
43  def report_pso(error_array, iteration_array, velocity_array,
    max_it):
44      PSO_data = np.zeros((max_it,3))
45      PSO_data[:,0] = np.transpose(iteration_array)
46      PSO_data[:,1] = np.transpose(error_array)
47      PSO_data[:,2] = np.transpose(velocity_array)
48      np.savetxt('PSO_process_sulfate_mixture.txt',PSO_data,
    delimiter = ',', fmt='%.8f')
49
50  def report_confidence_region(nPar, fopt, GL, alpha,
    confidence_region):
51      print('=========================')
52      print('CONFIDENCE REGION')
53      print('=========================')
54
55      np.savetxt('RC0_aluminum_sulfate.txt',confidence_region,
    delimiter = ',')
56      D_FIN = f.ppf(1-alpha, float(nPar), GL)
57      FReg = fopt * (1.e0 + float(nPar) / GL * D_FIN)
58      RC = np.empty(shape=[0, nPar])
59
60      for i in range(0, len(confidence_region)):
61          if confidence_region[i,nPar] < FReg:
62              array = np.zeros(nPar)
63              for j in range(0, nPar):
64                  array[j] = confidence_region[i, j]
65              RC = np.append(RC, array)
66      RC = RC.reshape(int(np.size(RC, 0) / nPar), nPar)
67      np.savetxt('RC_aluminum_sulfate.txt',RC,delimiter = ',')
```